5-2018

Investigation of single drop particle scavenging using an ultrasonically levitated drop

Steven Fredericks
Clemson University, safrede@clemson.edu

Investigation of single drop particle scavenging using an ultrasonically levitated drop

---

A Dissertation
Presented to
the Graduate School of
Clemson University

In Partial Fulfillment
of the Requirements for the Degree
Doctor of Philosophy
Mechanical Engineering

---

by
Steven Fredericks
May 2018

Accepted by:
Dr. John R. Saylor, Committee Chair
Dr. Joshua B. Bostwick
Dr. Rodrigo Martinez-Duarte
Dr. Lonny L. Thompson

Abstract

Airborne particulate, known as aerosols, produced by both natural and anthropogenic means, have significant health and environmental impacts. Therefore understanding the production and removal of these particles is of critical importance. The main thrust of this thesis research is concerned with improving the understanding of removal of particulates via interaction with falling liquid drops, known as wet deposition. This process occurs naturally within rain and can be imposed in industrial applications with wet scrubbers. Therefore improved models for wet scavenging have applications in both climatology and pollution control.

To perform this study, first the performance of existing models for wet deposition was investigated. Models for drop scavenging of aerosols via inertial impaction proposed by Slinn and by Calvert were compared with published experimental measurements. A parametric study was performed on the residual of the model predictions from the measurements to identify dimensionless groups not included in these models, which might increase model performance. The study found that two dimensionless groups, the relative Stokes number, Stk_r and the drop Reynolds number Re, are both well correlated with the residual of these models. They are included in modified versions of both of these models to provide better performance. That these two dimensionless groups improve model performance suggests that an inertial mechanism and an advective mechanism not accounted for in the existing models play some role in aerosol scavenging in the inertial regime.

These findings were experimentally investigated to identify more specifically these mechanisms. To do this, single drop particle scavenging was experimentally measured using an ultrasonic levitation technique. This technique enabled measurements of scavenging efficiency, E, for individual drops, and allowed for control of drop axis ratio, α, drop shape oscillations, and Re independently from drop diameter. This allowed for more controlled manipulation of the drop wakes in both attached and vortex shedding regimes. Non-evaporating drops were used which resulted in essentially

zero temperature and vapor concentration difference between the drop surface and the surrounding air, virtually eliminating the possibility of confounding phoretic effects. Plots of E versus Stokes number, Stk, were found to depend on α. These plots became independent of α when Stk was calculated using the Sauter mean diameter (as opposed to the equivolume diameter). Furthermore, E was shown to be insensitive to both Re and drop shape oscillations, suggesting that wake effects do not have a measurable impact on E. Finally, a method was developed to relate models of E for spherical drops (the assumed shape in existing scavenging model predictions) to E for arbitrarily deformed drops, such as those occurring in rain. Of note, these are the first measurements of droplet scavenging obtained using ultrasonic levitation.

Finally, as drop scavenging is heavily dependent on particle size, a novel technique was identified and explored for improving aerosol sizing measurements. To do this, experiments were carried out in an impactor where the distance between the impactor nozzle and the impactor plate was small, much less than the typically used one nozzle diameter separation. The aerosol deposition patterns in this impactor were investigated for aerosols in the 3μm to 15μm diameter range. Ring-shaped deposition patterns were observed where the internal diameter and thickness of the rings were a function of the particle diameter. Specifically, the inner diameter and ring thickness were correlated to the Stokes number, Stk; the ring diameter decreased with Stk, and the ring thickness increased with Stk. At $Stk \sim 0.4$ the ring closed up, leaving a mostly uniform disk deposition pattern. These ring patterns do not appear to correspond to patterns previously described in the literature, and an order of magnitude analysis shows that this is an inertially dominated process. Though this method was not used for particle sizing in this thesis research, it is possible that further development of this approach will result in a more advanced particle sizing tool for aerosol science research.

Acknowledgments

I would like to thank my adviser, Dr. John R. Saylor for providing guidance and support to grow as a researcher and a scientist. I would also like to thank the rest of my committee members: Dr. Joshua B. Bostwick, Dr. Rodrigo Martinez-Duarte, and Dr. Lonny L. Thompson for their input and guidance in writing this dissertation. Additionally I would like to thank all of the current and former members of the research team: Weiyu Ran, Rachel Sundberg-Anderson, Jonathan Hodges, Tyler Merrell, and Sagar Dasgupta; with whom I've had uncountable conversations that helped me troubleshoot, refine, and clarify the research presented herein. Finally I would like to thank Dr. John Wagner and Dr. Todd Schweisinger for providing perspective and guidance for balancing this research with my teaching responsibilities.

Table of Contents

List of Tables

List of Figures

Chapter 1

Introduction

Aerosol loading, or the presence of particulate suspended in the atmosphere has been shown to have negative health impacts, with studies showing increased mortality rates for patients[29,47,72,94–96,106,113] directly correlated with local acute and prolonged aerosol concentrations. Additionally, increased exposure to aerosols has been shown to increase lung cancer rates[24,71,73] and asthma rates.[31,31,97,97] In addition to the health impacts cited above, aerosol loading has been shown to have environmental and climatic impacts. Some examples of this are the formation of acid rain by the adsorption of sulfate and nitrate aerosols by rain drops;[43] the promotion of lighter albedo clouds with large aerosol loading due to formation of smaller cloud droplets;[76] and additional radiative forcing caused by increased adsorption of solar radiation which increases with increasing aerosol loading.[1,44,48,79,85,123]

Given the above, it is critical to understand the sources and sinks which contribute to the global aerosol load. Aerosol generation occurs due to a wide variety of mechanisms, however some examples are the suspension of windblown soil dust, the formation of sea salt nuclei due to wave action, forest fires, and volcanic activity.[37,43,107] In addition to these naturally occurring particle sources, local and global anthropogenic aerosol loading is caused by emission of combustion products in power generation and transportation, as well as in industrial and mining activities.[37,43] This particulate is removed from the atmosphere through a variety of mechanisms, primarily gravitational settling, or dry deposition, and through interaction with rain, or wet deposition.[104] In the case of anthropogenic emissions the aerosol can be removed before exhausting the effluent to the atmosphere through processes such as filtration or wet scrubbing.[18,51,93,118] The present work is focused on

obtaining a better understanding of the removal mechanisms of particles due to interaction with water drops. As stated above, this occurs naturally in rain, and therefore this work can aid in improving climate models. Since wet deposition is used in pollution control systems the present work can be used to improve the design of wet scrubbers.

Aerosol scavenging by drops is quantified by the scavenging coefficient, E, which is the ratio of the number of particles collected by the drop, n_c, to the total number of particles within the air column through which the drop passed, n_t:

$$E = \frac{n_c}{n_t} \tag{1.1}$$

and ranges from zero to unity. There are several scavenging mechanisms which contribute to E: inertial, interception, diffusion, diffusiophoresis, and thermophoresis. Inertial scavenging occurs when the particle possesses enough mass to deviate from its streamline and impact the drop surface.[8,43,55,104] Interception scavenging occurs when the particle's center of mass does not deviate from its streamline, but due to its finite size it contacts the drop surface and is thereby removed.[36,43,104] Diffusion scavenging is caused by the Brownian motion of small particles as they diffuse across a streamline near the drop, causing them to deposit on the drop surface.[43,57,104] Diffusiophoretic scavenging occurs when there is a concentration gradient of the vapor phase of the drop surrounding the drop, and thermophoretic scavenging occurs when there is a temperature gradient around the drop. These gradients are generally caused by drop evaporation in wet scavenging applications, and are therefore a function of the drop fluid properties and the humidity of the surrounding air.[28,43,104,105] A schematic illustration showing each of the above scavenging modes is presented in Fig. 1.1. Though the focus of this work is on the intertial regime, comparisons with other models and interpretation of the data obtained herein requires reference to the other scavenging modes, hence this inclusion here.

1.1 Scavenging models

Models for the mechanisms described above have been developed in the literature which divide scavenging into several scavenging mechanisms which are modeled separately. The net scavenging is then determined by summing each mechanism's contribution, implicitly assuming that the scavenging mechanisms act independently of each other. Unless otherwise noted, E without a sub-

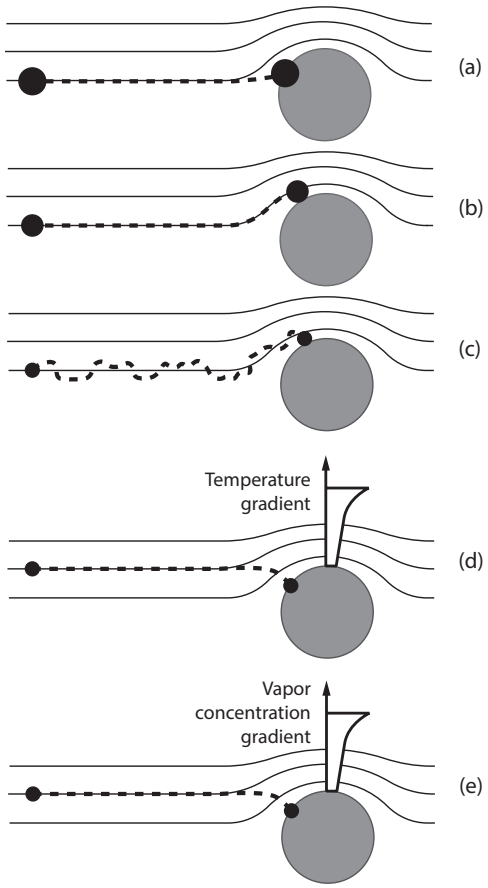

Figure 1.1: Schematic showing modes of particle scavenging by drops: (a) inertial impaction, (b) interception, (c) diffusion (Brownian motion), (d) thermophoresis due to a temperature gradient usually caused by drop evaporation, and (e) diffusiophoresis due to a vapor concentration gradient usually caused by drop evaporation.

script will be used to refer to the summation of scavenging contributions due to these mechanisms:

$$E = E_I + E_i + E_D + E_{tph} + E_{dph} \tag{1.2}$$

Equations for each of the scavenging modes are detailed in Appendix A for reference. Briefly, models of the above scavenging mechanisms are obtained as follows. Inertial scavenging, E_I, is commonly modeled in two different ways in the literature, either with the model of Slinn[104] which is based on the simulations of sphere collisions by Beard,[8] or with the model due to Calvert,[16,17] which is from curve fitting to the experimental results of Walton and Woolcock.[118] The Slinn model also has terms for interception and diffusion, E_i and E_D, respectively. With the interception term coming from the solution for flow over a sphere, and diffusion coming from Fickian diffusion to a sphere. Thermophoretic scavenging, E_{tph}, was obtained from the model due to Waldman, as reported by Davenport and Peters,[28] and diffusiophoretic scavenging, E_{dph}, was obtained from the model due to Waldman and Schmidt as reported by Davenport and Peters.[28]

The relative contributions of the mechanisms described in these models can vary considerably depending on the scavenging conditions. While the models for scavenging are functions of several variables, the mechanisms are all typically parameterized in terms of the Stokes number Stk, which is defined as:

$$Stk = \frac{U\rho d^2 C_c}{9\mu D} \tag{1.3}$$

where U is the velocity difference between the drop and the particle, ρ is the particle density; D is the drop diameter; d is the particle diameter; μ is the air viscosity; and C_c is the Cunningham correction coefficient:

$$C_c = 1 + \frac{2\lambda}{d}\left[1.257 + 0.4\exp\left(-0.55\frac{d}{\lambda}\right)\right] \tag{1.4}$$

where λ is the mean free path of air. Figure 1.2 presents a plot of E versus Stk as well as plots the contributing mechanisms versus Stk, demonstrating how the various mechanisms contribute to the total E. The general trend for wet scavenging is that E_I is dominant for large Stk, at intermediate Stk E_I drops and either E_i or E_{dph} become dominant, and finally at small Stk E_D or E_{tph} becomes dominant. Which mechanism is dominant at intermediate and low Stk is heavily

dependent on parameters not captured in Stk, such as the relative humidity of the air the drop is falling through, the Schmidt number, and the diameter ratio between the drop and particle. Because of these other factors, two example cases are presented in this figure to show how relative humidity can influence the scavenging, and in Fig. 1.3 scavenging models predictions will be presented for several drop diameters to demonstrate the influence of changing drop diameter on E. Figure 1.2 (a) presents the case of a 1 mm diameter drop falling at its terminal velocity, as determined by the formulation due to Beard,[6] through 50% relative humidity air. Here the Slinn model is used for the inertial component. In Fig. 1.2 (b) the case is presented for the same 1 mm diameter drop falling through 98% relative humidity air, again the Slinn model is used for the inertial contribution. In Fig. 1.2 (a) inertia is dominant by more than an order of magnitude for large Stk, however as Stk drops E also decreases. Near the critical Stokes number, Stk_*, which is the smallest Stk for which inertial impaction occurs, diffusiophoresis becomes the largest scavenging contributor. As Stk continues to decrease, the contribution from thermophoresis begins to dominate and E increases again. In contrast, Fig. 1.2 (b) shows the predicted scavenging in 98% humidity. For large Stk inertia is still dominant however, due to the much lower evaporation in this case, the concentration and temperature gradient near the drop surface is much smaller, causing interception to be the dominant scavenging mechanism at intermediate Stk, with the diffusiophoretic contribution an order of magnitude smaller. As Stk continues to decrease E_D becomes the dominant contribution and E again begins to increase. Therefore as this figure demonstrates, for large Stk inertia will always be several orders of magnitude larger than other scavenging mechanisms, however below the inertially dominant region, in other words for Stk smaller than Stk_*, the dominant mechanism is far more heavily dependent on mechanisms which are not captured entirely with Stk.

1.2 Previous experimental research

Other researchers have experimentally measured drop scavenging, and these results have been extensively reported in the literature,[3,5,15,40–42,52,53,56,59,74,77,78,116,118,119] with experimental techniques divided into two categories: vertical wind tunnels and fall towers. Vohl *et al.* used drops levitated in a vertical wind tunnel with induced turbulence upstream of the drop.[116] Beard used drops levitated in a vertical wind tunnel with 99% humidity and intentionally induced charge differences between drops and particles.[5] Walton and Woolcock used sessile drops mounted in a

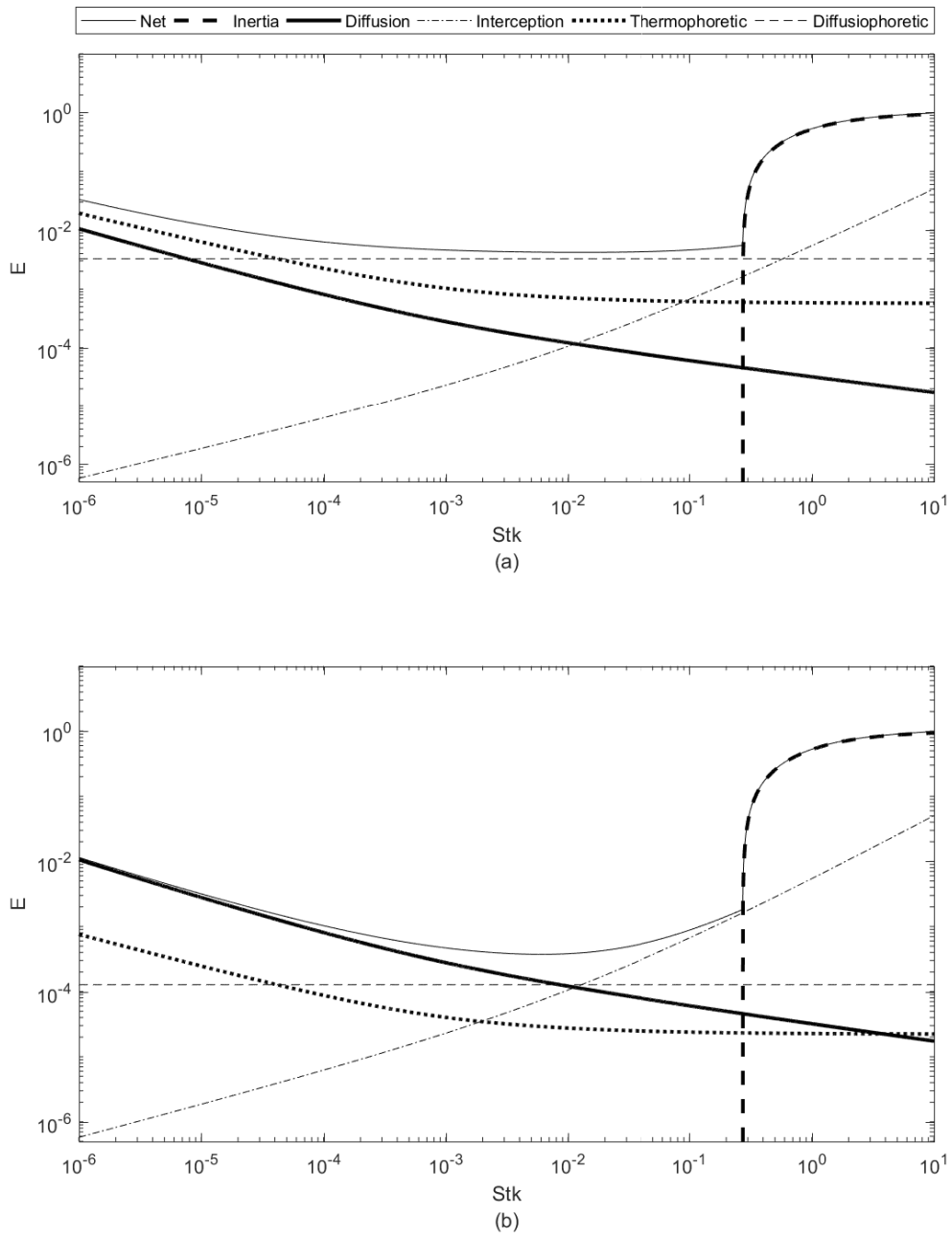

Figure 1.2: Plots showing the contributions of the net scavenging as well as individual mechanism contributions to scavenging versus Stk for a 1 mm diameter drop falling at terminal velocity through (a) 50% relative humidity air and (b) 98% relative humidity air.

vertical wind tunnel.[118] Ardon-Dryer *et al.* used freely falling drops of dilute ammonium sulfate at humidities of 15% and 88%.[3] Querel *et al.* used freely falling drops at terminal velocity in a fall tower with humidity between 30 and 90%.[77] Ladino *et al.* used freely falling drops in a fall tower at a fixed 89% humidity.[52] Chate & Kamra[59] and Pranesha & Kamra[74] used freely falling drops at terminal velocity in a fall tower with humidity between 35 and 50%. Byrne and Jennings used freely falling drops at terminal velocity in a fall tower with humidity of 58%.[15] Leong *et al.* used freely falling drops at terminal velocity with humidity of 30%.[56] Lai *et al.* used freely falling drops at terminal velocity in a fall tower.[53] Wang and Pruppacher used freely falling drops in a fall tower.[119] Hampl and Kerker and Hampl *et al.* used sub-terminal drops falling in a helium filled fall tower.[41,42] Starr and Mason used drops falling at terminal velocity in a low humidity fall tower.[78] Gunn and Hitschfeld used drops falling at terminal velocity in a high humidity fall tower.[40] Hereafter E_m will be used when referring specifically to the above measured scavenging data, or a subset of this measured scavenging data.

These experimental scavenging results are presented in Fig. 1.3, which compares them to E, predicted from the sum of the models described above via Eq. (1.2). More than one model prediction is presented in Fig. 1.3 because, as noted above, the models are not solely functions of Stk, and as such will predict different E at a given Stk as the drop diameter changes. In Fig. 1.3, model predictions are given for drop diameters D = 0.1, 0.5, 1.0, and 5 mm. Also, since phoretic forces will depend on humidity, the predictions in Fig. 1.3 will change with humidity; the plots presented there are all for water drops in 50% relative humidity. Figure 1.3 clearly reveals very large deviations of the data from predictions provided by the models described above, as well as large deviations of individual data sets from each other. This is worst for intermediate Stk where there are four decades of scatter in E_m, and deviations from the predicted E are two orders of magnitude both over and under predicting E_m. This is where models indicate that E should be a minimum, therefore some of the scatter in this range may be due to relatively larger uncertainty in the small E measurements, however even at larger Stk where the data is relatively well clustered there still exists over a decade of scatter in E_m and the models under predict by up to two orders of magnitude. Some of the deviations in this plot are due to comparing the measured and model predicted scavenging base on Stk when other parameters are playing a role in scavenging, however as Chapter 2 will show, accounting for these factors, even in the relatively well behaved inertial dominated region, still results in poor agreement between modeled and measured scavenging. With

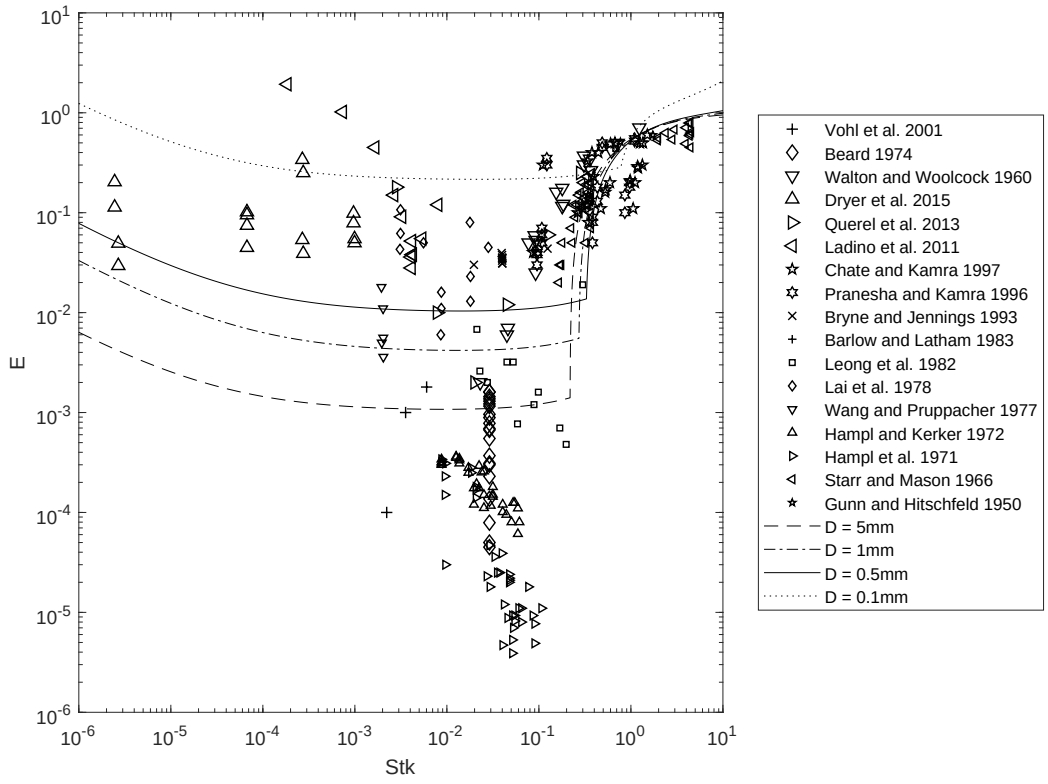

Figure 1.3: Plot showing surveyed scavenging data published in the literature (individual points),[3,5,15,40–42,52,53,56,59,74,77,78,116,118,119] and the net predicted scavenging, E, determined from the sum of model for E_i, E_I, E_D, E_{tph}, and E_{dph}, for various diameter drops at terminal velocity in 50% relative humidity air (lines).

the largest deviations between E_m and the measured results approaching two decades. Therefore there is a significant need to explain the poor agreement between the existing models and published scavenging results, as well as to develop models which better fit the experimental observations, and finally to quantify the role of additional parameters which have not yet been fully explored in the literature that may impact scavenging.

1.3 Aerosol sizing

The degree of the health and environmental impacts described above depend on, among other things, the size and number density of aerosols. Additionally the removal of these aerosols is greatly dependent on the size of the aerosols. A commonly used instrument for determining the size distribution and concentration of aerosols is the impactor,[43,58,61,115] a schematic of which is presented in Fig. 1.4. The impactor operates by accelerating an aerosol laden flow through a nozzle onto a plate oriented normal to the nozzle axis. This setup results in a low-diameter band-pass filter since large particles will deposit on the plate due to their inertia, while small particles pass around the impaction plate without deposition. By combining several of these plates, or stages, in series, an impactor cascade is created where each subsequent stage captures progressively smaller particle diameters. A schematic for a 5 stage cascade impactor is shown in Fig. 1.5 showing how the individual stages are connected. The particle size distribution can then be determined by gravimetrically measuring the mass deposited on the plate of each stage, with the number of bins in the resulting distribution equal to the number of stages in the cascade. Typical cascades have from five to eight stages, though impactors with more stages do exist such as the Sierra TAG, the MOUDI, nano-MOUDI and the ELPI impactors which have 9, 10, 13, and 13 stages, respectively.[60,61,63,64]

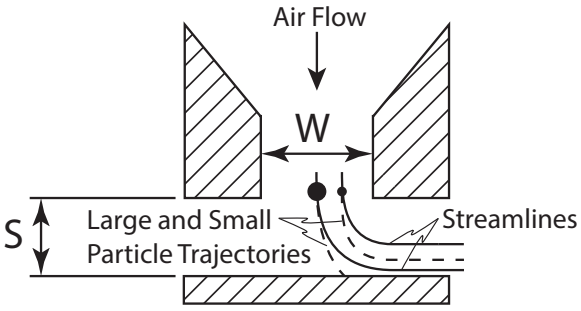

Figure 1.4: Schematic showing the geometry of an impactor and the typical particle path through an impactor.

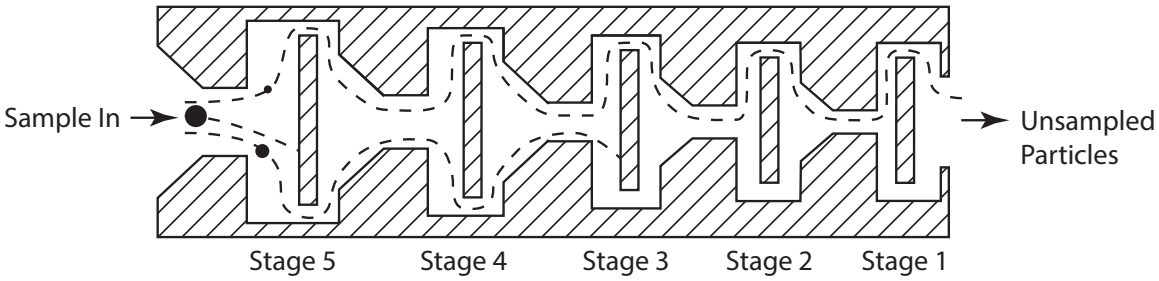

Figure 1.5: Schematic showing the combination of multiple stages to form a cascade impactor.

Impactor stages are typically characterized by their cutoff diameter, d_{50}, which is defined as the particle diameter for which 50% of the sampled particles will deposit on the impactor plate. The plot of the fraction of particles collected, η, versus particle diameter d is typically sigmoidal in shape, quickly approaching zero to the left of d_{50}, and quickly approaching unity to the right of d_{50}. A typical η versus d plot for a 5 stage cascade impactor is shown in Fig. 1.6, showing both the shape of the η versus d collection curves as well as the mass for each impactor stage. The steeper the curve at d_{50}, the less uncertainty there is in the diameter range collected by each impactor stage.[4,21] The steepness of the sigmoidal collection curve is determined by the characteristics of the flow through the impactor stage, and is primarily controlled by the ratio of the distance between the impaction plate and the nozzle, S, and the nozzle diameter, W. Typically, impactor stages are designed to have $S/W > 1$ to maximize the steepness of the deposition curve. This is likely the reason that exploration of small S/W impactors has been minimal. It has been shown that by decreasing S/W, the steepness of the deposition curve decreases, collecting more particles below d_{50} and fewer particles above d_{50} than is the case for $S/W > 1$. Decreasing S/W also decreases d_{50}.[39,58,62,64]

In the course of the experiments herein, a small S/W impactor was used. The goal in those experiments was to capture mondisperse particles for subsequent sizing via microscope imaging. Because the particles were monodisperse, the steepness of the η versus d curve was not relevant. The resulting deposition patterns were unexpectedly ring shaped, with the ring geometry a strong function of the particle size. Therefore opportunity exists to leverage this phenomona to develop a modification of the impactor which has a resolution better than the imposed resolution seen in impactor cascades.

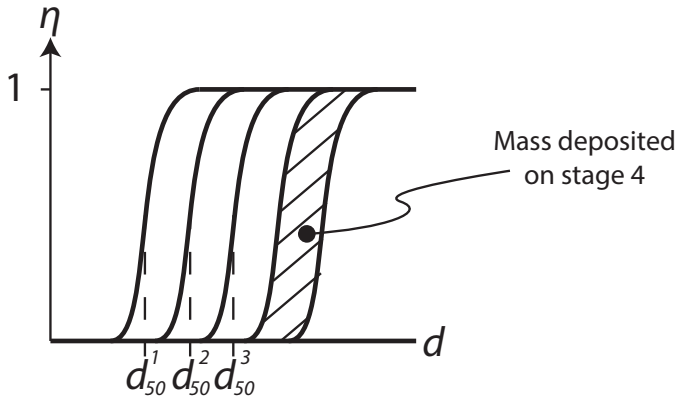

Figure 1.6: Typical η versus d plot for a five stage cascade impactor, with the location of d_{50} for the three smallest stages stage marked.

1.4 Goals

This introduction has shown that current aerosol scavenging models poorly predict the experimentally measured single drop scavenging data. Therefore there is a large opportunity to improve both the understanding of the mechanisms involved in single drop aerosol scavenging, as well as to provide modified scavenging models which can better describe the existing scavenging data. Additionally there exists an opportunity to begin work on developing a higher resolution aerosol sizing technique based on the spatial location of particles in an impactor stage deposit.

The goals of the present thesis research are:

1. Using the existing data available from the literature, determine which of the two existing models for inertial scavenging best predicts the available data.

2. Identify which dimensionless parameters are correlated with poor model performance in the inertial regime. This information can then be used to modify the models to better predict measured results, and to identify potential mechanisms which are poorly described by the existing models. Goals (1) and (2) will be covered in Chapter 2, which will show that the model residuals are well correlated with the drop Reynolds number. As drop shape, wake, and oscillations are all also correlated with the Reynolds number and not included in the existing scavenging models, and have not been investigated in detail in the published scavenging work, these are the identified phenomena which will be investigated.

3. Experimentally test the mechanisms identified in goal (2). This will allow for a more rigorous

investigation of these mechanisms which may be playing a role in scavenging. New data is required, as the previous data was not obtained with the intention of exploring these mechanisms and is not presented with sufficient detail to explore these mechanisms. Therefore data will be collected which will investigate previously unexplored aspects of the parameter space, namely the drop shape, oscillations, and wake, which have not been explored either experimentally or analytically by other researchers. This work will be covered in Chapter 3, and it will be shown that drop wake and oscillations play no measurable role in scavenging, while drop shape does play a significant role in scavenging. Based on these measurements an improved scavenging model will be developed to account for the role of drop deformations on scavenging.

4. Explore the deposition patterns in small S/W impactors. Specifically, determine if the ring-shaped patterns observed are robust and predictable, ascertain whether the geometry of the ring patterns can be determined by impactor parameters, and identify the mechanisms governing this phenomena.

Chapter 2

Parametric investigation of inertial aerosol scavenging models

The first goal of this chapter is to determine whether the inertial model due to Slinn[103,104] or the inertial model due to Calvert[16,17] (described in detail below) is more accurate by comparing their predictions to experimentally measured scavenging coefficients, E_m, of previous researchers published in the literature. The second goal of this chapter is to identify additional dimensionless groups that can be used to improve these models so that they better predict E_m. In addition to providing improved versions of the two models, it is hoped that the identified dimensionless groups will help to identify the other physical mechanisms which play a role in the inertially dominant scavenging regime.

2.1 Inertial model descriptions

The present Chapter is focused on models for the inertial mechanism of scavenging. There are only two models used for inertial impaction in the recent literature surveyed:[3,20,28,70,98,121] the model due to Slinn[103,104] and the model due to Calvert.[16,17] Both of these models are empirical fits: the Slinn model for scavenging via inertial impaction is a fit to numerical simulations due to Beard,[8] and the Calvert model for scavenging via inertial impaction is a fit to the experimental results of Walton and Woolcock.[118] Both models are predictions of the contribution of inertial impaction to

the scavenging coefficient E and will be referred to hereinafter as E_S and E_C for Slinn and Calvert, respectively.

Slinn's inertial model is:

$$E_S = \beta \left(\frac{\rho}{\rho_w} \right)^{1/2} \left(\frac{Stk - Stk_*}{Stk - Stk_* + 2/3} \right)^{3/2} \tag{2.1}$$

where β is a step function which limits E_S to only the inertial regime: $\beta = 1$ if $Stk > Stk_*$ and $\beta = 0$ otherwise; ρ is the particle density, ρ_w is the density of water, Stk is the Stokes number:

$$Stk = \frac{\rho d^2 UC}{9D\mu} \tag{2.2}$$

d is the particle diameter, U is the drop velocity, D is the drop diameter, μ is the air dynamic viscosity, C is the Cunningham correction factor:

$$C = 1 + \frac{2\lambda}{d} \left[1.257 + 0.4 \exp\left(\frac{-0.55d}{\lambda} \right) \right] \tag{2.3}$$

λ is the mean free path in air, and Stk_* is the critical Stokes number:

$$Stk_* = \frac{1.2 + \frac{1}{12} \ln(1 + Re_D/2)}{1 + \ln(1 + Re_D/2)} \tag{2.4}$$

where Re_D is the drop diameter based Reynolds number:

$$Re_D = \frac{\rho_a DU}{\mu} \tag{2.5}$$

where ρ_a is the air density, and Stk_* is the value of Stk below which the particle does not possess sufficient inertia to overcome viscosity and will not come into contact with the drop surface.[8,33,36,55] Using a potential flow solution for flow over a drop gives $Stk_* = \frac{1}{12}$,[8,33,36] and Stk_* is slightly greater than unity when using a Stokes flow solution.[8,33,55] Equation (2.4) is obtained via an interpolation scheme between these two solutions.[103,104]

As Eq. (2.1) is an empirical fit to Beard's numerical simulations, it follows that it is subject to the same assumptions as Beard's simulation.[8] Briefly, this simulation traced the path of particles introduced far upstream of a spherical drop, and considered no forces other than those due to the flow and to inertia. These assumptions preclude particle impacts on the drop surface due to the

hydrodynamic barrier effect. Accordingly it was assumed that once any particle came within several microns of the drop, other forces, such as an electrostatic force, would become dominant and allow for the particle to penetrate this barrier. Of note, this simulation is identical to the simulation of Langmuir,[55] however due to advances in computing technology it was solved with greater precision. Also, this simulation implicitly assumed that there was no particle bounce off, so that all particles which contact the drop are removed from the system.

The second inertial model is that due to Calvert:

$$E_C = \left(\frac{Stk}{Stk + 0.35} \right)^2 \tag{2.6}$$

Calvert's model is an empirical fit to the experimental data of Walton and Woolcock[118] which was obtained from pendant drops and therefore may not be perfectly representative of falling drops, making the application of Calvert's model to falling drops problematic. For example, pendant drops don't experience the same drop oscillations as falling drops, and the wake structure behind a pendant drop will differ from that of a falling drop. Furthermore, the data of Walton and Woolcock[118] only spanned $0.05 \leq Stk \leq 1.32$; therefore applying the Calvert model outside of this range may cause problems as well. It should be noted in passing that Calvert's model does not include the critical Stokes number, and the author makes no statement that the model should not be used below this value.[16,17] This uncertainty of application is of no bearing here, however, since this Chapter is only concerned with the inertial range.

2.2 Comparisons of previous experimental work

Numerous experimental studies of particle scavenging by drops exist, however many of these studies do not provide data for $Stk > Stk_*$,[3,5,15,41,42,52,53,116,119] and therefore will not be included in the present analysis of inertial regime scavenging. The inertial regime experimental studies considered here are the work of Quŕel *et al.*,[77] Chate and Kamra,[59] Pranesha and Kamra,[74] Leong *et al.*,[56] Starr and Mason,[78] and Gunn and Hitschfeld,[40] who performed experiments in the inertial regime using fall towers. Walton and Woolcock[118] performed experiments in the inertial regime in a vertical wind tunnel. Other inertial regime studies include Ranz and Wong,[80] Hahner *et al.*,[32] and Waldenmaier[117] who performed experiments in the inertial regime using horizontal wind tunnels. These studies, however, presented scavenging results only in terms of Stk and D, and due

to the flow geometry it could not be assumed that the experiments took place at terminal velocity. This made it impossible to compute groups such as Re_D, which were needed to compare their results to the model predictions, and so they are not considered further hereinafter.

To compare the measured scavenging coefficients, E_m, obtained from the studies cited above, to the model predictions, E_C and E_S, Stk and Re_D were computed from the data provided for each reported data point in the experimental studies cited above, and were then inserted into Eqs. (2.1) and (2.6) to provide E_S and E_C, respectively. Any data that fell outside of the inertial regime were ignored. All reported data were assumed to have been obtained at standard temperature and pressure. For the fall tower studies, the relative velocity between the drop and particles was assumed to be terminal, with the terminal velocity computed using the equation developed by Beard.[6]

The model predictions E_S and E_C are plotted against E_m in Fig. 2.1. Two figures of merit are used to evaluate the similarity of the model to the data. The first is the correlation coefficient:

$$r = \frac{\sum (x_i - \bar{x})(y_i - \bar{y})}{\sqrt{\sum (x_i - \bar{x})^2}\sqrt{\sum (y_i - \bar{y})^2}} \tag{2.7}$$

The second figure of merit is the standard error of fit of the data to a unity slope line:

$$S = \sqrt{\frac{\sum (y_i - F(x_i))^2)}{n-2}} \tag{2.8}$$

In the above equations x_i are the experimental measurements, y_i are the model predictions, and F is the unity slope line. Values for r and S are presented in Fig. 2.1. To provide a more meaningful comparison of the predictive capability of the two models presented in Fig. 2.1, E_S and E_C were multiplied by a constant that minimized the vertical deviation of the data from the unity slope line. This constant was obtained from the vertical intercept of a least-squares regression on the data in log space. This procedure ensured that the magnitude of r and S were determined by failures of the functional form of E_S and E_C, and not by the lack of a simple multiplicative constant. This constant is included in the label of the ordinate in Fig. 2.1.

As Fig. 2.1 shows, the Calvert model does a better job of predicting the data as measured by both r and S. It is noted that the Calvert model is empirically based upon a subset of the data used here, namely the Walton and Woolcock data set. Hence, it is possible that the better performance of the Calvert model is due to the presence of data used in developing the model. To determine if this was the case, the Walton and Woolcock data was removed and new r and S were

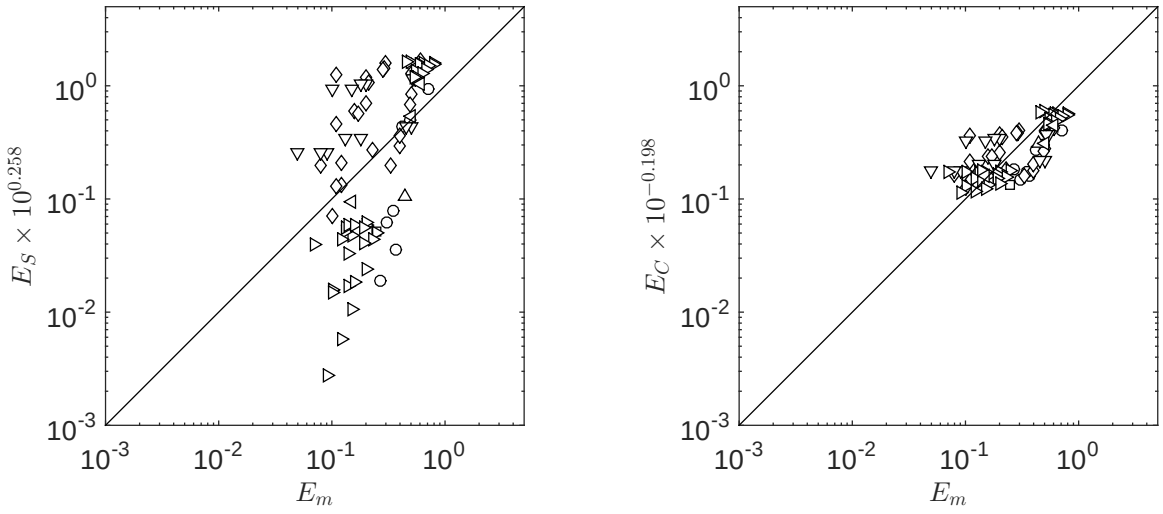

(a) Slinn model: $r = 0.587$, $S = 0.598$

(b) Calvert model: $r = 0.717$, $S = 0.213$

Figure 2.1: Predicted versus measured scavenging coefficients comparing (a) Slinn's model and (b) Calvert's model. The data sets are: ○ Walton and Woolcock 1960,[118] □ Quérel *et al.* 2013,[77] ◇ Chate and Kamra 1997,[59] ▽ Pranesha and Kamra 1996,[74] △ Leong *et al.* 1982,[56] Starr and Mason 1966,[78] and ◁ Gunn and Hitschfeld 1950.[40] The Calvert model has better agreement with the surveyed scavenging measurements by virtue of the larger value of r and the smaller value of S for that model. Only experimental data falling within the inertial regime were used.

calculated for both models, giving $r = 0.624$ and $S = 0.588$ for E_S and $r = 0.747$ and $S = 0.207$ for E_C, confirming that the Calvert model is the preferred model for predicting scavenging. This result satisfies the first goal of this Chapter, which was to determine which of the two models investigated is preferred for predicting scavenging in the inertial regime.

2.3 Analytical comparison of predicted and measured scavenging data

In order to improve the models of Slinn and Calvert, the log space residual error, e, was computed for each model, where e is defined as:

$$e = \log_{10}(E_m) - \log_{10}(E) \tag{2.9}$$

Note that the prefactor from Fig. 2.1 is not used in this equation nor in subsequent equations for e. This residual was related to each of six dimensionless groups ψ, five of which were identified via a Buckingham Pi analysis, as described below. Specifically, e was related to the dimensionless groups

ψ via a the power law:

$$e = f_1(\psi) = A\psi^b + B \tag{2.10}$$

where (A, b, B) were found via nonlinear least squares regression. The goodness of the fit was quantified via r and S. This was done for each of the six ψ considered and the ψ with the largest r and smallest S were deemed to contribute the most to the residual error and were then used to create an improved model E':

$$E' = E \times 10^{f_1(\psi)} \tag{2.11}$$

The above process was then repeated, generating a new residual $f_2(\psi)$ for the revised model and correcting it to form a twice-improved model, E''. This process was continued until the most correlated ψ yielded a correlation coefficient that was less than 0.60. Such a cutoff was needed to give a definite end to the above procedure. The value of 0.6 was somewhat arbitrary; cutoff values smaller than 0.60 resulted in models that were excessively complex and did not visually improve the collapse of the data to the unity slope line in plots such as that presented in Fig. 2.1.

As noted above, five of the ψ were obtained using a Buckingham Pi analysis. Assuming that E is a function of D, d, ρ, ρ_a, μ, U, gravitational acceleration, g, and the particle diffusivity, $\mathcal{D}$, then E will be a function of the five dimensionless groups: Re_d, Re_D, Stk, the Péclet number, Pe, and the Froude number, Fr. Additionally a relative Stokes number, Stk_r was also developed for this analysis:

$$Stk_r = \log_{10}\left(\frac{Stk}{Stk_*}\right) \tag{2.12}$$

which cannot be obtained from the Buckingham Pi analysis. This dimensionless group is a measure of the particle's inertia relative to the critical value, and is a measure of how far into the inertial regime an experimental condition lies. It was thought to provide a measure of inertia potentially better than Stk alone, a supposition borne out by the following results.

The resulting functions for the first iteration of the above process, f_1, are presented in Tables 2.1 and 2.2 for the Slinn and Calvert models, respectively. Note that the subscripts S and C will be used for Slinn and Calvert, respectively. These tables show that the two model residuals are best

ψ	r	S	$f_1(\psi)$
Stk_r	0.854	0.312	$-3.07Stk_r^{0.173} + 2.72$
Stk	0.784	0.374	$0.0694Stk^{-2.38} - 0.231$
Pe	0.740	0.405	$-1.98 \times 10^{-12}Pe^{1.18} + 0.714$
Re_d	0.701	0.429	$-0.747Re_d^{0.64} + 1.4$
Re_D	0.647	0.458	$-1.19 \times 10^{-6}Re_D^{1.72} + 0.613$
Fr	0.114	0.598	$3.19 \times 10^{13}Fr^{-6.64} + 0.25$

Table 2.1: Correlations of various dimensionless groups for the residual of E_S.

ψ	r	S	$f_1(\psi)$
Re_D	0.633	0.166	$-4.15 \times 10^{-16}Re_D^{4.35} - 0.101$
Pe	0.463	0.190	$-3.7 \times 10^{-16}Pe^{1.49} - 0.107$
Fr	0.326	0.203	$3.19 \times 10^{-3}Fr^{0.517} - 0.35$
Re_d	0.187	0.211	$-0.065Re_d^{0.683} - 0.095$
Stk	0.084	0.214	$5.14 \times 10^{-3}Stk^{1.69} - 0.207$
Stk_r	0.055	0.214	$-9.94 \times 10^{-5}Stk_r^{-0.885} - 0.196$

Table 2.2: Correlations of various dimensionless groups for the residual of E_C.

described by different dimensionless groups: e_S is best described by Stk_r and e_C is best described by Re_D.

Tables 2.3 and 2.4 present the residual, e', between E_m and E':

$$e' = \log_{10}(E_m) - \log_{10}(E') \tag{2.13}$$

as well as the power law relationships, $f_2(\psi)$, relating ψ and e'. As Table 2.4 shows, the modified Calvert model is not well correlated with any of the investigated dimensionless groups, its correlation coefficient being less than 0.60 for all ψ considered. Thus, the modified Calvert model is E'_C:

$$E'_C = E_C \times 10^{-4.15\times10^{-16}Re_D^{4.35}} \times 10^{-0.101} \tag{2.14}$$

Table 2.3 shows a significant correlation between e'_S and Re_D, and so the above process was

ψ	r	S	$f_2(\psi)$
Re_D	0.803	0.186	$-2.61 \times 10^{-14}Re_D^{3.9} + 0.185$
Pe	0.567	0.257	$-6.68 \times 10^{-16}Pe^{1.49} + 0.162$
Stk_r	0.272	0.301	$-6.06 \times 10^{-15}Stk_r^{-4.11} + 0.009$
Stk	0.260	0.302	$7.24 \times 10^{-6}Stk^{-8.15} - 0.036$
Fr	0.192	0.307	$9.89 \times 10^{-8}Fr^{1.55} - 0.020$
Re_d	0.158	0.308	$-0.098Re_d^{0.59} + 0.144$

Table 2.3: Correlations of various dimensionless groups for the residual of E'_S.

ψ	r	S	$f_2(\psi)$
Fr	0.432	0.15	$0.584Fr^{0.0913} - 1.140$
Re_D	0.263	0.160	$0.395Re_D^{0.052} - 0.549$
Stk_r	0.229	0.162	$-0.063Stk_r^{-0.217} + 0.091$
Pe	0.167	0.164	$0.060Pe^{0.069} - 0.263$
Stk	0.141	0.165	$-4.69 \times 10^{-24} Stk^{-38.3}$
Re_d	0.130	0.165	$-0.169Re_d^{-0.202} + 0.153$

Table 2.4: Correlations of various dimensionless groups for the residual of E'_C.

ψ	r	S	$f_3(\psi)$
Stk_r	0.566	0.153	$-8.04 \times 10^{-15} Stk_r^{-4.11} + 0.011$
Re_d	0.389	0.171	$-0.222Re_d^{-0.504} + 0.179$
Fr	0.349	0.174	$-3.78Fr^{-0.384} + 0.232$
Re_D	0.325	0.176	$-0.731Re_D^{-0.451} + 0.057$
Pe	0.322	0.176	$-276Pe^{-0.399} + 0.070$
Stk	0.201	0.182	$0.032Stk^{0.978} - 0.034$

Table 2.5: Correlations of various dimensionless groups for the residual of E''_S.

repeated yet again for that model, resulting in the correlations shown in Table 2.5. As all of the correlation coefficients are less than 0.60 in Table 2.5, the doubly modified model is considered as the revised Slinn model:

$$E''_S = E'_S \times 10^{f_2(Re_D)} \tag{2.15}$$

or, via substitution:

$$E''_S = E_S \times 10^{-3.07 Stk_r^{0.173}} \times 10^{-2.61 \times 10^{-14} Re_D^{3.9}} \times 10^{2.905} \tag{2.16}$$

Equations (2.16) and (2.14) are the improved versions of the Slinn and Calvert models, respectively, which achieve the second goal of this Chapter, to improve upon the accuracy of their original versions. These equations are reproduced below:

$$E^*_S = E''_S = E_S \times 10^{-3.07 Stk_r^{0.173}} \times 10^{-2.61 \times 10^{-14} Re_D^{3.9}} \times 10^{2.905} \tag{2.17}$$

$$E^*_C = E'_C = E_C \times 10^{-4.15 \times 10^{-16} Re_D^{4.35}} \times 10^{-0.101} \tag{2.18}$$

Plots of the original and improved Slinn and Calvert models are presented in Fig. 2.2.

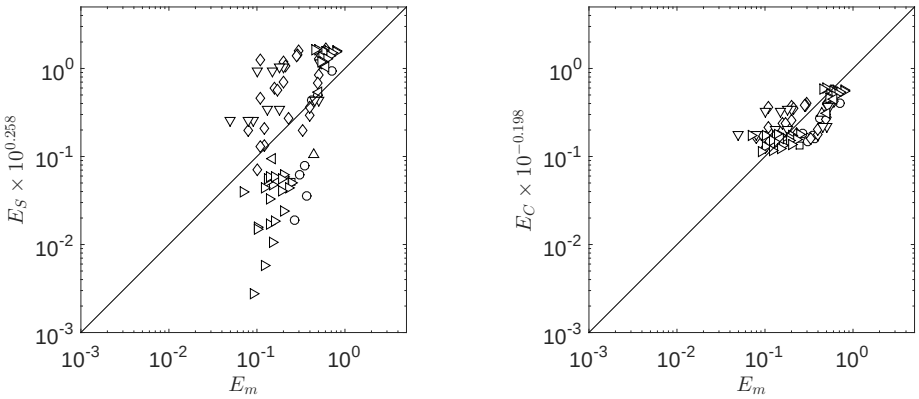

(a) $r = 0.587, S = 0.598$

(b) $r = 0.717, S = 0.213$

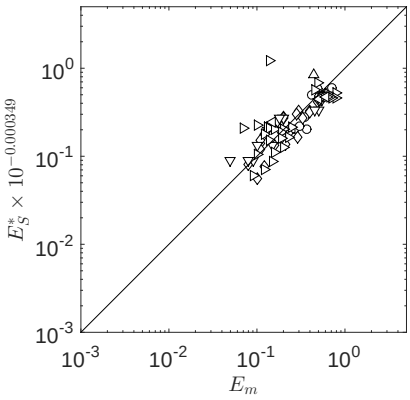

(c) $r = 0.806, S = 0.185$

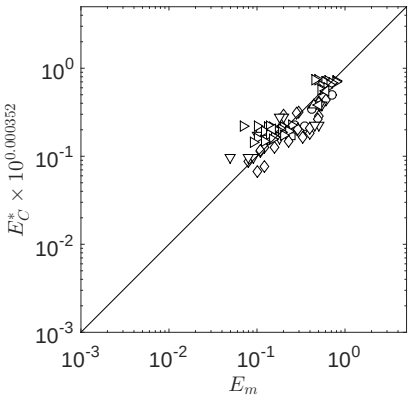

(d) $r = 0.842, S = 0.165$

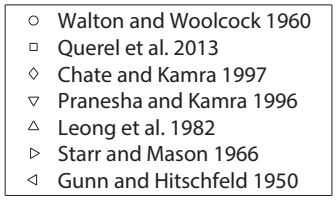

Figure 2.2: Plots of model prediction versus experimental data: (a) and (b) are the unmodified Slinn and Calvert models, respectively; (c) and (d) are the final, modified Slinn and Calvert models, respectively.

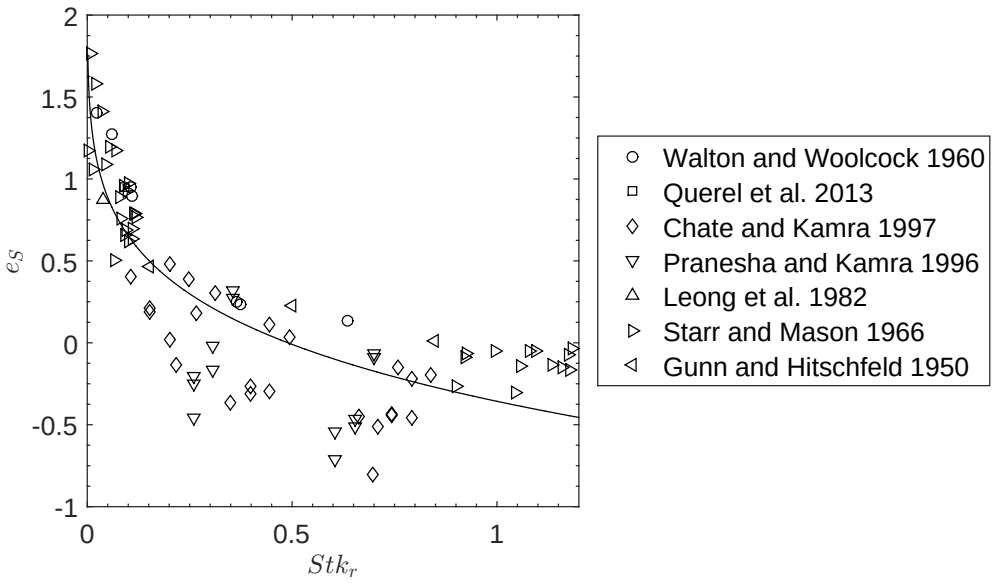

Figure 2.3: Relationship between the residual, e_S, and Stk_r for the unmodified Slinn model, E_S.

2.4 Significance of identified parameters

The question of whether the dimensionless groups used in revising the equations of Slinn and Calvert may provide insight on scavenging in the inertial regime is now addressed. Two dimensionless groups, Stk_r and Re_D, are used to revise the models. Stk_r is discussed first.

Figure 2.3 presents the residual, e_S, versus Stk_r, showing that e_S is high when Stk_r is near zero, but decreases as as Stk_r increases. This implies that E_S under-predicts scavenging near the transition to the inertial regime, but improves as Stk_r increases. This indicates that there exists some mechanism that is not well accounted for in E_S which plays a role in scavenging during the transition to inertially dominated scavenging. In comparison, Stk_r is the least well correlated dimensionless group for e_C, indicating that E_C describes this mechanism well.

Recall that E_S is solely based upon inertial impaction simulations by Beard,[8,103] while E_C is solely based upon experimental measurements of particle collection by pendant drops performed by Walton and Woolcock.[16,118] This provides information regarding what additional mechanisms could be contributing to scavenging in the transition to the inertial regime. The fact that e_C is uncorrelated to Stk_r for even freely falling drops indicates that this mechanism is likely present for both pendant drops and for drops in free fall. This rules out any mechanisms which rely on the

down stream side of the drop, as that is where a pendant drop would be supported. It also likely rules out any mechanism related to drop oscillations as a pendant drop will be relatively pinned due to its support.

A possible mechanism fitting these requirements would be the inertial compression of the particle phase on the front hemisphere of the drop. This mechanism is an inertial enhancement of diffusional deposition caused by inertially increasing the particle concentration near the drop surface. It was proposed by de la Mora and Rosner,[30] and would correspond to larger scavenging near $Stk_r = 0$. This is because as particles approach the drop they will deviate from their streamlines due to inertia; as Stk_r increases this deviation becomes larger and the resulting scavenging increases. However, at low Stk_r very few particles will be deflected enough to allow for inertial impaction on the drop. Instead the majority of affected particles will become more closely packed near the drop surface, resulting in an increase in the local concentration of particles near the drop surface relative to the freestream concentration. Because of the particle phase compression there is an increased concentration gradient near the drop, which will result in a greater mass transfer of the particle phase to the drop surface via diffusional deposition.

The contribution of this mechanism to scavenging will diminish, however, as the inertia of the particles is increased. This is due to two mechanisms: first more particles will be scavenged due to inertial impaction as Stk increases; second, as Stk increases the required time for a particle to travel around the drop will become significantly shorter than its relaxation time, meaning that there will be less time for the inertial compression of the particle phase to enhance mass transfer to the drop surface. As this mechanism would be present in any of the experimental measurements considered here, and it agrees with the trend in Fig. 2.3, it is a possible explanation for some of the residual observed with the Slinn model.

The other dimensionless group that was well correlated with the model residuals was Re_D, as shown in Tables 2.2 and 2.3. Figure 2.4 presents plots of the residual versus Re_D for both models, showing similar behavior for both models. Hence, the mechanism which Re_D describes is most likely not accounted for by either model. A possible mechanism that could account for this trend is wake capture of particles. Wake capture occurs when a particle traverses the front end of the drop without being scavenged but is then pulled into the recirculating region in the drop wake and is ultimately deposited on the back side of the drop after one or more passes in this recirculating region. Wake capture is often used to explain scatter in experimental data.[5,38,77,120] However there has been no

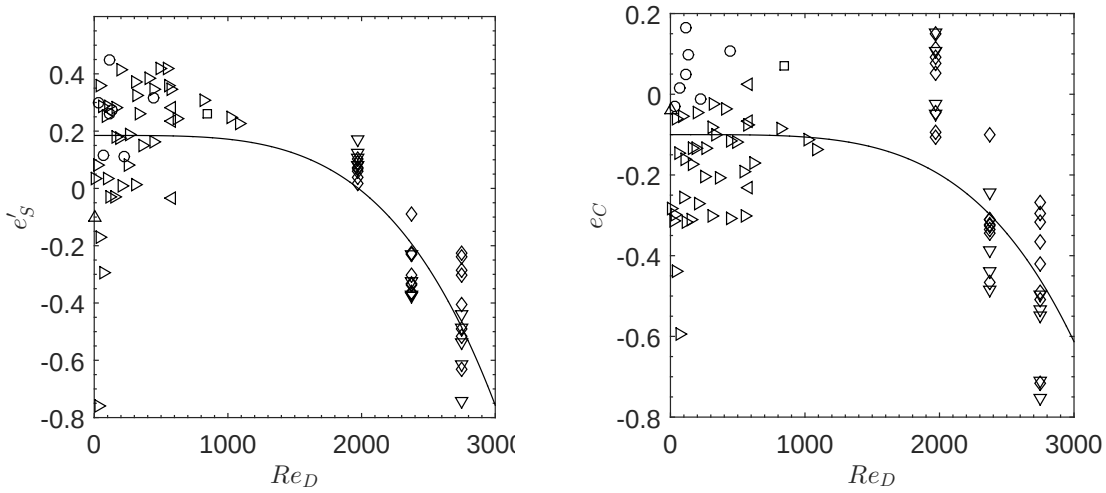

(a) (b)

Figure 2.4: Plots of residual versus Re_D for: (a) the Slinn model, and (b) the Calvert model. The data sets are: ○ Walton and Woolcock 1960,[118] □ Quérel *et al.* 2013,[77] ◇ Chate and Kamra 1997,[59] ▽ Pranesha and Kamra 1996,[74] △ Leong *et al.* 1982,[56] Starr and Mason 1966,[78] and ◁ Gunn and Hitschfeld 1950.[40]

rigorous study of the wake capture of particles by a falling drop. Sakamoto and Haniu[89] showed that the wake dynamics for a sphere are primarily a function of Re_D, with vortex shedding beginning to occur at $Re_D \sim 600$. This corresponds with the trends in Fig. 2.4, as there is a large drop off in the residual for $Re_D > 600$, which is in the vortex shedding regime. If wake capture is playing a significant role in particle scavenging it would follow that once the wake becomes unstable during vortex shedding the likelihood of particle capture by this method is reduced significantly, and would lead to the observed decrease in the residual. Furthermore, wake capture of particles is not included in Beard's simulations, and is unlikely to have an effect in Walton and Woolcock's data due to their experimental apparatus, which used a vertical wind tunnel, and, instead of a freely floating drop, a pendent drop. This drop was supported with a fixed structure which would make the wake of these experiments different from that of a freely falling drop. Because the observed trend approximately matches the expected trend for the onset of vortex shedding and because it is reasonable to conclude that this mechanism is not accounted for in either model, it is possible that wake capture plays a role in scavenging in the inertial regime.

2.5 Model findings

This Chapter has shown that the Calvert model better predicts published experimental scavenging data in the inertial regime. Modifications to the two models are given in Eqs. (2.16) and (2.14), both of which better describe the measured results than either unmodified model. Two mechanisms other than inertial impaction were identified to be playing a measurable role in scavenging within the inertial regime based upon the parametric study of the model residuals conducted. The dimensionless group Stk_r indicates an inertial mechanism at play, likely the compression of the particle phase near the front hemisphere of the drop. The dimensionless group Re_D indicates an advective mechanism at play, perhaps wake dynamics due to the drop off at high Re_D. Further experimental investigation is required to confirm that these are, in fact, the correct mechanisms described by the identified dimensionless groups.

Chapter 3

Experimental study of drop shape and wake effects on particle scavenging

As was shown in the previous Chapter,the large deviations between the data and predictions provided by scavenging models shown in Fig. 1.3 can be partly attributed to the model predictions not having been calculated at the same conditions as the experimental data, this accounts for only part of the discrepancy. The cause of most of these deviations is still unclear. One possible contributor to the deviations of experimental data from the models of particle scavenging by drops is the fact that the models presume a spherical drop shape, while falling drops attain an oblate shape due to aerodynamic forces and gravity, this means that the streamlines approaching the drop will not be the same as those in the model, and therefore the inertial component may be incompletely captured. Furthermore, falling drops oscillate about an equilibrium shape as they fall. Finally, drops can have a wake, depending on their Reynolds number, and this wake can be attached or exhibit vortex shedding; the vortex shedding in turn can potentially couple to drop shape oscillations. All of this is not accounted for in the models of particle scavenging described in the Introduction. The goal of this portion of the thesis research is to determine if, and to what degree, the above characteristics of falling drops might contribute to deviations of experimental data from model predictions. It should be noted that charging[5] and turbulent diffusion[122] have been proposed as additional mechanisms

which can cause these deviations, however turbulence cannot account for these deviations, as the data presented in Fig. 1.3 was collected with either drops in the laminar section of a vertical wind tunnel, or for single drops falling though quiescent fluid. Additionally charge neutralization was used in the majority of the data in this figure, therefore charging cannot account for these deviations either.

The deformation of a drop is measured by the axis ratio:

$$\alpha = \frac{v}{h} \tag{3.1}$$

where h and v are the horizontal and vertical radii of the drop, respectively; for a sphere $\alpha = 1$. This deformation becomes significant for drops where $D > 1$ mm, since the surface tension of water renders deviations from sphericity minimal below this diameter. The $D > 1$ mm diameter range comprises a significant fraction of raindrops. For example, using the Marshall-Palmer[65] drop size distribution at a rain rate of 10 mm/hr, 28% of drops will be larger than 1 mm, and 73% of the mass of rain falls in this $D > 1$ mm range. Drop deformation increases with D. For example a 1 mm, 2 mm, and 3 mm drop will be deformed to $\alpha = 0.98$, 0.93, and 0.86, respectively, under equilibrium conditions.[2,6]

As noted above, wakes can exist in the flow behind the drop. The wake is primarily determined by the drop Reynolds number:

$$Re = \frac{\rho_a U D}{2\mu} \tag{3.2}$$

where ρ_a is the air density (note that drop radius is the characteristic length in Eq. (3.2)). For spheres, an attached wake appears at $Re \sim 100$, and vortex shedding begins at $Re \sim 300$.[89] This wake behavior has been observed in simulated raindrops with diameters between 1.65 and 2.91 mm.[91] For raindrops falling at their terminal velocity, as determined by the terminal velocity equation due to Beard,[6] Re will be sufficiently large to form an attached wake for drops larger than 0.6 mm, and for drops larger than 1.1 mm Re will be large enough for vortex shedding to occur. Applying this to the Marshall-Palmer distribution for 10 mm/hr rain, this corresponds to 75% of raindrops having a wake, and 23% of drops experiencing vortex shedding. Additionally, a drop will not have a stationary shape as it falls, and will instead oscillate about its equilibrium shape, having a change in α throughout its oscillation cycle on the order of 0.02[2,108] and these shape oscillations can be coupled to the vortex shedding of the drop wake,[9] as noted above.

Of the data presented in Fig. 1.3, the majority of the experiments were for drops where Re was in the range where a wake is expected, however none of these works investigated the role of wakes in detail. Additionally, some of these experiments had drops large enough to exhibit deformation, however this is the minority of experiments and the role of α on E was not investigated. Finally, although the experiments with drops large enough to exhibit deformation will also exhibit oscillation, none of these experiments explored the role of drop oscillation on scavenging. Hence, since drop deformations, wakes, and drop shape oscillations all can exist in falling drops, but their influence on scavenging has not been quantified in the existing analytical or experimental literature, a new scavenging measurement method was developed to quantify these effects. This method used an acoustically levitated drop which can easily be exposed to aerosol laden flows. This approach differs from the previously used scavenging measurement techniques of fall towers and vertical wind tunnels in that U and the drop axis ratio, α, can both be adjusted independently of D, which is not the case for a freely falling drop.[2,6,7] The drop velocity and shape combine to determine Re, which can classify the wake size[124] and vortex shedding of the wake.[89] As the previous chapter showed, model residuals with the existing published scavenging measurements correlate well with Re, which it was hypothesized might be due to wake effects. This will be explored in more detail using the ultrasonic levitation method, herein. Additionally this method can be used to induce shape oscillations in the drop, and the magnitude of these oscillations can be independently controlled, allowing this effect to be exaggerated to more clearly determine if it affects scavenging. Therefore the significance to scavenging of static and dynamic drop shape and drop wake can be evaluated.

Finally, it is noted that the experiments presented in Fig. 1.3 were all conducted for water drops in unsaturated conditions. In such a situation evaporation can cause concentration gradients which leads to diffusiophoretic effects, as well as evaporative cooling of the drop surface, leading to thermophoretic effects. In the experiments presented below, propylene glycol was use instead of the more typical water to minimize the evaporation of the drop during these tests. This approach minimizes phoretic scavenging contributions, which may otherwise dominate effects due to shape deformation, shape oscillations, and wakes.

3.1 Scavenging method

An ultrasonic standing wave field was used to levitate a stationary drop within a particle laden jet. Unlike fall tower and wind tunnel experiments which have been traditionally used in drop scavenging experiments, this approach allowed for control of drop shape independent from drop diameter, and easily allowed for exploration of both sub-terminal and super-terminal velocities. The apparatus used is shown in Fig. 3.1.

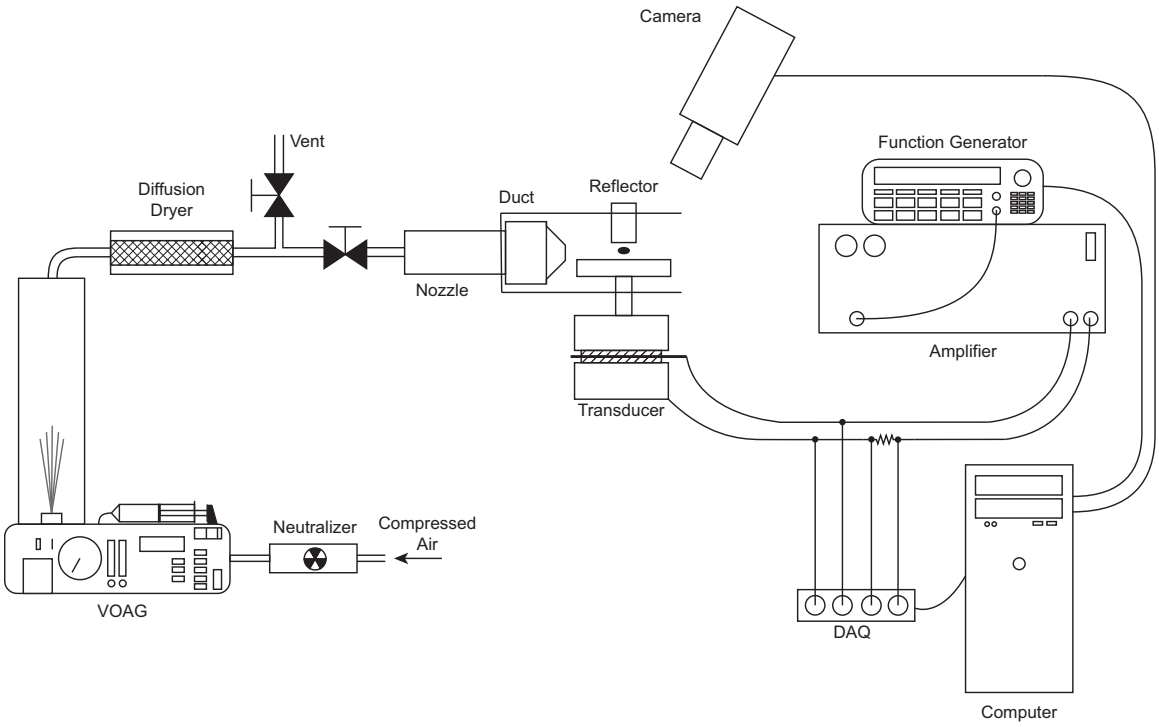

Figure 3.1: Diagram of the experimental apparatus used to determine the scavenging coefficient of individual drops.

Ultrasonic levitation involves the development of an acoustic standing wave field. At the nodes of such a field, the acoustic radiation force will support an object.[27,49,50,100] The ultrasonic standing wave field supporting the drop was created using an ultrasonic transducer, a reflector, a function generator, an amplifier, and custom control software. A more detailed description of the transducer and controller is given in Appendix B. The transducer consisted of two piezoelectric disks with a copper plate between them, an aluminum back mass, and an emitter, following the design of Trinh.[110] To drive the transducer an Agilent 33220A function generator was used to generate a sine wave at the resonant frequency of the transducer/reflector system, approximately 30 kHz,

with a peak to peak amplitude of 300-900 mV. The function generator output was amplified using a Krohn-Hite 7500 amplifier to produce a signal of 30-90 V which was applied to the ultrasonic transducer. The transducer, thus driven, emitted a nominally planar wave which was reflected by the reflector, consisting of a flat aluminum surface placed an integer number of half wave lengths from the transducer. This produced the ultrasonic standing wave field used to levitate droplets in the experiment.

The resonance frequency of the transducer was found to drift with time as the transducer was operated. To account for this, a software control was implemented in LabView. To ensure that the applied signal was at the resonant frequency of the transducer/reflector system, the applied voltage and current were measured with a Measurements Computing USB-2020 DAC at a sample rate of 10 MHz. The phase shift between the voltage and current was calculated, and the driving frequency was subsequently adjusted to reduce the phase shift to zero, maximizing the power delivered to the transducer. This change in frequency resulted in a change in wavelength of the ultrasonic wave, and as the gap between the reflector and transducer is fixed, this process therefore detuned the ultrasonic wave field to no longer be a pure standing wave. This change in the reflector gap tuning is very small, on the order of μm and had far less impact on the ability to levitate drops than keeping the frequency constant and not compensating for the drift in the transducer resonance frequency. This method allowed a droplet to be levitated for several hours, which is significantly longer than the duration of a typical scavenging experiment. A study was performed and determine there was negligible influence of the ultrasonic field on the particles flowing over the drop; details of this study are presented in Appendix C.

With a drop floating in the field, the drop shape was adjusted by changing the voltage applied to the transducer. Increasing the applied voltage resulted in more oblate drops while decreasing the field resulted in more spherical drops. To induce drop oscillations, the applied voltage was amplitude modulated (AM) causing the drop to oscillate at the AM frequency. Modulation frequencies were applied at both the drop natural frequency as described by Lamb[54] and at the frequency which produced the largest amplitude oscillations, which was typically approximately half the frequency predicted by Lamb. These frequencies were of order $\mathcal{O}$(100 Hz). That the larger amplitude oscillations were observed to occur below the Lamb frequency is likely due to the non-spherical shape of the drops in this experiment. Shen *et al.* have shown that there is a decrease in the frequency of sectoral oscillations in an oblate drop with increasing drop deformation,[101,102] so it stands to

reason that a similar dependence would hold for oblate-prolate oscillations. Additionally Trinh and Wang have shown that for large amplitude, driven oscillations, such as those in this experiment, the observed peak in oscillation amplitude is dependent on the degree of modulation of the ultrasonic field,[109] indicating that some shift from the Lamb frequency should be expected. In both oscillating cases the jet velocity was adjusted so that the vortex shedding frequency, as predicted by Sakamoto and Haniu,[89] was an integer multiple of the imposed drop oscillation frequency.

It should be noted that while the above method produces an oblate spheroid, which is the shape a raindrop will achieve as it falls, the direction of the flow relative to the minor axis of the drop is orthogonal to the flow condition in rain. This deviation from the natural condition of rain notwithstanding, this approach is useful because it allows for independent control the drop Reynolds number, shape, and oscillations, which are all typically determined by the drop diameter. By decoupling these parameters, this method allows for the impact of these parameters to be more easily explored independently, and therefore to pinpoint their influence on scavenging. Additionally, a method was developed to account for the change in drop orientation relative to that of a freely falling droplet, as is described in Section 3.3.

Propylene glycol was used as the drop fluid in these experiments to minimize change in the drop size due to evaporation over the course of the experiments. Initial runs conducted with water as the working fluid resulted in significant changes in drop diameter over the course of an experiment. For example, over ten minutes a 91% reduction in drop volume was observed for water. This corresponds to a 55% reduction in drop diameter. By using the relatively nonvolatile propylene glycol the drop volume only decreased by 7% in the same duration, which corresponds to only a 2% reduction in diameter. This allowed for longer runs, which collected more total particles, thereby increasing the signal measurement and reducing the uncertainty in E, without introducing confounding effects due to changing D through the course of the run. This approach had the added benefit of essentially removing phoretic effects, which may otherwise mask the influence of drop shape, wake, and oscillations. As an aside, in addition to the lower evaporation rate of propylene glycol compared to water, propylene glycol also has a smaller surface tension by a factor of 1.5 and a larger dynamic viscosity by a a factor of 40. The differences in these properties may cause the shape and oscillations for the drops herein to be different than for water drops, however this is assumed to have negligible impact on the scavenging measurements herein, as both the drop shape and oscillations will be measured directly, and not predicted from a model.

Images of the levitated drop were obtained during each experiment using a Cooke Sensicam high speed camera, and were used to measure drop diameter. An example drop image is shown in Fig. 3.2. A Canny edge detection algorithm[19] was applied to the image and the horizontal and vertical extents of the drop were found, giving the major and minor radii of the drop, h and v respectively, which were used to obtain α as defined in Eq. (3.1). The three dimensional shape of the drop was assumed to be an oblate spheroid where the equivolume spherical diameter,

$$D = 2h\alpha^{1/3} \tag{3.3}$$

was used to quantify the drop size.

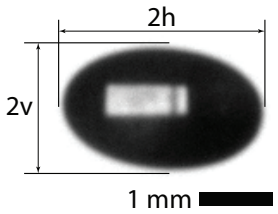

Figure 3.2: Back lit image of a levitated drop, with the light visible through the drop.

To produce monodisperse particles, a vibrating orifice aerosol generator (TSI 3450 VOAG) was used. The VOAG produces monodisperse droplets by exciting a liquid jet, thereby causing the jet to break up into a stream of monodisperse droplets. The jet is composed of a solution containing a nonvolatile solute (a dye), and the resulting monodisperse droplets evaporate, producing a monodisperse aerosol with the particle diameter controlled primarily by the concentration of the dye according to:[12]

$$d = \left(\frac{6QC}{\pi f}\right)^{1/3} \tag{3.4}$$

where Q is the VOAG solution flowrate, C is the dye volume concentration, and f is the vibration frequency of the VOAG. Disodium fluorescein was chosen as the dye because it is a well characterized fluorescent dye, which fluoresces when excited by ultraviolet light. It has a peak excitation wavelength of 480 nm and a peak emission wavelength of 525 nm.[90] The intensity of the emitted light depends on the intensity of the absorbed light, the dye concentration, and the solution pH.[67] Taking advantage of this response, a fluorometer (Turner Designs, PicoFlour 8000-003) was used to

measure the concentration of the sample, which in turn was used to determine the mass, or number of particles present, in the sample. More details of the fluorometer measurements are presented in Appendix D.

The air entering the VOAG was first directed through a krypton 85 neutralizer (TSI 2077A) to remove charge from the generated particles so that any electrostatic attraction could be assumed negligible between particles or between particles and drops. The particles were then transported through a diffusion dryer to ensure that the particles were entirely dry. Following the diffusion dryer the flow exited via a nozzle based on the design of Bell and Mehta,[10] which produced a uniform velocity particle laden jet. Design and validation details of this nozzle are presented in Appendix E. The particle concentration was determined by clamping a 3 μm Teflon filter (Millipore) over the nozzle outlet for 1 minute to collect particles. This filter was then removed, washed with 10 ml doubly distilled water, and 40 μl of the resulting solution was transferred to a cuvette containing 40 μl of 10 pH buffer solution. The resulting solution was then measured with a fluorometer to determine the concentration of disodium fluorescein particles in the jet. Drops were typically levitated in the particle laden jet flow for 5 - 20 minutes at which time the drop exhibited visible color change. At this time the drop was then removed from the field and mixed with 0.2 ml of 10 pH buffer solution. The resulting solution was measured with a fluorometer to determine the amount of disodium fluorescein collected by the drop. Using these two measurements, the scavenging coefficient was determined according to the equation:

$$E = \frac{f_d V_d t_f A_j}{f_f V_f t_d A_d} \tag{3.5}$$

where f_d and f_f are the disodium fluorescein concentrations for the drop and filter respectively, V_d and V_f are the dilution volumes for the drop and filter respectively, t_f and t_d are the duration of the filter test and drop exposure respectively, and A_j and A_d are the cross sectional area of the jet and the projected area of the drop respectively.

The above experimental method produces E which can exceed unity, a violation of conservation of mass. This increased scavenging is due to three artifacts in the experimental method, which yield artificially high scavenging. The first contributor is a decrease in flowrate through the system when the filter was mounted relative to the flowrate when the drop was exposed to the jet. For large particle diameter d, this drop in flowrate caused additional particle settling in the

particle generator and a decrease in the mass collected by the filter, resulting in under-counting of the fluorescein concentration in the jet. The second artifact is due to the ultrasonic field, which compresses the particle trajectories as they travel from the nozzle to the drop. Just as the acoustic radiation force compresses the drop in the node of the standing wave field, so too are the particles pushed toward the node. This results in a larger fluorescein concentration in the region of the drop than was measured by the filter. The third artifact was a change in the tube geometry between the diffusion dryer and the nozzle when the nozzle was moved for the filter collection portion of the experiments which resulted in increased deposition in the tubing, resulting in an under counting of the fluorescein concentration of the jet the drop was exposed to.

These three contributors were corrected to provide the actual E presented in the Scavenging results Section, below. Details of these corrections are presented in Appendix F, but briefly to correct for the drop in flowrate during the filter collection, experiments were conducted to measure filter collection at the actual flow rate of each experiment. Compression of particle trajectories in the ultrasonic standing wave field was accounted for by simulating the particle trajectories as they travel from the nozzle to the drop. The acoustic radiation force exerted by the acoustic field on the particles was calculated using the formulation due to Settnes and Bruus,[100] and the drag experienced by the particles was calculated as Stokes drag. A correction factor was created from these simulations by taking the ratio of the particle concentration at the nozzle exit and at the drop location. Finally the increased deposition in the tubing during the filter collection due to different tube bend geometry upstream of the nozzle was accounted for using the tube deposition model due to McFarland *et al.*[66]

3.2 Scavenging results

A plot of E versus Stk is presented in Fig. 3.3, where E is the corrected scavenging coefficient, as described above, and Stk is computed using the diameter of an equivolume sphere (Eq. (3.3)) for the length scale in Eq. (1.3). The value of α for each data point is indicated via grayscale. This data shows that E increases monotonically with Stk, for the range of Stk explored here. Also, for a given Stk, E increases with decreasing α (E increases as the drops become less spherical). This trend with α becomes more pronounced for smaller Stk. This is seen more clearly when the data is binned in Stokes space and E is plotted against α within the Stk bin, as shown in Fig. 3.4. This

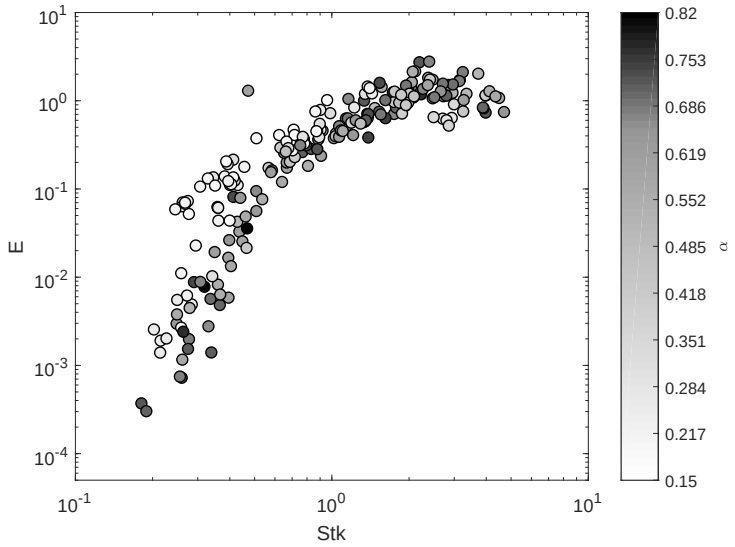

Figure 3.3: Plot of scavenging coefficient, E, versus Stokes number, Stk, where Stk is based on the equivalent volume spherical diameter of the drop. The marker grayscale intensity indicates the drop axis ratio, α for each data point. These data are for stationary drops.

figure shows, again, that E decreases with α, and that this decrease is largest for small Stk.

To see how Re, and therefore wake effects, influence E the data from Fig. 3.3 was binned evenly in Stk and plotted against Re, where the length scale in Re was the drop minor diameter. A series of E versus Re plots were obtained, similar to those presented in Fig. 3.4, which showed essentially no sensitivity of E to Re. The Reynolds number ranged from $Re = 100 - 500$, which includes both the attached wake and the vortex shedding wake regimes.[89] To further demonstrate the insensitivity of E to Re, the data within each Stk bin was fit to an exponential function of the form:

$$E = Ce^{(\phi_{Re})(Re)} \tag{3.6}$$

so that the exponent ϕ_{Re} quantifies the sensitivity of E to Re. This exponent is plotted against the average value of Stk for each Stk bin in Fig. 3.5. As the figure shows, $\phi_{Re} = 0$ within the 95% confidence intervals of the data, further demonstrating that E is insensitive to Re. This suggests that wake effects are not playing a measurable role in scavenging, though it should be noted that for $Stk < 0.6$, the 95% confidence intervals are large. Hence, it is possible that there is some sensitivity to Re in this range that the data is unable to reveal. It is noted that this insensitivity to Re holds

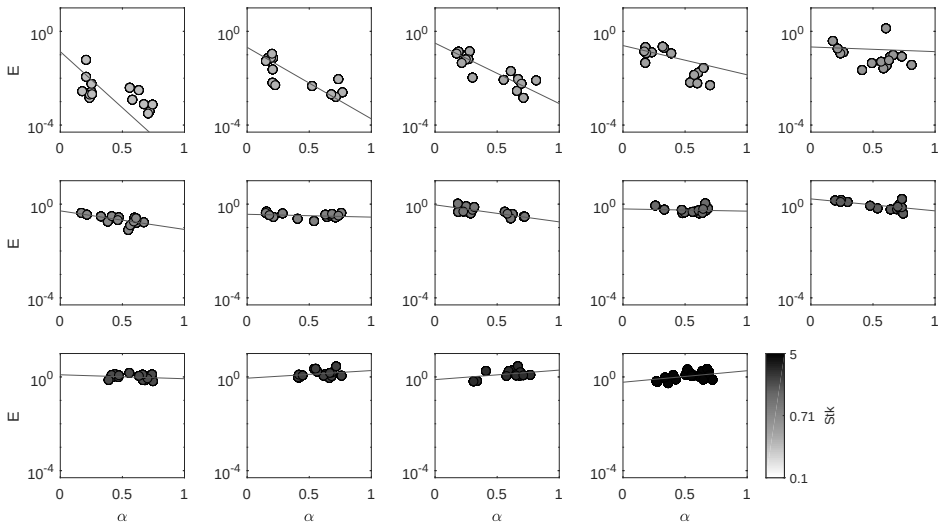

Figure 3.4: Plots of scavenging coefficient E versus drop axis ratio α, for stationary drops. Each plot is for a fixed range of Stk. The Stokes number increases from left to right and top to bottom encompassing the entirety of the data in Fig. 3.3, binned evenly in Stk. The Stk bins are: (0.182:0.263); (0.263:0.308); (0.308:0.363); (0.363:0.415); (0.416:0.511); (0.511:0.699); (0.699:0.812); (0.812:1.025); (1.025:1.302); (1.302:1.546); (1.546:1.931); (1.931:2.209); (2.209:4.719). The Stokes number for each data point is indicated by grayscale.

true for drops in the attached wake regime and drops in the vortex shedding regime.

In addition to the stationary drop scavenging measurements presented in Fig. 3.3, measurements were made while acoustically inducing oscillations in the drops. These drop oscillations were excited at both the natural frequency predicted by Lamb[54] as well as the frequency which gave the largest change in α for a given field strength. For all oscillating drops the jet velocity was adjusted so that the vortex shedding frequency, as predicted by the Strouhal number measurements of Sakamoto and Haniu[89] for a sphere, was 4 times the drop oscillation frequency, meaning that a second harmonic coupling between vortex shedding and drop oscillation was attained. Figure 3.6 shows the binned, non-oscillating measurements from Fig. 3.3 as well as E for the oscillating drops. The degree of oscillation is quantified by $\Delta\alpha$ the difference between the maximum and minimum α during the oscillation cycle and is indicated via grayscale in Fig. 3.6. As this figure shows, the oscillating scavenging measurements appear to be insensitive to the degree of oscillation, which is larger in all cases than that of a freely falling raindrop.[2] The oscillating data also does not deviate from the non-oscillating data within the confidence intervals. All this indicates that drop oscillations do not materially contribute to scavenging.

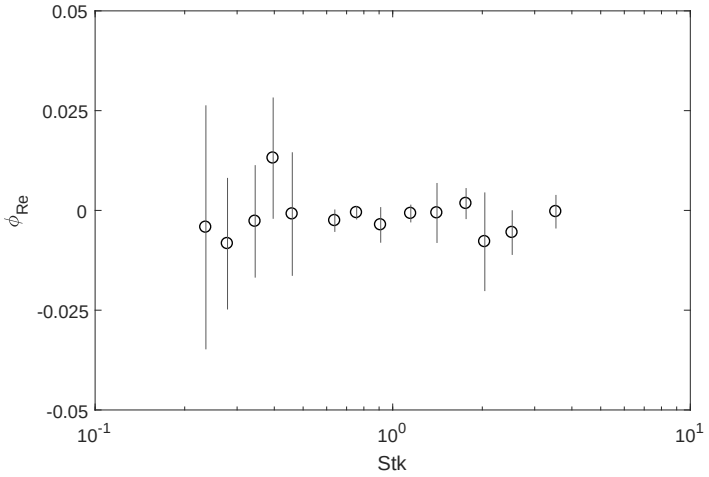

Figure 3.5: Plot of ϕ_{Re}, which quantifies the sensitivity of E to Re, versus Stk based on E versus α fits of the data in Fig. 3.4 binned in Stk. The vertical bars show the 95% confidence intervals of ϕ_{Re}.

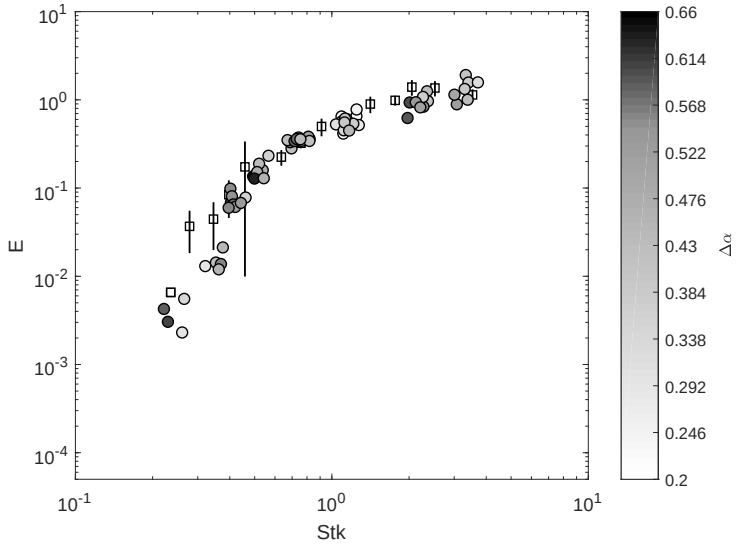

Figure 3.6: Plot of the bin average E of the non-oscillating data (squares) from Fig. 3.3 and the oscillating drop measurements (circles). For the oscillating data the grayscale value indicates the magnitude of the drop oscillations as measured by the difference between the maximum and minimum α of the oscillation cycle, $\Delta\alpha$. The vertical bars show the 95% confidence interval of the non-oscillating drop bins.

3.3 Application of results to models

An important result presented above is the increase in E with decreasing α shown in Figs. 3.3 and 3.4, which occurs at small Stk. This result can be explained by considering how the drop surface area and projected area change with α. For a fixed volume drop in the flow conditions of this experiment (where α is always < 1) the surface area decreases with increasing α, while the projected area increases with increasing α. This leads to a situation where there is more area available for particles to deposit at small α, while simultaneously decreasing the number of particles in the flow path of the drop. This can explain the observed increase in scavenging for small α and Stk, where the scavenging contribution is dominated by surface area dependent mechanisms such as diffusional deposition, and phoretic forces. However, at large Stk, inertia becomes dominant, which is a projected-area-dependent mechanism. For this case both the number of particles encountering the drop and the removal of particles by the drop are determined from the projected area. Since E is a ratio of these two values, large Stk scavenging should therefore be independent of α, which is in fact the case, as Figs. 3.3 and 3.4 show.

The above explanation can be shown more formally with the following scaling argument, similar to the method used by Slinn and Hales.[105] First, the rate a drop is exposed to particles, $\dot{n}_t$, is assumed to scale as:

$$\dot{n}_t \sim n_\infty U A_d \tag{3.7}$$

where n_∞ is the freestream particle concentration and A_d is the projected area of the drop. Also, it is assumed that the drop collects these particles at the rate $\dot{n}_c$, which is given by the relationship:

$$\dot{n}_c \sim \Gamma A \tag{3.8}$$

where Γ is the net flux, in particles per time per area, of particles moving from the air to the drop at the drop surface due to all scavenging mechanisms, which is assumed to be independent of drop shape, and A is the area of the drop surface which is interacting with the particles, and is dependent on drop shape, α. For large Stk, where inertia is dominant, $A = A_d$, but for smaller Stk, $A = A_S$,

where A_S is the drop surface area. The ratio of $\dot{n_c}$ to $\dot{n_t}$ gives E, so for large Stk E will scale as:

$$E \sim \frac{\Gamma A_d}{n_\infty U A_d} = \frac{\Gamma}{n_\infty U} \tag{3.9}$$

and E is insensitive to drop shape, while for small Stk E will scale as:

$$E \sim \frac{\Gamma A_s}{n_\infty U A_d} \tag{3.10}$$

which is a function of α, and E will increase as α decreases. These large and small Stk relations agree with the experimental observations.

The above relationship can be used to relate scavenging for a sphere, E_σ, with scavenging for an oblate spheroid (such as the data herein), E_o. This is accomplished by substituting geometric expressions for the surface and cross sectional areas of oblate spheroids and spheres into Eq. (3.10), and taking the ratio of E_σ and E_o, which gives the relationship:

$$\frac{E_\sigma}{E_o} = \frac{2\alpha}{1 + \frac{\alpha^2}{\sqrt{1-\alpha^2}} \tanh^{-1}\left(\sqrt{1-\alpha^2}\right)} \tag{3.11}$$

The full derivation of this model is shown in Appendix G, and a plot of the relationship between E_σ and E_o is shown in Fig. 3.10. This relationship can be expanded further to predict how an oblate spheroid will scale with the measured Stk in the present study, which will allow for quantifying the influence of the drop shape in the scavenging results. This is done by making the following assumptions. First, that E primarily scales with the Stokes number, and second that the Stokes number characteristic length for an oblate spheroid, Stk_o, is the major diameter, which can be related to the equivolume spherical Stokes number (Stk) according to:

$$\frac{Stk}{Stk_o} = \alpha^{1/3}. \tag{3.12}$$

By combining Eqs. (3.11) and (3.12) the following relationship is obtained:

$$E_o \sim Stk \left[\frac{1 + \frac{\alpha^2}{\sqrt{1-\alpha^2}} \tanh^{-1}\left(\sqrt{1-\alpha^2}\right)}{2\alpha^{2/3}} \right] \tag{3.13}$$

Equation (3.13) show that the scavenging of an oblate spheroid, such as a falling drop, is a function of Stk and α, and scales directly with Stk. An important result is that multiplying Stk by the

portion of Eq. (3.13) in square brackets yields the Stokes number using the Sauter mean diameter, D_S, as the characteristic length for the drop, where:

$$D_S = 6\frac{V}{A_s} \tag{3.14}$$

where V is the drop volume, and A_s is the drop surface area. Therefore, for deformed drops in the flow conditions of this study, Eq. (3.13) can be rewritten as:

$$E_o \sim Stk_S \tag{3.15}$$

where Stk_S is the Sauter mean diameter based Stokes number. To the author's knowledge this is the first use of D_S as the length scale for Stk. The Sauter mean diameter is the diameter of a sphere which preserves the surface area to volume ratio of an oblate spheroid, and is commonly used in surface area dominated processes.[43] Replotting the data obtained herein against the Sauter mean diameter based Stokes number, Stk_S, it is seen that E becomes insensitive to α, as shown in Fig. 3.7. To better visualize this trend this data was binned in Stk_S space and plotted as a function of α, then curve fit to an exponential function of the following form:

$$E = Ce^{(\phi_\alpha)(\alpha)} \tag{3.16}$$

The resulting ϕ_α are plotted against Stk_S in Fig. 3.8. The confidence intervals for ϕ_α span zero for all Stk_S indicating that there is no statistically significant sensitivity of E to α. Therefore E for an arbitrarily deformed drop in the flow orientation of the experiment herein can be used to predict the scavenging for a spherical drop, and vice-versa.

Because Stk_S accounts so well for α effects, it can also be used to better understand the oscillating results from this experiment. Recalculating the data from Fig. 3.6 to be based on Stk_S removes any influence of drop shape on E as discussed above. This highlights any potential dynamic effects in the collected data. Figure 3.9 presents the data thus treated, showing the binned, stationary measurements from Fig. 3.7 as well as the measured oscillating drops. The oscillating data was evaluated at Stk_S for the average α of the oscillation cycle. As this figure shows, the oscillating measurements agree well with the stationary results. This gives further indication that the previous conclusion of E insensitivity to wake effects is valid, as for the exaggerated case tested here there is

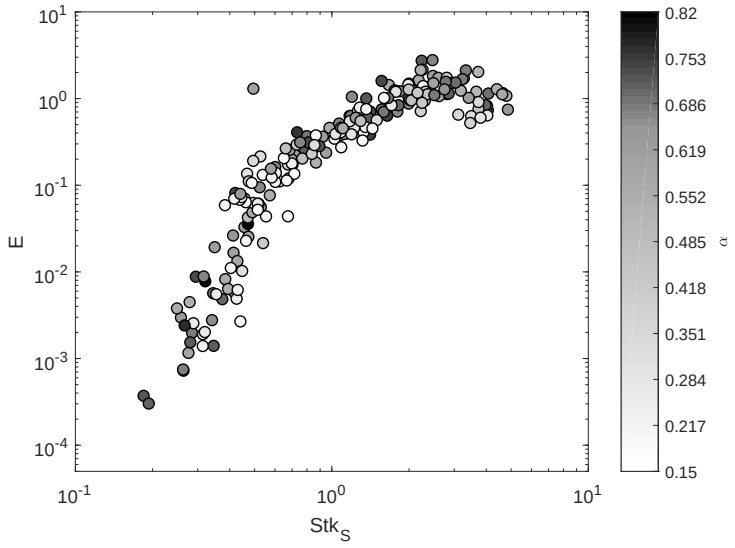

Figure 3.7: Plot of the measured scavenging as a function of Stk_S calculated with the Sauter mean diameter for stationary drops.

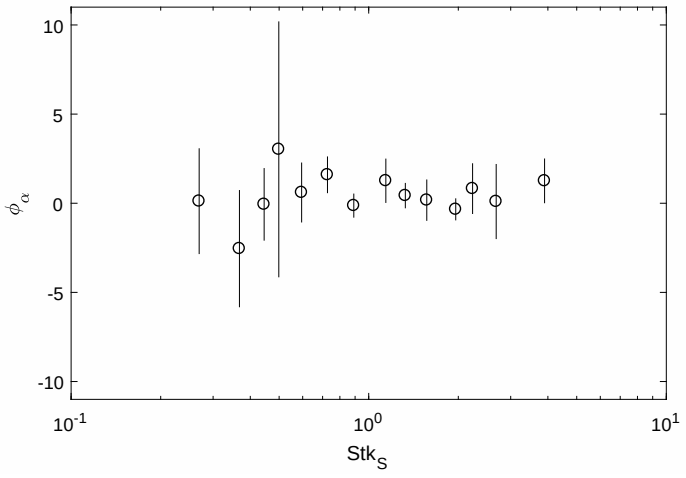

Figure 3.8: Plot of ϕ_α, which quantifies the sensitivity of E to α, versus of Stk_S, based on E versus α fits of the data in Fig. 3.7 binned in Stk_S. The vertical bars show the 95% confidence intervals of ϕ_α.

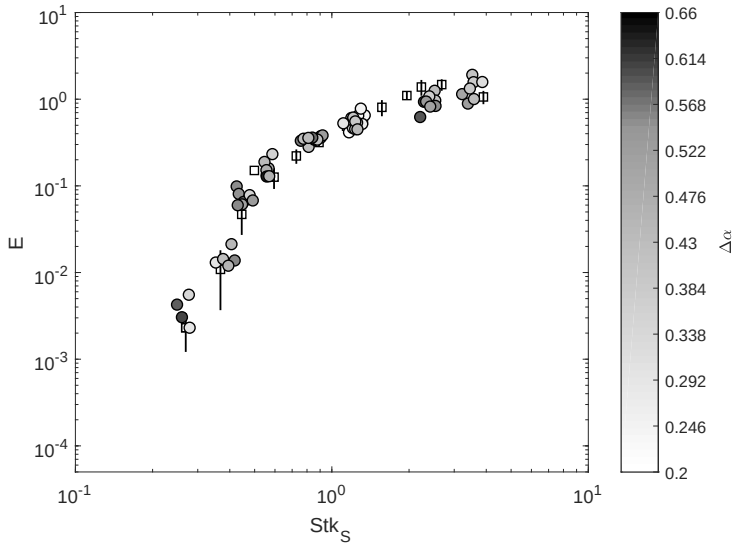

Figure 3.9: Plot of the bin average of the non-oscillating data (squares) from Fig. 3.7 and the oscillating drop measurements (circles). For the oscillating data the grayscale indicates the magnitude of the drop oscillations as measured by $\Delta\alpha$, the difference between the maximum and minimum α of the oscillation cycle. The vertical bars show the 95% confidence interval of the non-oscillating drop bins.

no measurable discrepancy between the stationary and oscillating drop conditions. As there appears to be no wake effects, the correlation between the model residuals and Re identified in Chapter 2[34,35] must be due to some other Re dependent process which is not present in this experiment. As the drop fluid in this experiment was chosen to have a very low evaporation rate to facilitate longer scavenging durations to minimize uncertainty, and the convective mass and heat transfer from an evaporating drop are both Re dependent, it is likely that phoretic forces are the cause of the Re correlated model residuals found in Chapter 2. This hypothesis is explored in greater detail later in this Chapter.

As the above analysis has been demonstrated to account for α in the present data, it can be concluded that the assumptions made in Eqs. (3.7) and (3.8) are sufficient to capture the relevant physics of the scavenging process. Recall that the orientation of the drops used in this investigation are rotated perpendicular relative to the flow direction compared to the orientation of a freely falling rain drop. Therefore the results above will not apply directly to rain. However, the same analysis used to obtain Eq. (3.11) can be applied for the orientation of a raindrop. That is, the ratio can be obtained for the scavenging coefficient for a sphere, E_σ, to the scavenging coefficient of an oblate

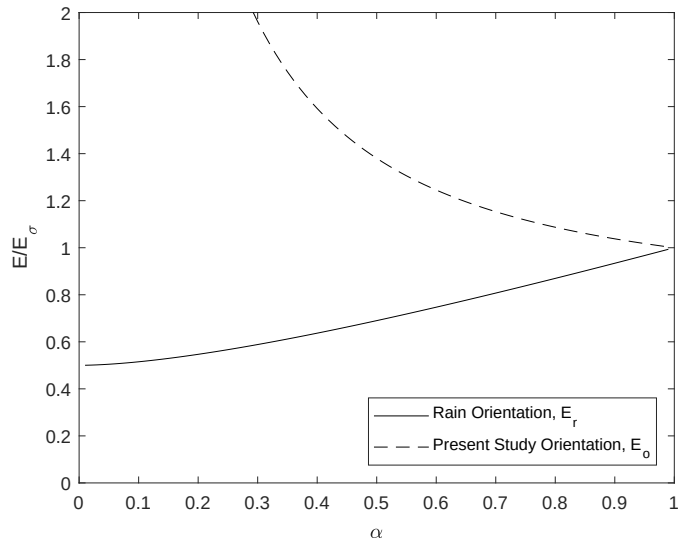

Figure 3.10: Plot of E/E_σ versus α, where E_σ is spherical drop scavenging, and E represents either deformed drop scavenging in the flow orientation expected in rain, E_r, or in the flow orientation of the present study, E_o.

spheroid oriented as raindrops are, E_r. This ratio is:

$$\frac{E_\sigma}{E_r} = \frac{2}{1 + \frac{\alpha^2}{\sqrt{1-\alpha^2}} \tanh^{-1}\left(\sqrt{1-\alpha^2}\right)} \tag{3.17}$$

The details of this derivation are presented in Appendix G, and a plot of the relationship between E_σ and E_r versus α is shown in Fig. 3.10. This relationship allows for spherical scavenging models to be used to predict scavenging for arbitrarily deformed rain drops and vice-versa. For example, the scavenging models discussed in the Introduction all assume a spherical drop and by applying Eq. (3.17) to these model predictions, new predictions can be obtained which account for the deformations present in rain. This will be shown below. Another example of the utility of the analysis presented in Eqs. (3.11) and (3.17), is that they can be used to directly compare the present data with that of previous researchers, by converting both sets of measured scavenging to equivalent spherical scavenging measurements. This will be presented later in this Discussion.

As noted in the Introduction, raindrops larger than 1 mm will deform due to aerodynamic forces and gravity. Equation (3.17) allows for these drop deformations to be accounted for, and the extent of their influence on particle removal in a rain event to therefore be quantified. The following analysis is an example which demonstrates this by modeling particle removal in two ways: first by

assuming the rain drops are spherical and applying the models for E without modification; then by accounting for drop deformation to obtain E_r from the spherical E via Eq. (3.17). Comparing the net particle removal in both cases quantifies the impact of drop shape on scavenging. To do this, the raindrop size distribution was obtained using the Marshall-Palmer model,[65] and the shape of each drop diameter was determined using the relationship due to Andsager *et al.*:[2]

$$\alpha(D) = 1.0048 + 0.0057D - 2.628D^2 + 3.682D^3 - 1.677D^4 \tag{3.18}$$

with the units for D in cm. The terminal velocity of each drop diameter was obtained from the model due to Beard.[6] The individual drop E was found using the models described in the Introduction. These models were evaluated in two ways: first for spherical drops with the unmodified models, then accounting for drop deformations by applying Eq. (3.17) to obtain E_r. The particle size distribution was determined from the model due to Clark and Whitby.[23] Following Slinn,[104] the evolution of the particle concentration during a rain event is:

$$n(d,t) = n(d,0)e^{-\Lambda(d)t} \tag{3.19}$$

where n is the particle concentration, t is the rain duration, and Λ is the washout coefficient found by:[104]

$$\Lambda(d) = \int \frac{\pi}{4}(D+d)^2 U(D)E(d,D)N(D)dD \tag{3.20}$$

where N is the drop size distribution. The difference between $n(d,0)$ and $n(d,t)$ gives the modeled particle removal over the course of the rain event. Applying this analysis results in a decrease in modeled particle removal when accounting for the drop shape compared to the calculated removal for spherical drops. The magnitude of this decrease depends on the rain rate and frequency of rain events, therefore to reveal the significance of this analysis, it is applied in two example cases, a U.S. city that experiences high rainfall, and one that experiences low rainfall. For Orlando, FL, the analysis shows that accounting for α results in a decrease of 11,800,000 kg of particles removed per year over the city, which is a 0.3% decrease in predicted particulate removed. When this is applied to the much drier Las Vegas, NV, the prediction accounting for shape effects results in 1,880,000 kg less of particulate removed per year, which is a 0.27% decrease compared with the predicted removal

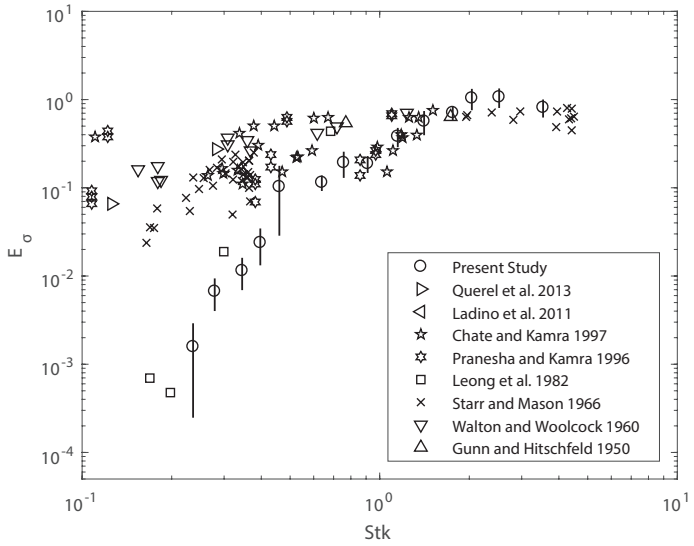

Figure 3.11: Plot of present scavenging measurements and previously published scavenging measurements. All measurements have been adjusted to equivalent spherical scavenging via Eq. (3.11) for the data in the present experiment, and via Eq. (3.17) for the previously published results. The present results have been binned and averaged for clarity, the error bars show the 95% confidence bounds of the averaged results.

from spherical drops. In both cases the difference is large in terms of mass of particulate removed, but small in terms of percentage.

Because Eqs. (3.11) and (3.17) allow for spherical drop scavenging to be extrapolated from arbitrarily deformed drops in both the orientation of the present experiment and of a falling raindrop (which is the orientation for drop fall towers and vertical wind tunnels) respectively, the results of this study can now be readily compared with existing experimental scavenging measurements, as well as scavenging models for spherical drops. Figure 3.11 shows how the data collected herein compares with previously published single drop scavenging measurements in the same Stokes range. To account for drop deformations, the measured E have been adjusted to give the spherical drop equivalent scavenging, E_σ. To minimize clutter, the results from this study have been binned and the averages plotted. The other data presented in this figure comes from the surveyed single drop scavenging literature with measurements of E for $Stk > 0.1$, which is the range of the present study.[40,52,56,59,74,77,78,118]

As Fig. 3.11 shows, although the present analysis collapses the present data with itself, it does not seem to collapse the present data with that of prior researchers at small Stk, where the

present data is up to two orders of magnitude smaller than the majority of other researchers. It should be noted that this separation is small compared to the four decade scatter observed at smaller Stk in the literature data, as shown in Fig. 1.3. The separation between the present results and the previous research is not entirely unexpected, as the conditions of the present study are different from those of previous researchers, with the two most obvious differences being the different shape and flow orientation of the drops, and the different drop fluid, resulting in significantly less drop evaporation. The first difference should be accounted for from Eqs. (3.11) and (3.17), however the lower evaporation rate in the present work is not accounted for in this analysis, nor is it captured in Stk. There are also other differences between the present and literature data which are not captured in Fig. 3.11, such as differences in humidity, d/D, Reynolds, and Schmidt numbers, which are all parameters that appear in various scavenging models, and therefore should have some influence on the measured scavenging. An alternate way to present the data in Fig. 3.11 is to calculate the model prediction for the conditions of each data point and then compare the predicted and measured result. This allows for a more direct comparison of the data as it accounts for other parameters in addition to Stk. Figure 3.12 shows measured E (again, translated to the equivalent spherical value, E_σ, using Eqs. (3.11) and (3.17)) plotted against the predictions for spherical drop scavenging due to the models presented in the Introduction for the conditions of each data point.

As Fig. 3.12 shows there is generally good agreement between the models and the measured values when E_σ is predicted to be greater than 0.1, however as the model predictions for E_σ decrease, the models under predict scavenging for a majority of data points. Of note, there is a slightly different behavior exhibited by the present data compared with that of previous researchers when the measured E_σ deviates from the model prediction. The literature data shows a nearly horizontal band in Fig. 3.12, while the present results show a nearly vertical band. To further investigate the source of these discrepancies, the dominant mechanism of each point was identified, and Fig. 3.12 replotted in Fig. 3.13 with the symbols identifying the dominant scavenging mechanism of each data point, instead of the author.

Figure 3.13 shows that when inertia is dominant the measured scavenging is generally in good agreement with the models, and when inertia is no longer dominant the models no longer predict the measured E well, except for a few points in the present data where interception is dominant. This figure also shows that poor agreement between the models and the literature data occurs when diffusophoresis should be dominant, while the present results are interception dominant when the

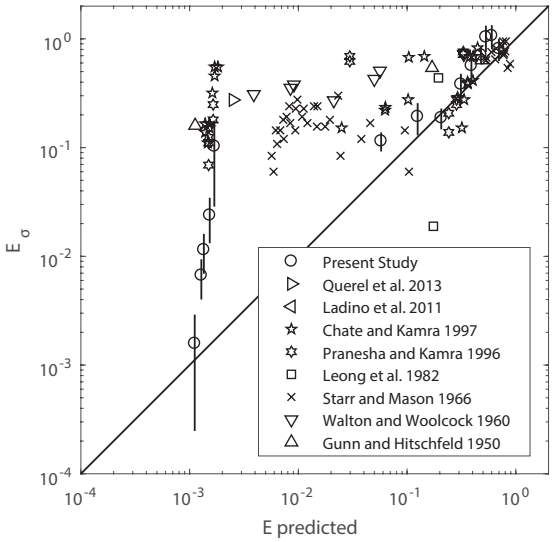

Figure 3.12: Plot of measured versus model predicted scavenging values for the present results, converted to E_σ via Eq. (3.11) (the vertical lines correspond to 95% confidence intervals), as well as those from the literature surveyed, converted to E_σ via Eq. (3.17). The solid line is of unity slope, and corresponds to exact agreement between the measured value and the model prediction.

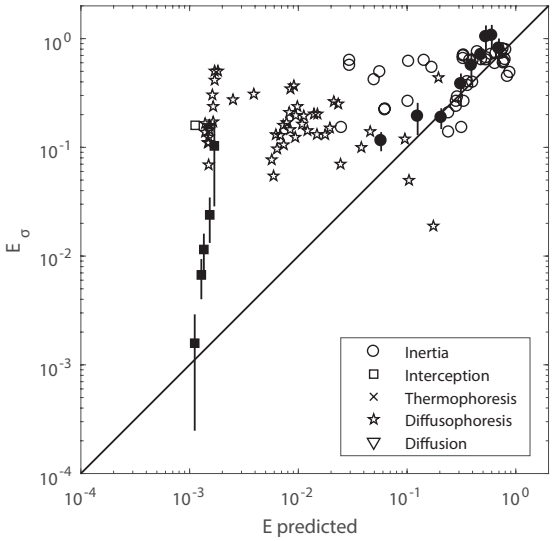

Figure 3.13: Plot of measured versus model predicted scavenging values for the present results, converted to E_σ via Eq. (3.11) (filled symbols, the vertical lines correspond to 95% confidence intervals), as well as those from the literature surveyed, converted to E_σ via Eq. (3.17) (open symbols). The solid line is of unity slope, and corresponds to exact agreement between the measured value and the model prediction. The symbols designate the dominant scavenging mechanism for each data point as determined from the model prediction.

poor model agreement occurs. To better identify the reason for the deviations, the transition from inertial dominance was investigated. The inertial model has a nearly vertical portion near Stk_*, the critical Stokes number, defined in Eq. (2.4), this is shown in Fig. 1.2. Recall that Stk_* defines the lower bound for which inertial scavenging is possible. Near Stk_*, which for the present data is in the range from 0.24 to 0.28, small changes in Stk give large changes in E predicted. The present results with poor model agreement fall just beyond this region of high Stk sensitivity for the inertial contribution to scavenging, and are barely in the interception dominant regime. Several of these points in the present data which show large deviations between the model and measured E are within the measurement uncertainty on Stk of being in this highly Stk sensitive inertially dominant part of the parameter space. This explains the vertical band in the present results seen in Figs. 3.12 and 3.13. Given this, it can be concluded that present data is in good agreement with the existing models contrary to what is shown in Figs. 3.12 and 3.13, which only show the vertical deviation between the measured E and the model predictions, neglecting uncertainty in Stk. This conclusion does not hold for the literature results, however, as when the same amount of uncertainty is applied to Stk for this data there is no similar overlap with the inertial contribution to scavenging. This result can be expected from Figs. 3.12 and 3.13 as the data in poor agreement with the models for the literature data here forms a horizontal band instead of a vertical one. This implies that the diffusiophoretic model is under predicting scavenging in this regime. This is consistent with the findings of other researchers who have also noted under prediction in this region.[3,121,122] As the region of largest discrepancy between the present data and the surveyed data occurs in the diffusiophoretic dominant regime it is worth investigating the differences between the present study and studies with water drops further.

The contributions of diffusiophoretic effects on scavenging are dependent on the drop fluid as well as the humidity of the air the drop is falling through, since as the humidity increases the diffusiophoretic contributions will decrease. For water drops to have diffusiophoretic contributions to scavenging not dominant over interception contributions, as is the case for the present results with propylene glycol, the models discussed above require that for a water drop the air must have a relative humidity greater than 95%. For the diffusiophoretic contributions with a water drop to be as small as with the propylene glycol drops used herein, the air would have to have relative humidity of 98%. The highest relative humidity condition in the literature surveyed was that of Querel *et al.* at 90%, which is still sufficiently low that the diffusiophoretic scavenging is predicted to dominate

interception contributions.

This drastic decrease in E in the absence of diffusiophoretic forces can be significant when considering scavenging in rain or sprays, where there is potential for saturation to occur. For rain, saturation will occur at higher altitudes, however there may be large portions of a raindrop's fall time in which it will experience less than saturated air, and therefore the diffusiophoretic contributions will be significant when calculating scavenging. As the duration of a rain event increases, the fraction of a drop's fall time in saturated air will increase as evaporation of previous raindrops will both increase the moisture content of the air and lower the temperature at increasingly lower altitudes. Therefore the time is limited for which appreciable diffusiophoretic contributions to scavenging occurs in a rain event. This phenomena is also applicable to the design of sprays for scavenging in enclosed spaces, as when saturation is reached the performance of the spray will drop.

3.4 Experimental scavenging findings

The above work shows that it is possible to perform single drop scavenging experiments using an acoustically levitated droplet to obtain scavenging measurements for a single drop. Using this experimental technique the following has been demonstrated. First, the drop wake has no influence on scavenging both in the attached wake and vortex shedding wake regimes as well as for interception dominated and inertial impaction dominated scavenging regimes. Second, the drop shape has some influence on E at small Stk due to an increase in surface area which can interact with particles, however this shape effect can be accounted for by using the Sauter mean diameter as the characteristic length of the drop when calculating Stk, which allows for the comparison of scavenging for deformed drops in the flow orientation of this experiment. Third, a method was developed to extrapolate the equivalent spherical drop scavenging for a deformed drop in the flow orientation of this experiment as well as in the orientation of rain, allowing for direct comparison of scavenging measurements, as well as the use of scavenging models which presume spherical drops to predict scavenging of deformed drops, like those observed in rain. Finally it was shown that by removing diffusiophoretic contributions from an evaporating drop, E, drops significantly. In the absence of these phoretic effects, experiments agree very well with the inertial model of Slinn.

Chapter 4

Ring-shaped deposition patterns in small nozzle-to-plate distance impactors

As was discussed in the Introduction, during the course of the experiments described in Chapter 3, particles were collected with a small nozzle-to-impactor stage spacing. The deposition pattern of these particles took the form of a well defined ring, which upon further investigation had geometry that was a function of the particle size. Recognizing this as an opportunity to improve the resolution of cascade impactors, the following experiments were carried out.

4.1 Impactor ring deposit formation

Experiments were conducted at small S/W for a range of particle diameters to determine if any dimensional characteristics of the rings might be a function of particle diameter. The apparatus used to do this is shown in Fig. 4.1. The particles used in these experiments were composed of disodium fluorescein which were generated using a vibrating orifice aerosol generator (VOAG, TSI Model 3450). The disodium fluorescein was dissolved in a 50/50 water/isopropyl alcohol solvent. This solution was flowed through the VOAG, creating a monodisperse distribution of drops. Upon evaporation of the solvent, a monodisperse particle distribution remained having a diameter, d,

determined by:

$$d = \left(\frac{6QC}{\pi f} \right)^{\frac{1}{3}} \tag{4.1}$$

where C is the solution concentration, Q is the solution flowrate, and f is the vibration frequency of the VOAG orifice.[12] Disodium fluorescein was used since it is a bright green dye which is easily visualized.

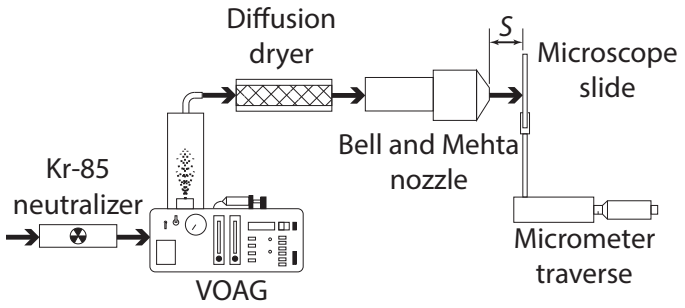

Figure 4.1: Apparatus used to generate monodisperse disodium fluorescein particles and measure the resulting deposition pattern.

As shown in Fig. 4.1, the aerosol stream was convected from the VOAG through a vertically oriented drying column having a diameter of 100 mm using house air. The house air passed through a Kr-85 source (TSI Model 3077A), so that all of the air used in the jet was subjected to charge elimination. The house air had a relative humidity that was typically 5% and which facilitated evaporation of the solvent to create particles. The particles were flowed through a diffusion drier (ATI Model DD250) to ensure that they were fully dry and had a density, ρ, equal to that of pure disodium fluorescein and a diameter predicted by Eq. (4.1). The dry particles were then passed through a nozzle with an exit diameter, W, of 12.7 mm. As shown in Fig. 4.2 this nozzle consisted of three stages, an expansion plenum, followed by a flow straightener comprising packed 3 mm straws approximately 30 mm in length in a 50 mm straight plenum, and then the nozzle whose profile conformed to a fifth order polynomial defined by Bell and Mehta.[10] Wire mesh diffusers with a mesh size of ~ 0.5 mm were installed between each stage. The region surrounding the nozzle orifice had a flat face indicated as F in Fig. 4.2, and which was 2 mm wide. This nozzle is designed to provide a flat velocity profile at its exit. More details regarding this nozzle are presented in Appendix E. The jet exit velocity, U, was measured with a hand held anemometer (TSI Velocicalc).

A microscope slide mounted on a precision translation stage served as the impactor plate. As

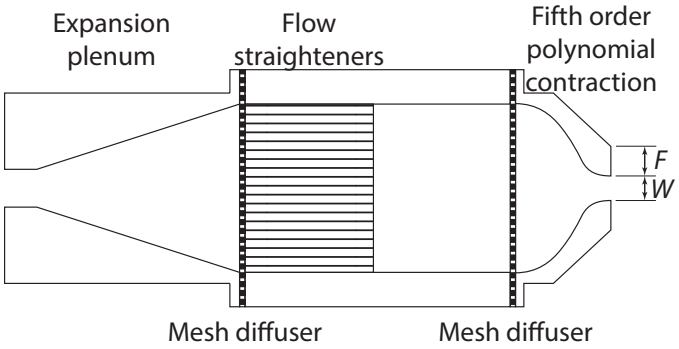

Figure 4.2: Schematic of the Bell and Mehta[10] nozzle used to produce a uniform velocity jet. The diagram is not to scale.

particle bounce was a concern, a sticky coating was applied to the microscope slide to aid in particle retention.[69,111,112] This coating was created by pretreating the slide with a solution of Vaseline brand petroleum jelly dissolved in heptane at a 1:20 volume ratio in a method similar to that used by Sethi and John.[99] The microscope slide was dipped in this solution and then allowed to dry, resulting in a ~ 4 μm thick film of petroleum jelly coating the microscope slide. The spacing between the nozzle and the slide, S, was set to 0.6 mm using the micrometer traverse, giving $S/W = 0.047$. The coated microscope slide was exposed to the aerosol laden jet for a period of time sufficient to allow a visible accumulation of particles on the slide. This duration ranged from 30 seconds to 5 minutes depending on the particle number density in the jet.

Attempts were made to confirm the particle diameter predicted by Eq. (4.1) by imaging the particles deposited on the slide at 10X using a microscope (Leica DM750) with a mounted digital camera (Cannon Rebel T3). However, due to humidity in the laboratory the deposited fluorescein particles, which are very hygroscopic, would begin to absorb water from the laboratory air almost instantly upon removal of the microscope slide from the dry jet air. This would cause the particles to "melt" and either combine with each other on the slide, or grow in diameter. In an attempt to minimize the degree of water absorption by deposited particles during this transition, the microscope was enclosed and flushed with 5% relative humidity air. However when transferring the slides from the jet to the microscope enclosure there was still significant water adsorption from the ambient lab air. When the laboratory air had a relative humidity $> 30\%$, imaging measurements revealed deviations from Eq. (4.1) $> 40\%$ and deviations on the order of 15% for dryer lab conditions. It should be noted that the absorbtion of water and growth of the particles did not occur until after

the particles had deposited on the microscope slide and the microscope slide was removed from the jet apparatus. Hence, none of the absorbtion issues described above affected the particle trajectories or impact location on the slide. In light of the above, Eq. (4.1) was used to obtain d for all of the results presented herein.

To obtain images of the rings, the microscope slides were back-lit and imaged at 1X using a digital camera (Cannon Rebel T3i) with a 65 mm macro lens (Canon MP-E 65mm). The diameter and thickness of the rings were then measured using these 1X images. Measurements obtained from both the 1X and 10X images were generated by importing the captured images into ImageJ.[92] The 1X ring images were measured by manually drawing a circle over the inner and outer diameter of the rings and obtaining a pixel measurement of the diameters, which were then converted to lengths via calibration images of a fine-scaled rule which was imaged at the same location as the microscope slide.

4.2 Observed impactor rings

Representative ring-shaped deposition patterns are presented in Fig. 4.3. This figure shows that the ring inner diameter, outer diameter, and, concomitantly, ring thickness (one-half the outer diameter minus the inner diameter), vary with particle diameter d. Visual observation of Fig. 4.3 shows that the inner diameter gets smaller as the particle diameter increases from 6.16 μm to 12.98 μm. At $d = 12.98$ μm, the inner diameter of the ring has decreased to zero, as the entire circular region is filled in. There are a few anomalies in Fig. 4.3 which warrant discussion. First, the blurred checkerboard pattern in the background of all four images is a result of the LED array which was used to back-light the microscope slides for imaging; the checkerboard pattern is simply an out-of-focus image of this array. Secondly, in Fig. 4.3(b), and to a lesser extent Figs. 4.3(a) and 4.3(c) there is some dust contamination visible. These dust particles are the linear objects visible inside the ring in Fig. 4.3(b), and the large dark particles in Figs. 4.3(a) and 4.3(c). In color images it is clear that these are dust since it is easy to distinguish between the orange-brown fluorescein particles generated in this experiment and the ambient dust, however this distinction is lost when reproduced in grayscale. Third, in Fig. 4.3(a) there is a faint second ring inside the well defined primary ring. This is the result of the particle distribution not being perfectly monodisperse and will be discussed in more detail in Section 4.3. Fourth, in Figs. 4.3 (a) through (c) the top portion

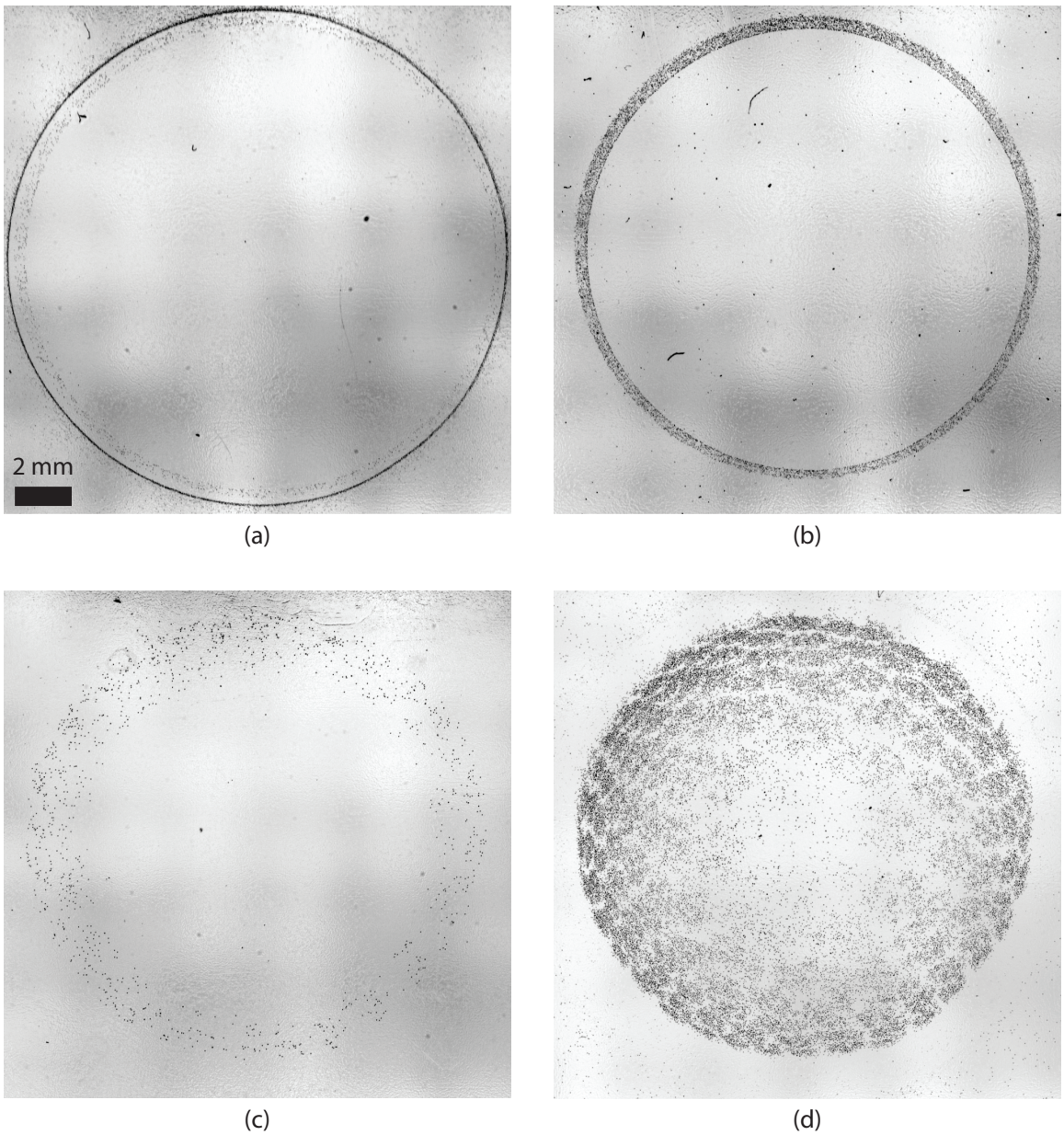

Figure 4.3: Representative particle deposition patterns imaged at 1X magnification for various particle diameters and jet velocities: (a) $d = 6.16$ μm $Stk_W = 0.07$ (b) $d = 7.18$ μm $Stk_W = 0.12$ (c) $d = 12.69$ μm $Stk_W = 0.20$ (d) $d = 12.98$ μm $Stk_W = 0.38$.

of the deposit appears darker than the bottom. This is likely due to a slight cant in the mounting of the slide, making the top $\sim 20\mu$m further from the nozzle than the bottom. Finally, the regular "cell" pattern in the deposit in Fig. 4.3(d) is due to the flow straightener in the nozzle, as there are the same number of "cells" within the deposit as the number of straws used in the flow straightener. Additional images of the ring-shaped deposits similar to those in Fig. 4.3 are presented in Appendix I.

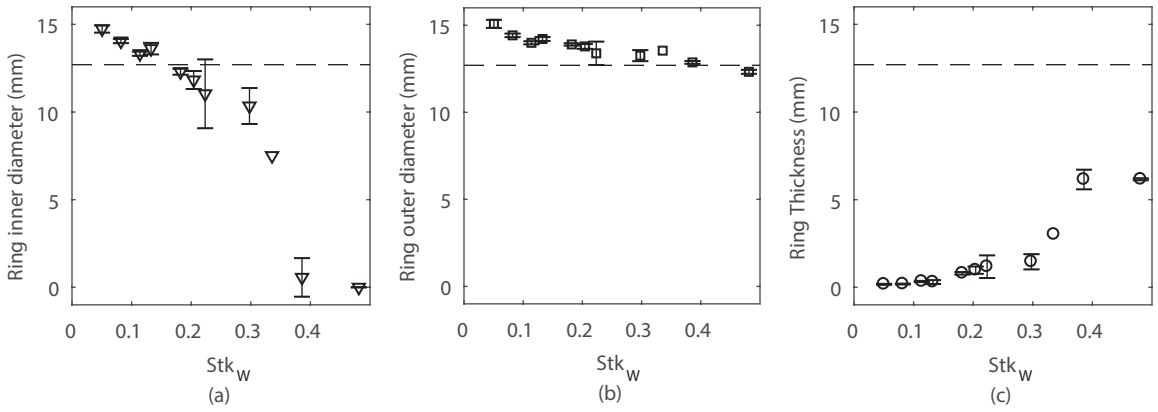

Figure 4.4: Relationship between ring dimensions and Stk_W: (a) Ring inner diameter versus Stk_W; (b) ring outer diameter versus Stk_W; (c) ring thickness versus Stk_W. The nozzle diameter, W is shown as the dashed line.

The particle velocity, U, and aerosol diameter, d, were varied. In Fig. 4.4 the ring dimensions are plotted against the particle Stokes number typically used to characterize impactors:[43,58,64]

$$Stk = \frac{\rho d^2 U}{9\mu W} \tag{4.2}$$

where μ is the dynamic viscosity of air. These plots show the result of 182 deposition rings, binned in Stk_W, with bin widths of 0.03. The error bars show 95% confidence intervals for the ring dimension. As Fig. 4.4(a) shows, the inner diameter of the ring is very sensitive to Stk_W, varying from 15mm to zero as Stk_W increases from 0.05 to 0.49. The ring outer diameter is relatively insensitive to Stk_W, decreasing from $\sim$ 15mm to slightly more than 12mm over the same range of Stk_W. It is noted that no deposition was observed below $Stk_W \sim 0.035$, and at $Stk_W \sim 0.4$ the inner diameter approaches zero and is equal to zero at the largest Stk_W explored giving a ring thickness of $W/2$. This condition

corresponds to a uniform deposition, which would be expected for a traditional impactor. Also of note, for a circular nozzle with $S/W > 1$, d_{50} will occur at $Stk_{50} = 0.24$,[43] and 100% collection of particles occurs at slightly higher Stk_W. Interestingly, this 100% collection would correspond approximately to the point in Stk_W space where the observed depositions from the small S/W impactor tested herein cease to be rings, and become uniform.

To investigate the influence of S/W on the ring dimensions, additional data was gathered at smaller S/W. This data is presented in Appendix H, and sample ring-deposit photographs from this test are presented in Appendix I. This test showed that the ring internal and external diameters increase with S/W. The ring thickness is essentially unaffected by variation in S/W for the data collected.

To ensure that the rings formed during these experiments were truly a function of particle diameter, and not caused by some unknown process varying from experiment-to-experiment, rings were obtained for the case where two particle diameters were present in the jet at the same time. This was done by slightly detuning the VOAG to produce a bimodal aerosol. The existence of a bimodal distribution of drops leaving the VOAG is easily confirmed by providing a slight horizontal air flow over the VOAG head which, when illuminated from the side, shows two separated jets instead of one when the system is appropriately detuned. Running the VOAG in this detuned condition produced two different particle diameters as shown in Fig. 4.5. The bottom images in Fig. 4.5 show the 1X images of the deposition pattern resulting from the bimodal aerosol, revealing two well defined rings, separated by a particle-free gap. The top images in this figure show a 10X view of the deposit, clearly showing that the larger diameter particles are located in the inner ring and the small particles in the outer ring, in agreement with the results presented in Figs. 4.3 and 4.4. Of note, some of the particles have soft, fluid-like edges and some appear to be in the process of merging, this is likely due to the hygroscopicity of the fluorescein particles discussed in Section 4.1. The possibility of particle merging prior to acquisition of the images presented in the images in Fig. 4.5 do not invalidate the conclusions herein, however, since this occurs once the particle has been deposited and therefore could not have influenced the particle's trajectory as it traveled from the nozzle to the slide.

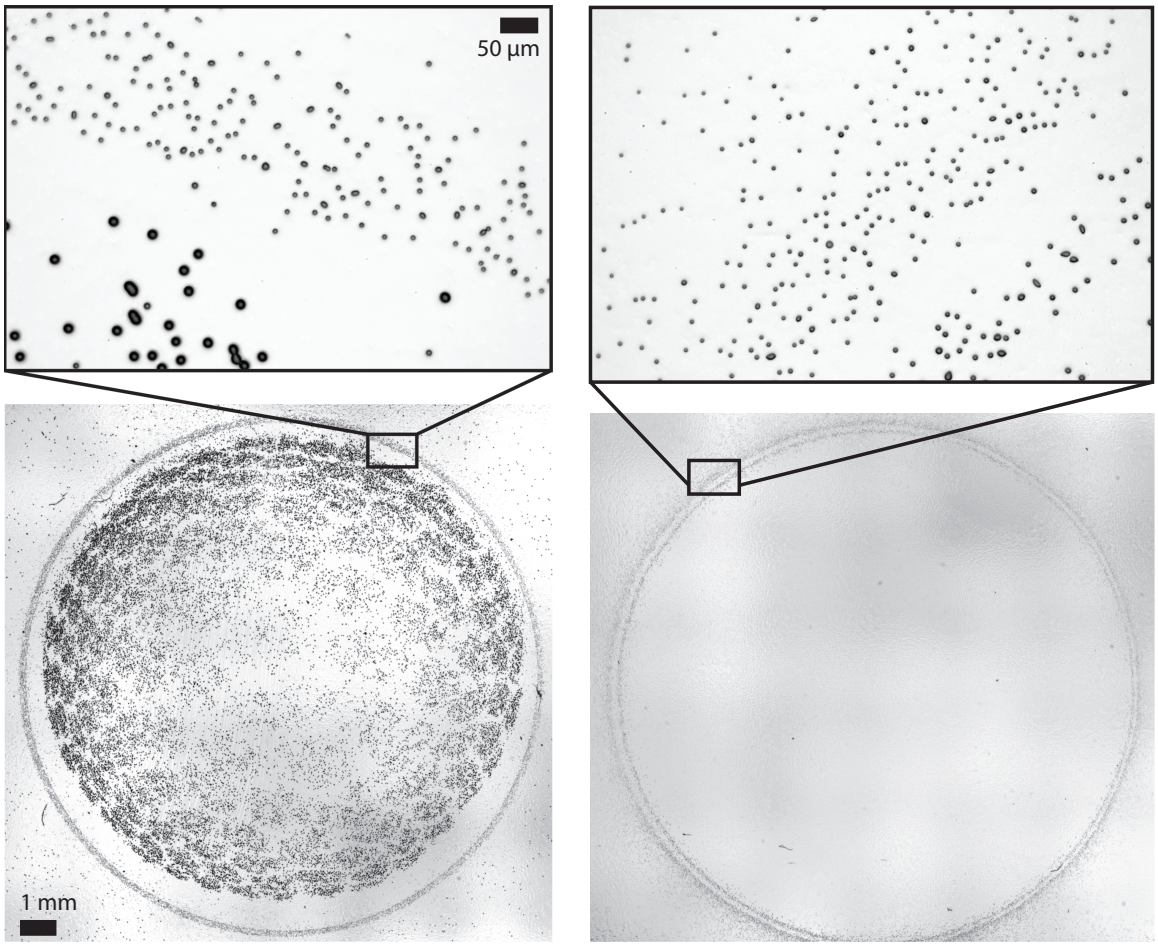

Figure 4.5: Deposition rings produced by bimodal particle distributions. The bottom images show two distinct deposition rings, separated by a thin particle-free region. The top images show magnified regions of the deposition rings, showing the size segregation of the deposited particles. The inner and outer deposition rings contain particles with d of (a) 12.98 μm and 7.9 μm and (b) 5.54 μm and 4.4 μm, respectively. This corresponds to Stk_W of (a) 0.40 and 0.14 and (b) 0.06 and 0.04, respectively.

4.3 Causes of impactor rings

The deposition patterns on impactor plates for traditional impactors have been previously investigated and described in the literature. These investigations have found that for typical operating conditions, the deposition pattern of a polydisperse aerosol is nominally a Gaussian distribution centered on the nozzle axis.[13,46,83,84,99] These studies did not, however, investigate the size distributions within the particle deposits. Studies of monodisperse particles have shown that there is some correlation between the spatial distribution of deposited particles and particle diameter for particles near d_{50}, with larger particles tending to deposit closer to the centerline of the jet, and smaller particles migrating outward.[46,99] However, this behavior appears to be the result of aerosol focusing in the impactor nozzle. Aerosol focusing will preferentially concentrate selected diameter particles to the centerline of the flow, the selected particle size being a function of the flow conditions and the nozzle geometry.[22,25,26,81,82,114] Burwash *et al.*[14] found a similar deposition pattern with fixed particle sizes for high Reynolds number jets, and that the relationship between the deposition location was correlated with S/W. However, it should be noted that none of the above studies reveal a clear separation between particle deposition locations based on size, showing only a gradual shift in the radial extent of a Gaussian pattern.

In addition to the deposition patterns discussed above, secondary deposits, or "halos", have been occasionally observed ringing the main deposit on an impactor stage.[13,68,83,84] The particles in these "halo" deposits have diameters smaller than d_{50} for the impaction stage, suggesting some relationship between deposition location and particle diameter, at least for particles smaller than d_{50}. However, no other studies have explored whether and to what extent particles were geometrically segregated in these halos according to their size. Several mechanisms have been proposed to explain the formation of these "halo" deposits, including gravitational settling, Magnus lift, Saffman lift, and particle resuspension. However no studies have examined the role of these proposed mechanisms in the formation of "halo" deposits on a diameter-resolved basis. All of these deposition patterns appear to be significantly different from those presented in the present work, as the observed rings, such as those presented in Figs. 4.3 and 4.5, are very well defined with minimal blurring around the edges compared with those described in the literature above. Hence, the results presented herein showing a clear ring pattern for a monodisperse aerosol, where the ring diameter is clearly related to the particle diameter, is a new result.

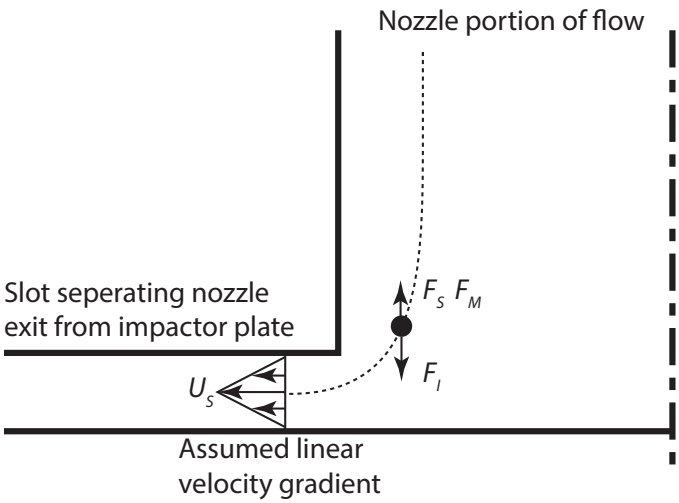

Figure 4.6: Free-body diagram of forces acting on the particle in a curvilinear path transitioning from the flow through the nozzle to flow through the slot gap between the nozzle exterior and the impactor slide. Also shown is the assumed velocity profile in the slot for the purpose of this order of magnitude analysis.

It is worth noting that an instrument does exist which uses deposition location to size particles. This instrument is the inertial spectrometer, which relates aerosol diameter to the location along a curved path where the aerosol is deposited.[11,75] Obviously the flow conditions in this instrument are significantly different from those which exist in the impactor described in the present work.

The excellent correlation of the ring diameters with Stk_W shown in Fig. 4.4 suggests that the observed ring deposition patterns are governed by particle inertia. To help confirm this, an order of magnitude analysis is now presented to determine the degree of influence that other processes, such as Saffman lift, Magnus lift, and diffusion due to Brownian motion, as well as inertia, would have on the deposition patterns. A free body diagram is presented in Fig. 4.6 showing the forces considered as well as the assumed velocity profile within the slot separating the exterior of the nozzle (the region "F" shown in Fig. 4.2) and the impactor plate. All the forces considered are assumed to occur within the indicated slot.

The particle inertia was estimated using the acceleration required to stop a particle traveling at velocity U over a duration, τ; where τ is the relaxation time of the particle given by:

$$\tau = \frac{W \cdot Stk}{2U} \tag{4.3}$$

The particle inertial force, F_I, was then estimated as:

$$F_I = \frac{\rho \pi d^3 U}{6\tau} \tag{4.4}$$

The Saffman lift force, F_S, on a particle traveling through a velocity gradient, was estimated according to the work of Saffman[87,88] as:

$$F_S = 1.615 \rho_f d^2 U_S \sqrt{\nu \frac{dU_s}{dy}} \tag{4.5}$$

where ρ_f is the fluid density, ν is the kinematic viscosity, and U_S is the velocity through the slot. As indicated in Fig. 4.6 it was assumed that the velocity gradient in the slot was linear, and that there were no compressibility effects.

The lift due to the rotation of a sphere, the Magnus effect, F_M, was obtained using the work of Rubinow and Keller:[86]

$$F_M = \frac{\pi}{8} d^3 \omega \rho_f U_S \tag{4.6}$$

where ω is the angular velocity of the rotating particle. The rotation of the particle was estimated as a solid body rotation driven by the velocity difference across the particle.

Values of F_I, F_S, and F_M are presented in Table 4.1 for a range of conditions and particle diameters investigated in this work. These numbers show that inertia is the dominant force acting on the particles, except perhaps at large Stk_W where F_I is indeed larger than F_S, but only double its magnitude. Further investigation is needed, but it seems likely that inertia is the governing factor in the formation of these rings.

Finally, it is now demonstrated that the amount of "blurring" in the rings caused by Brownian motion of the particles is small compared to the measured ring dimensions. The particle drift, δ_B, due to Brownian motion was estimated as:[43]

$$\delta_B = \sqrt{2\mathcal{D}t} \tag{4.7}$$

where t is the transit time of a particle on the centerline to completely pass through the curved portion of the flow between the nozzle and the impaction plate, and $\mathcal{D}$ is the particle diffusivity

Stk_W	d (μm)	U (m/s)	F_I (N)	F_S (N)	F_M (N)	δ_B (mm)
0.12	10	1.5	2.6×10^{-9}	1.4×10^{-9}	9.7×10^{-11}	1.8×10^{-4}
1.2×10^{-3}	1	1.5	2.6×10^{-10}	1.4×10^{-11}	9.7×10^{-14}	6.1×10^{-4}

Table 4.1: Results of order of magnitude analysis of the influence that several mechanisms have on particles traveling through the gap between the nozzle and microscope slide for the conditions of the experiments presented herein.

defined as:[43]

$$\mathcal{D} = \frac{kTC_c}{3\pi\mu d} \tag{4.8}$$

where k is the Boltzmann constant, C_c is the Cunningham slip correction, and T is the temperature. As Table 4.1 shows, the particles will move on the order of a micron due to diffusion, which is orders of magnitude smaller than the millimeter scale thickness of the rings presented here, and indicates that diffusion should be negligible in the formation of the observed rings.

Based on the results of this analysis confirming inertia to be the dominant mechanism contributing to the observed ring deposits, a rough model and method for using ring deposits for aerosol sizing was developed and is presented in Appendix J.

4.4 Impactor ring findings

Experiments were conducted to measure the deposition patterns resulting from an impactor with $S/W = 0.047$. The resulting deposition patterns were in the form of rings whose inner and outer diameter were correlated to Stk_W. These rings appear to be distinct from the impactor deposition patterns described by previous investigators.[13,14,46,68,83,84,99] An order of magnitude analysis has shown that inertia is dominant for the particle sizes investigated and the most likely cause of the ring shaped depositions observed. As the ring geometry is so well correlated with Stk_W, it may be possible to use the spatial location of deposition to help determine inter-stage particle size distributions if the results presented herein can be applied in a traditional impactor cascade.

Chapter 5

Conclusions

A study of the existing published data in the inertial regime was performed and compared against the Slinn and Calvert inertial models. The Calvert model was found to better describe the existing data, however both models had large residuals near the transition away from inertially dominant scavenging. These residuals were found to be well correlated with an inertial term, Stk_r, in the case of the Slinn model. A correction term was added to the model, and both the Calvert and modified Slinn model were then shown to have residuals correlated to Re. Correction terms were developed for Re for both models, and the resulting modified models were shown to be in good agreement with the published data.

It was hypothesized that wakes, drop oscillations and/or drop shape contributed to the Re dependent mechanism. To test this hypothesis an acoustically levitated drop was used to investigate these effects. This investigation showed that the wake did not play any significant role in scavenging. However the results did show the importance of drop shape in scavenging. Drop oscillations had no measurable impact on scavenging. Based on this finding a model was developed which allows for the extrapolation of scavenging model predictions, which assume spherical drops, to predict scavenging for arbitrarily deformed drops, such as those seen in rain; and vice versa. Additionally the use of a non-evaporating drop in these experiments highlighted the significance of diffusiophoresis in scavenging of water drops. This mechanism is a function of Re and is likely the cause of the strong model correlations to Re observed in the study of published data.

Finally during the course of these experiments it was observed that small S/W impactors produced discrete ring shaped deposition patterns. Experiments were performed which showed that

the diameter and thickness of these deposition patterns were strongly dependent on the particle size, and could be manipulated by changing the impactor geometry. A scaling analysis showed that pure inertia is the dominant force acting on particles in this region of the impactor. This finding opens the possibility of developing a novel aerosol sizing method with better resolution than the traditional impactor cascade.

Appendices

Appendix A Scavenging models

Inertial scavenging: E_I occurs when a particle approaches a drop, and due to the curvature of the streamline it is traveling along and the particle inertia, the particle deviates from its streamline and impacts the drop, removing the particle from the flow.

There are two models for E_I that are commonly found in the literature, the first is the model due to Slinn:[104]

$$E_{I,1} = E_S = \left(\frac{\rho}{\rho_w}\right)^{1/2} \frac{Stk - Stk_*}{Stk - Stk_* + 2/3} \tag{A.1}$$

where ρ_w is the density of water. Inertial impaction, as described in Eq. (A.1) is on only applied when Stk is greater than the critical stokes number, Stk_*, which is:

$$Stk_* = \frac{1.2 + \frac{1}{12}\ln(1+Re)}{1+\ln(1+Re)} \tag{A.2}$$

Where Re is the radius based drop Reynolds number, $Re = \rho_a U D/2\mu$.

The second model for E_I is due to Calvert:[16,17]

$$E_{I,2} = E_C = \left(\frac{Stk}{Stk + 0.35}\right)^2 \tag{A.3}$$

which has no Stk_* limitation.

Interception scavenging: E_i occurs when a particle is transported over a drop and the particle center of mass does not deviate from its streamline, which does not intersect the drop surface. However as the particle has a finite volume, any streamlines within the particle radius of the drop surface will cause the particle graze the drop, and be removed from the flow. Interception scavenging can be modeled from the work of Slinn:[104]

$$E_i = 4\frac{d}{D}\left[\frac{\mu}{\mu_d}\left(1 + 2Re^{1/2}\frac{d}{D}\right)\right] \tag{A.4}$$

where μ_d is the viscosity of the drop.

Diffusion scavenging: E_D occurs when a particle is small enough that as it interacts with the air molecules in its path the particle is deflected due to Brownian motion. Because of the "random walk"

of the particle centered around its streamline, it can be deflected into the drop surface, removing the particle from the flow. Diffusion scavenging can be modeled from the work of Slinn:[104]

$$E_D = \frac{4}{ReSc}\left(1 + 0.4Re^{1/2}Sc^{1/3} + 0.16Re^{1/2}Sc^{1/2}\right) \tag{A.5}$$

where Sc is the Schmidt number, $Sc = \mu/\rho_a\mathcal{D}$ where $\mathcal{D}$ is the particle diffusion coefficient:

$$\mathcal{D} = \frac{k_b T C_c}{3\pi\mu d} \tag{A.6}$$

where k_b is the Boltzmann constant and T is the air temperature.

Thermophoretic scavenging: E_{tph} occurs when a particle moves through a temperature gradient, and the presence of the gradient exerts a force on the particle pushing it in the direction of the heat flow. For an evaporating drop there will be a sufficient temperature gradient near the drop surface due to the evaporative cooling of the drop surface. Thermophoretic scavenging can be obtained from the model due to Waldman, as reported by Davenport and Peters:[28]

$$E_{tph} = \frac{4\alpha_{th}\left(2 + 0.6Re^{1/2}Pr^{1/3}\right)(T - T_d)}{UD} \tag{A.7}$$

where T_d is the drop surface temperature, Pr is the Prandtl number of air, and α_{th} is given by:

$$\alpha_{th} = \frac{4C_c\left(k_a + \frac{5\lambda}{D}k_p\right)k_a}{5P\left(1 + \frac{6\lambda}{D}\right)\left(2k_a + k_p + \frac{10\lambda}{D}k_p\right)} \tag{A.8}$$

where k_a and k_p are the air and particle thermal conductivity respectively and P is the air pressure.

Diffusiophoretic scavenging: E_{dph} occurs when a particle passes through a concentration gradient, such as the vapor concentration gradient near the surface of an evaporating drop. The Stefan flow of the vapor phase will exert a force on the particle in the direction of flow of the heaviest molecule in the gradient. Diffusiophoretic scavenging can be found from the model due to Waldman and Schmidt as reported by Davenport and Peters:[28]

$$E_{dph} = \frac{4\beta_{dph}\left(2 + 0.6Re^{1/2}Sc_d^{1/3}\right)\left(\frac{P_d^0}{T_d} - \frac{P_a^0\Phi}{T}\right)}{UD} \tag{A.9}$$

where Sc_d is the Schmidt number of the drop vapor diffusing into air, P_d^0 and P_a^0 are the vapor

pressure of the drop fluid at the drop surface and air temperature respectively, Φ is the relative humidity of the air, and β_{dph} is given by:

$$\beta_{dph} = \frac{T\mathcal{D}_d}{P}\left(\frac{M_d}{M_a}\right)^{1/2} \tag{A.10}$$

where $\mathcal{D}_d$ is the diffusivity of the drop vapor into air, M_d is the molecular weight of the drop fluid, and M_a is the molecular weight of the air.

Net scavenging: The total scavenging of a drop is the sum of the scavenging contributions due to each mechanism. Using the Slinn model for inertial scavenging for the inertial term, the model for net scavenging is given as:

$$\begin{aligned} E = & \left(\frac{\rho}{\rho_w}\right)^{1/2}\frac{Stk - Stk_*}{Stk - Stk_* + 2/3} + 4\frac{d}{D}\left[\frac{\mu}{\mu_d}\left(1 + 2Re^{1/2}\frac{d}{D}\right)\right] \\ & + \frac{4}{ReSc}\left(1 + 0.4Re^{1/2}Sc^{1/3} + 0.16Re^{1/2}Sc^{1/2}\right) \\ & + \frac{4\frac{4C_c\left(k_a + \frac{5\lambda}{D}k_p\right)k_a}{5P\left(1+\frac{6\lambda}{D}\right)\left(2k_a + k_p + \frac{10\lambda}{D}k_p\right)}\left(2 + 0.6Re^{1/2}Pr^{1/3}\right)(T - T_d)}{UD} \\ & + \frac{4\frac{T\mathcal{D}_d}{P}\left(\frac{M_d}{M_a}\right)^{1/2}\left(2 + 0.6Re^{1/2}Sc_d^{1/3}\right)\left(\frac{P_d^0}{T_d} - \frac{P_a^0\Phi}{T}\right)}{UD} \end{aligned} \tag{A.11}$$

Appendix B Acoustic levitation apparatus and control

The acoustic standing wave field supporting the drop was created using an ultrasonic transducer, a function generator (Agilent 33220A), an amplifier (Krohn-Hite 7500), and custom control software. The transducer, shown in Fig. B.1, consisted of two piezoelectric disks with a copper plate between and an aluminum emitter horn and backmass, detailed drawing of which are shown in Figs. B.2 and B.3 respectively. The copper plate acts as the positive electrode for the piezoelectric disks, while the aluminum components act as ground. When a sine wave is applied to the transducer the piezoelectric ceramic will vibrate at the frequency of the applied signal. The transducer components are bolted together with sufficient clamping force to ensure that this vibration is transmitted through the emitter horn and produces a sound wave at the interface of the emitter horn and the air. According to Trihn this should be approximately 350 in-lbs, however during assembly it was not possible to verify this. Instead the transducer was tightened until bridging the aluminum and copper would produce a green spark due to the voltage produced by compressing the piezoelectric ceramic.

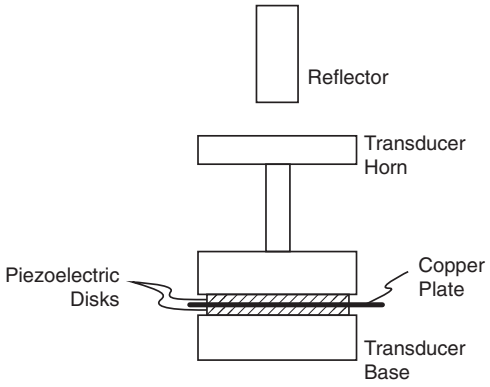

Figure B.1: Schematic of the assembled ultrasonic transducer and reflector, based on the general design of Trinh[110]

To drive the transducer a function generator output a sine wave at approximately 30 kHz with an amplitude of 300-900 mV. The function generator output was run through an amplifier with a gain of 100x to produce a signal of 30-90 V. The resulting high amplitude signal was applied to the ultrasonic transducer. The transducer will only produce a sufficiently strong standing wave when it is excited at resonance. The piezoelectric ceramic is manufactured to have a given resonant frequency, however due to manufacturing tolerances and the coupling between the piezoelectrics

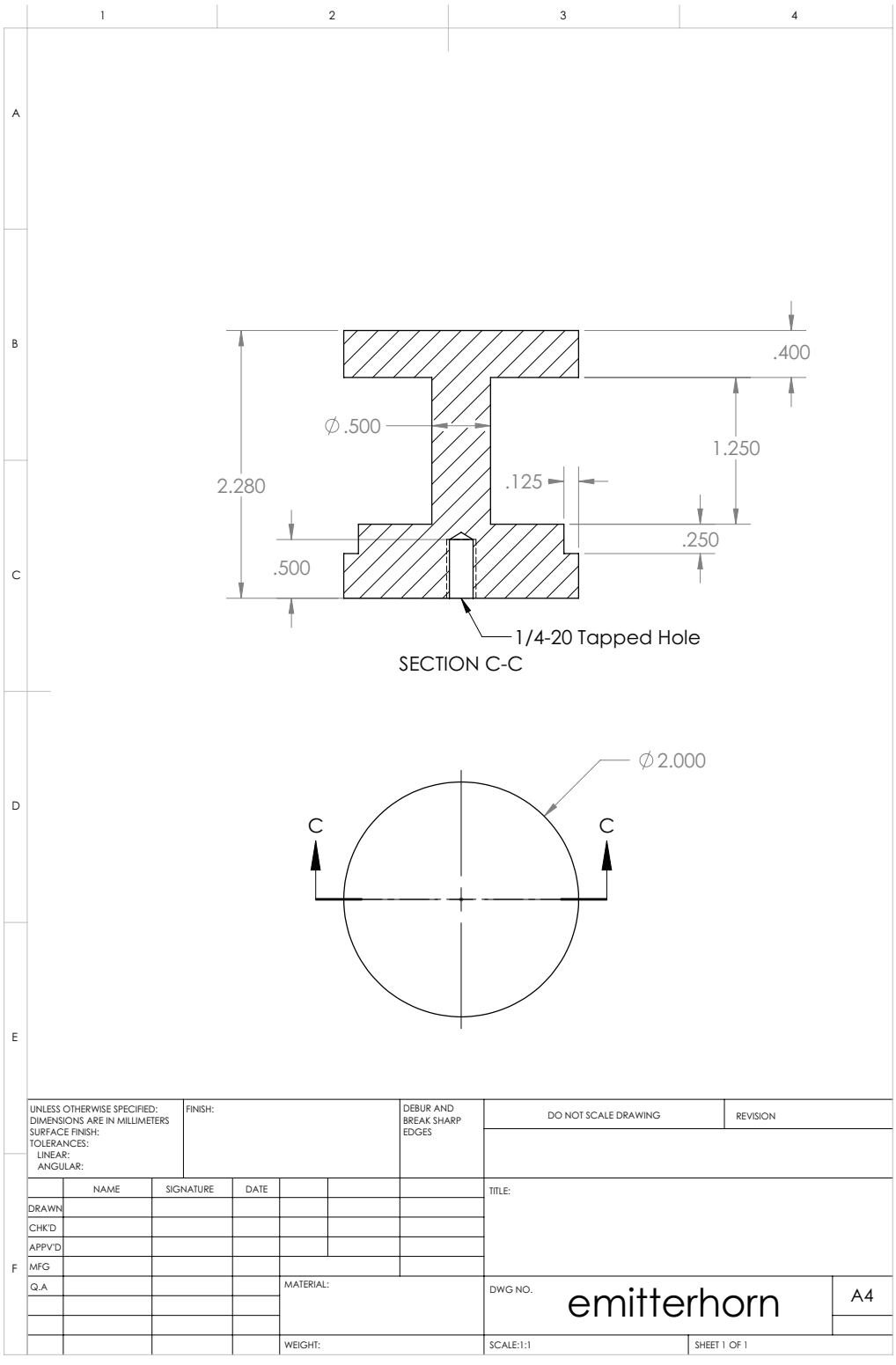

Figure B.2: Machine drawing of the aluminum emitter horn used in the transducer.

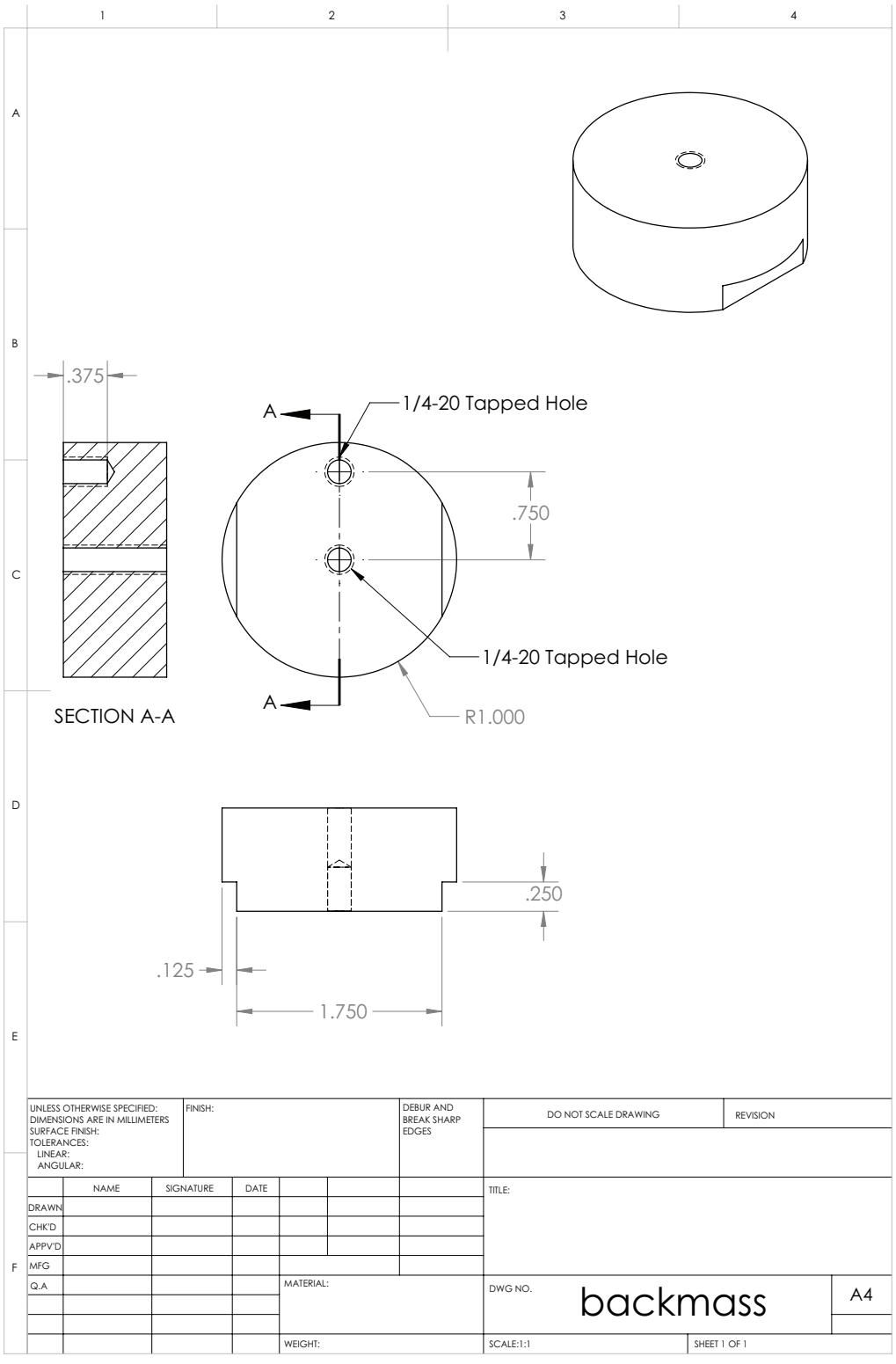

Figure B.3: Machine drawing of the aluminum backmass used in the transducer.

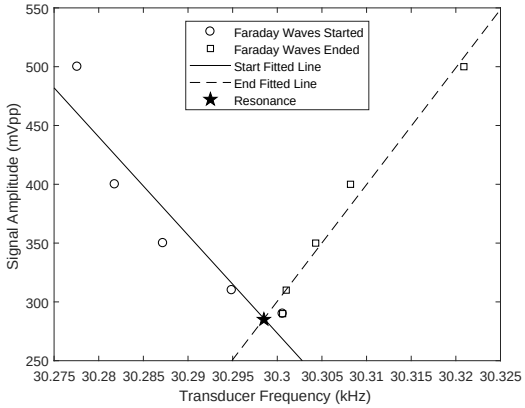

Figure B.4: Plot showing the first and last frequency observed to produce Faraday waves in a sessile drop on the transducer emitter horn at various power levels. The intersection of these two sets gives the resonant frequency of the transducer at approximately 30298.5 Hz

and the other transducer components, when assembled into the transducer this frequency was not found to be an sufficient prediction of the transducer resonant frequency. To determine the resonant frequency of the transducer a small volume of water was placed on the emitter horn. This water drop was back lit and imaged with a real time image display. At a given voltage a frequency sweep was performed. When the transducer was near resonance Faraday waves were visible on the drop. The range of frequencies which produced Faraday waves was recorded, and then the voltage was reduced and the frequency sweep repeated. As the applied voltage reduced the range of frequencies which produced Faraday waves decreased. After performing this measurement for several voltages linear trend lines were found for the onset and cessation of Faraday waves, and the intersection point between these two fits was taken to be the resonant frequency for the transducer assembly. A plot of the tuning data of the transducer used is shown in Fig. B.4.

Nominally an acoustic standing wave field will be produced when a reflector is placed an integer number of half wavelengths from the emitter horn. To tune the gap separation between the emitter horn and the reflector a small volume of water was placed on the emitter horn and the transducer was energized. At larger applied voltages the Faraday waves are energetic enough to emit satellite droplets from the water surface, which are ejected into the acoustic field. The reflector gap spacing was adjusted until these aerosolized water droplets began to accumulate in an a node of the acoustic field, and form a small levitating droplet. The gap spacing was further refined by injecting a droplet into the identified node and adjusting the transducer gap while monitoring the

drop shape. For a given applied voltage the gap was adjusted to maximize the deformation of the drop, indicating that the reflector was optimally placed to produce a stronger standing wave field, which could support the drop during the experiments.

Unfortunately, the resonant frequency of the transducer is not constant. It was observed that as the transducer operated the resonance frequency drifted, and a drift of approximately 10 Hz would be sufficient to no longer produce a standing wave strong enough to levitate a droplet. It is hypothesized, but not confirmed, that this drift is due to the heat generated by the vibrating transducer causing a shift in the transducer resonance frequency. To keep the transducer tuned during a scavenging experiment the following technique was developed. The applied voltage, V, and current, I, were measured with an oscilloscope and plotted against each other in real time. When the transducer was able to levitate drops the V vs I plot formed a diagonal line, however as the frequency drifted away from resonance the V vs I plot opened up to form an oval. When this plot collapsed to a diagonal line this corresponded to V and I being in phase with each other. From AC power theory, the power, P, in an AC circuit can be found as:

$$P = IV\cos(\theta) \tag{B.1}$$

where θ is the phase shift between I and V. Therefore the transducer power is maximized when θ is zero.

This allowed for an easy, visual method for tuning the transducer to enable drop levitation, however constantly updating the frequency was not realistic for performing a scavenging experiment. Therefore a controller was developed to automatically keep the transducer operating at peak power throughout the experiment. For this task LabView was used to control the signal applied to the transducer. An overview of the front panel and block diagram for the controller is presented in Figs. B.5 and B.6. The front panel gives real time output of the voltage and current measurements, as well as the measured phase between them. Additionally the front panel allows for the user to set the initialization and sampling parameters, target phase, the voltage, amplitude modulation frequency, the amplitude modulation magnitude, the log file name, and some imaging parameters. The voltage and current measurements were performed using a Measurement Computing high speed USB DAQ capable of sampling 2 channels simultaneously at 10 MHz each. This DAQ can only measure voltage however, so to measure the current the voltage drop across a 2.474 Ω resistor was measured and

converted to current with Ohm's law. The DAQ was only able to measure a maximum of 10 V, therefore in order to measure the voltage drop across the transducer a voltage divider was used to reduce the measured voltage drop across the transducer by 1/5. A schematic view of the voltage measurements is shown in Fig. B.7. During operation the DAQ measured 1000 data points at 10 MHz, this gives approximately 300 measurements per signal period for the frequency applied to the transducer and fully resolves approximately 3 waveforms. A sine wave was fit to each signal, and the phase difference was then calculated from the two fits. This is the "Measure and Display" portion of the block diagram in Fig. B.6.

A very rudimentary controller was then implemented to adjust frequency in order to attain a user specified θ target. First the decision to increment or decrement the frequency was made by comparing the θ measurement with the previous loop's value, and if θ was getting nearer the target then the frequency change would occur in the same direction as the previous loop, otherwise the direction would reverse. Next the magnitude of the frequency change was determined, if θ was more than one degree off from the target the frequency would only be changed by one Hz, if θ was off by a smaller amount then a quadratic smoothing function was used to calculate the change in frequency. If the signal was being amplitude modulated no frequency adjustment was made due to instability that would occur resulting from attempting to get good measurements of the modulated signal, any frequency drift during amplitude modulating runs was deemed acceptable. This is the "Tuning Control" portion of the block diagram in Fig. B.6.

The function generator supplying the signal to the transducer was then adjusted to output the new frequency. The Agilent function generator can be controlled by sending the driver a correctly formatted text string. The new frequency, as well as the current user input voltage, amplitude modulation frequency, and amplitude modulation depth were written to a string and sent to the Agilent function generator. This is shown in the "Transducer Signal Output" portion of the block diagram in Fig. B.6. A log of the applied voltages, frequencies, amplitude frequencies, and amplitude depths along with the measured voltage, current, power, and phase were written to a log file. This is shown in the "Log Output" portion of the block diagram shown in Fig. B.6. This process was applied approximately four times per second, giving a relatively stable acoustic field for the scavenging experiments, and a detailed log of the transducer operation.

As the Cooke Sensicam used to image the drop could not achieve a high enough frame rate to fully resolve the drop oscillations, aliasing was controlled to resolve the drop oscillations. This

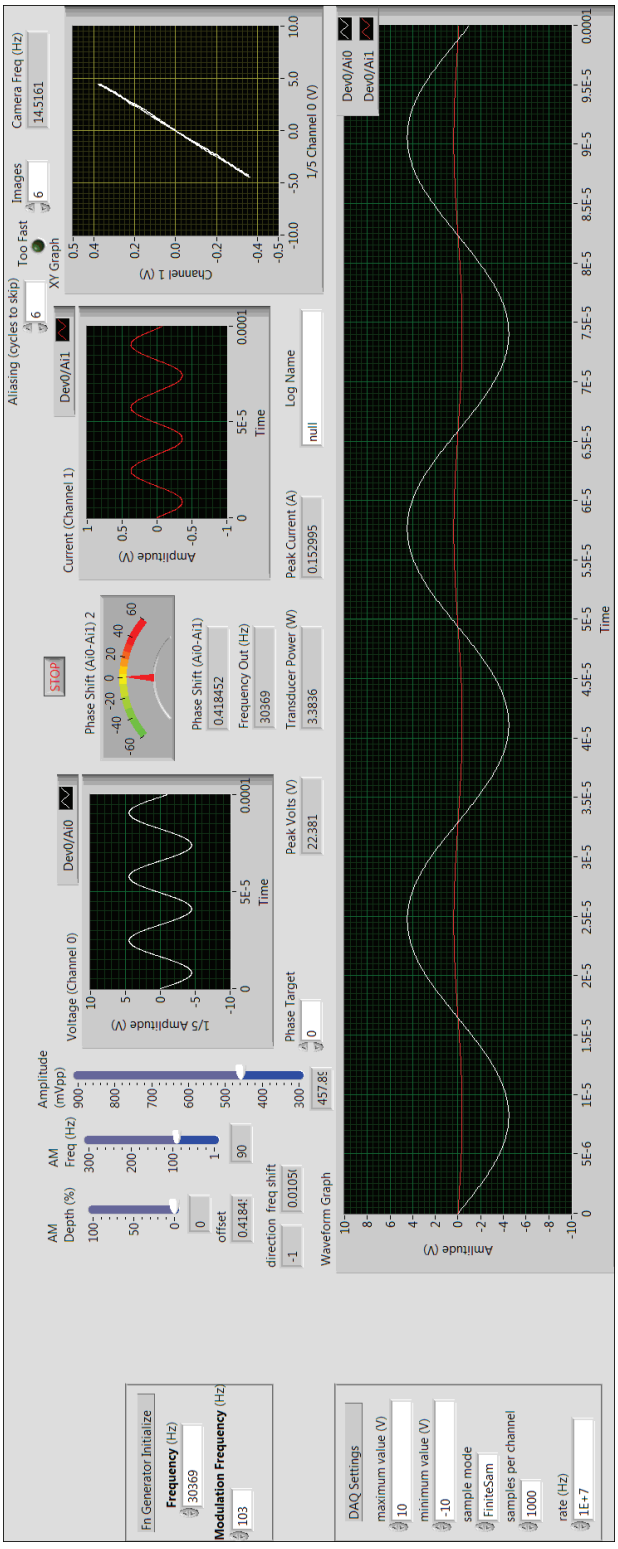

Figure B.5: The LabView front panel for the transducer controller.

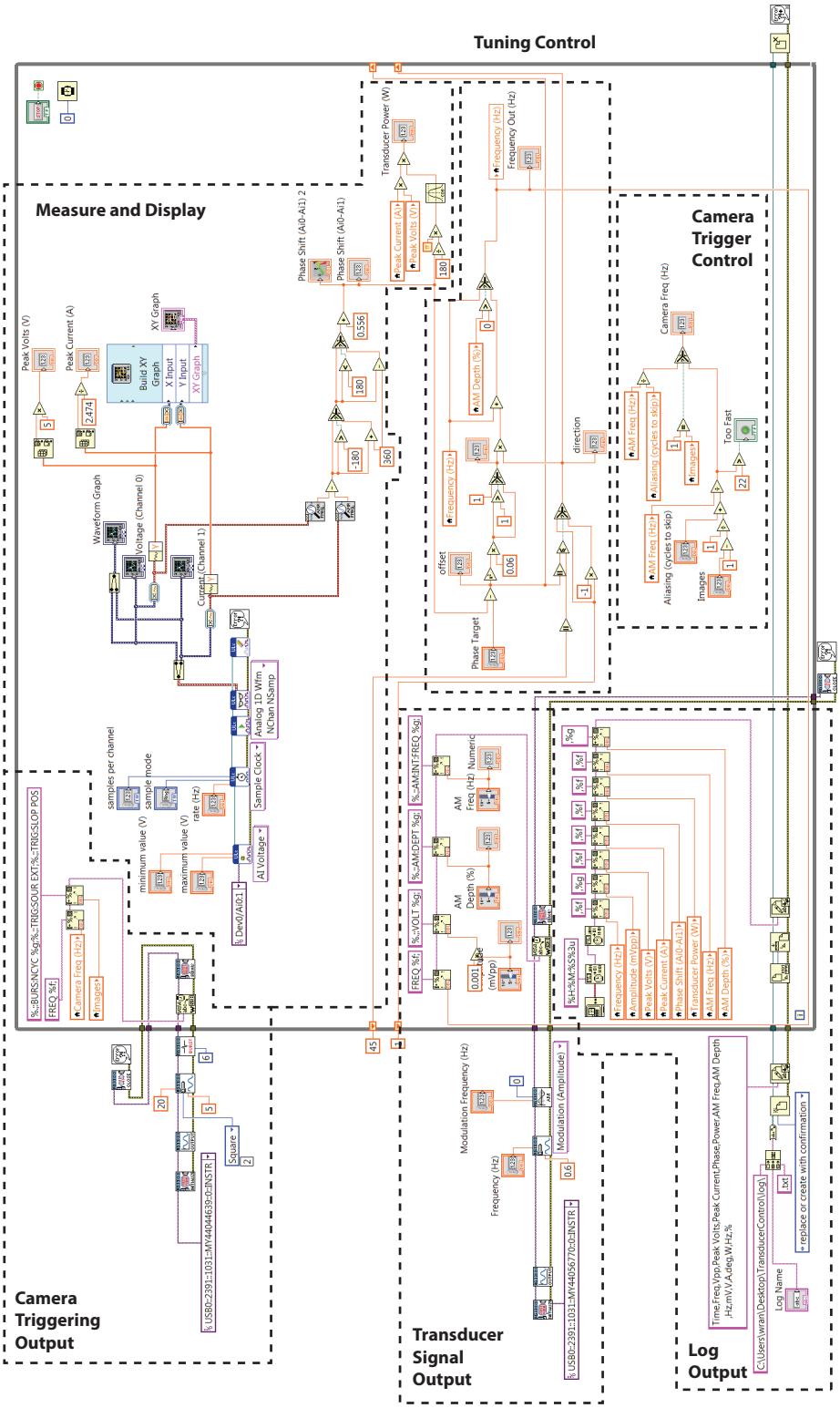

Figure B.6: The LabView block diagram used control the transducer during the scavenging experiments. The function of the block diagram is explained in detail in the text.

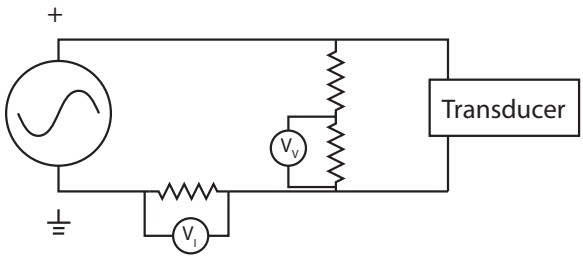

Figure B.7: Schematic showing where the voltage and current measurements where taken for controlling the transducer. The voltage from V_I was converted to I using Ohm's law.

.

was achieved by taking advantage of the fact that if amplitude modulation was to be used to excite a levitated drop, the drop would oscillate at the frequency of the acoustic field modulation. It was therefore possible to implement camera control into the transducer control in LabView. First, the sync output signal from the Agilent function generator was connected to the trigger input on a second Agilent function generator. The sync signal is a clock signal which is a square wave at the frequency of the main output of the function generator, this allows for multiple function generators to operate synchronously. Upon receiving a trigger from the first function generator, the second function generator was configured to output a square wave burst. This signal was input to the trigger of the Sensicam to control the timing of the drop imaging and therefore allowed for control over the aliasing of the drop and enabled the camera to capture the maximum and minimum deformation experienced by the drop. The user inputs the number of images desired to resolved the aliased drop oscillation, n_I, and the number of drop oscillations that should be skipped between images, n_S, and the sample frequency, f_s, is calculated based on the modulation frequency, f_{am}, as:

$$f_s = \frac{f_{am}}{(n_I - 1)^{-1} + n_S} \tag{B.2}$$

A visual representation of this is shown in Fig. B.8, which shows how the camera is controlled based on the amplitude modulation frequency of the drop. The calculation of the camera sample frequency is shown in the "Camera Trigger Control" portion of the block diagram in Fig. B.6, the result of which is passed to the second Agilent function generator using a formatted string, similar to the previous function generator control, as shown in the "Camera Trigger Output" portion of the block diagram in Fig. B.6.

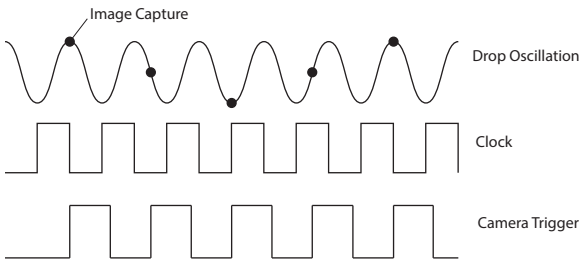

Figure B.8: Diagram showing how the amplitude modulation of the drop is used to control the timing for imaging the oscillating drop. With this control the aliasing of the drop is manipulated to fully resolve a full period of the drop oscillation.

Appendix C Acoustic streaming impact

Acoustic streaming is a phenomena where an object within an acoustic field will generate vortexes in the flow around the object, such as a levitated drop. This occurs due to the scattering of the acoustic waves, which are nominally planar waves, interacting with the object in the field. At the interface between the object and the acoustic wave, which is irrational, will be forced to change direction due to the no penetration condition at the interface. This induces rotation within the acoustic boundary layer near the object's surface. The rotation within the acoustic boundary layer is viciously coupled with the general flow in the field and produces vortexes in around the object. To measure the extent which accoustic streaming may be induced near the drop in the scavenging experiments a flow visualization experiment was performed to estimate the flow field around a the drop with streak imaging velocimetry. In this experiment a 0.5 W argon-ion laser was expanded into a sheet with a series of cylindrical lenses. This laser sheet was aligned with the axis of the jet. The tracer particles for this experiment was talc powder. Talc was used instead of fog as was used previously because the fog generator produced too large a concentration of droplets which masked any structure in the flow, while the talc concentration was such that individual streak lines could be identified. A container filled with talc was placed upstream of the nozzle, and the talc was aerosolized via agitation with a PC case fan mounted in the container. The concentration of the aerosolized talc could be roughly controlled by varying the velocity of the fan, and was adjusted until individual streak lines were visible in a live image preview.

This talc laden jet was blown over a glass sphere mounted within the acoustic field and the resulting flow was imaged using a Cooke Sensicam at 20 frames per second. This sample rate is low enough that each image is independent, and all talc particles in a given frame will be out of the imaged region before the subsequent image is taken. A sample image of the talc tracer particle streaks is shown in Fig. C.1. To determine the influence of streaming on the flow first images were taken with the acoustic field deactivated. To identify the streaks in the image, first the glass sphere was masked out in the image, then the vertical image gradient was calculated. This was done to reduce thermal noise from the image. Only the positive gradients were considered to avoid double counting each streak, then the image was converted to binary using a threshold value of 2 standard deviations above the the mean gradient value. This process produced an image of the isolated streaks in a format which made calculating flow information possible. A sample processed streak

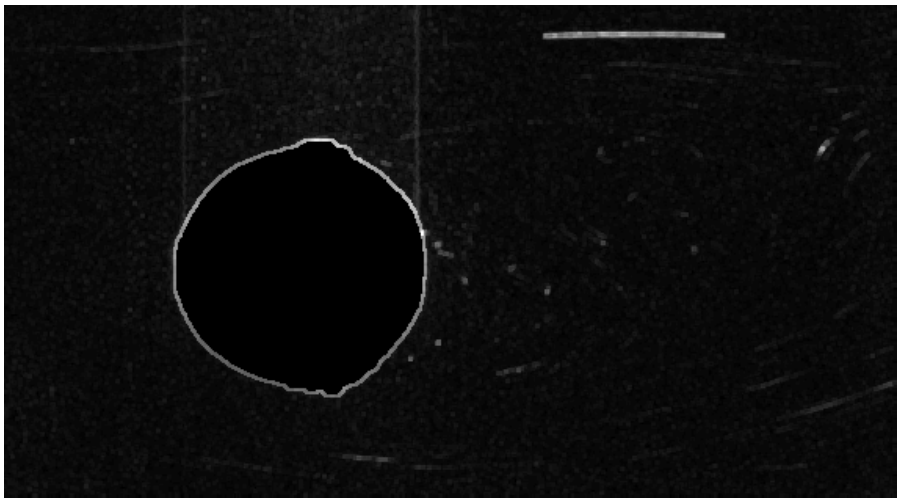

Figure C.1: Photograph of talc tracer particles illuminated by a 0.5 W laser sheet in flow around a glass sphere showing a vortex behind the sphere. The glass sphere has been masked out and flow is from the left to the right.

image is shown in Fig. C.2. The magnitude and direction of each streak was then calculated by identifying the endpoints of each streak and these values were stored at the centroid of each streak. This process was repeated for 1000 images and the average magnitude and direction of the streaks was determined. A sample flow field is shown in Fig. C.3.

This process was repeated with the acoustic field enabled, and the difference between the resulting velocity field was determined. A sample plot showing the difference in the magnitude and direction of the velocity field near the drop in the presence and absence of the acoustic field is shown in Fig. C.4. This figure shows the percent difference between the undisturbed flow, which approximates what a drop falling at its terminal velocity would experience, and that disturbed by the acoustic field. As this figure shows, there is some deviation from the undisturbed flow, however this is limited to near the bounds of the recirculating wake behind the drop. The average differences

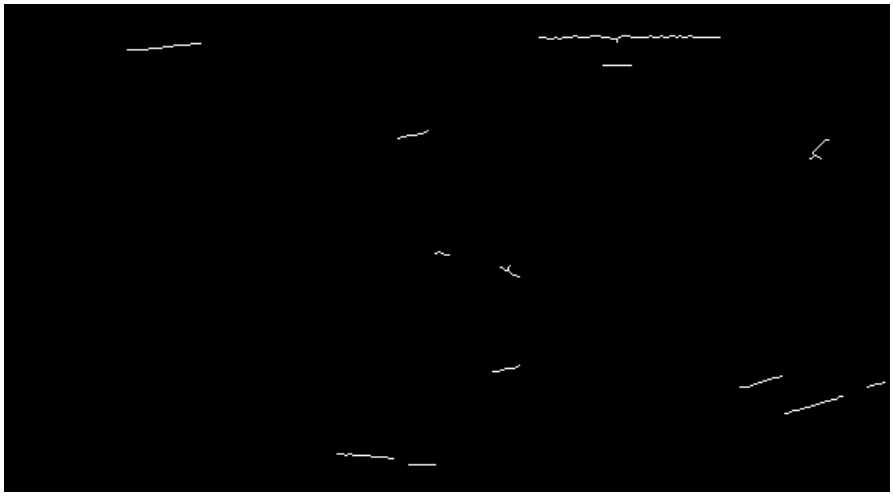

Figure C.2: Image showing the isolated streaks from talc tracer particles after the algorithm described in the text has been applied. Flow is from the left to the right.

in velocity field magnitude and direction at various acoustic field strengths and Reynolds numbers are shown in plots in Fig. C.5. As this figure shows, the magnitude of the velocity field around the drop, and in the sphere wake has some deviation compared to that observed without the field enabled, and after $Re \sim 200$ tends to increase with increasing Re. The large deviation at low Re is likely due to the presence of acoustic streaming near the sphere interface, and the large deviations at higher Re are likely due to an irregular number of vortex shedding periods captured in each sample. Additionally, the direction of the flow generally has small deviations with and without the field enables, and this difference decreases with increasing Re. Therefore based on these results it can be concluded that in the Re range of the experiments herein any acoustic streaming will have negligible impact on the scavenging of a drop suspended in the field.

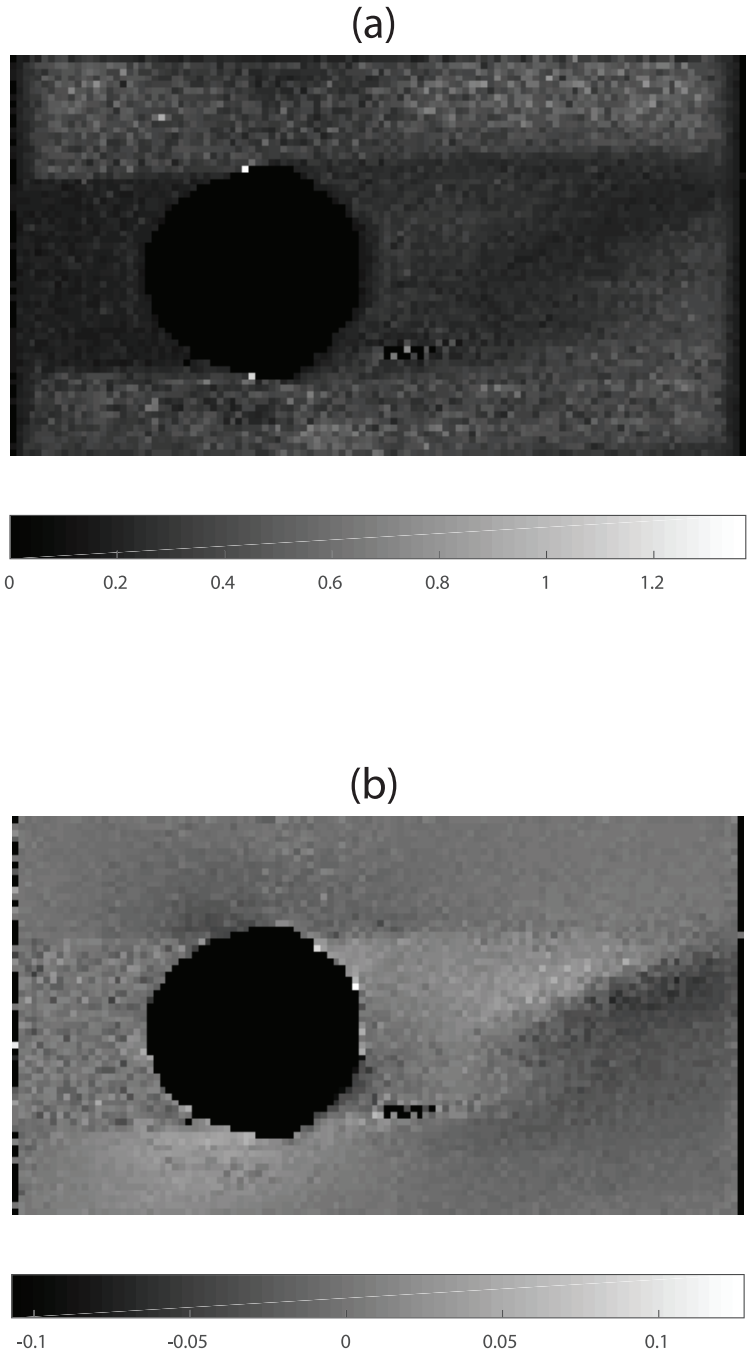

Figure C.3: Processed images using streak image velocimetry for a sphere at $Re = 178$, showing the (a) magnitude of the velocity field in m/s and (b) the direction of the velocity field in Rads. Flow is from the left to the right.

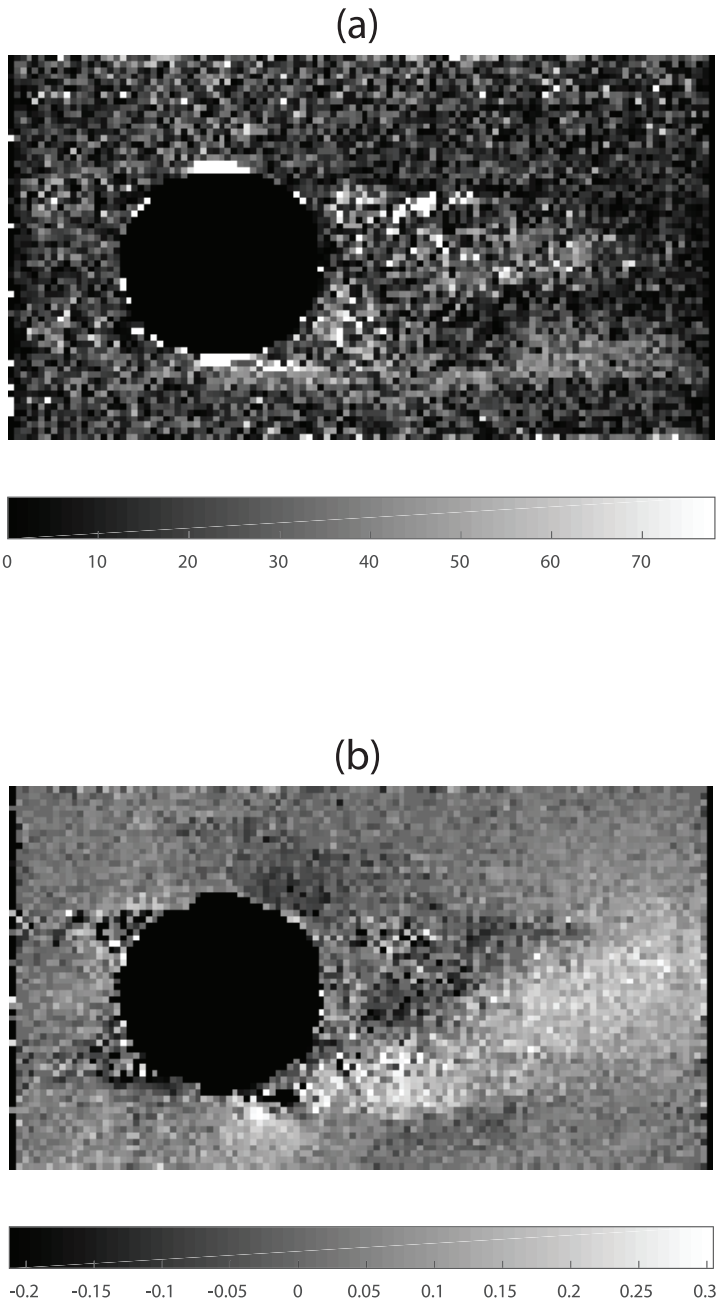

Figure C.4: Images showing the percent difference between the undisturbed and ultrasonically excited velocity field around a sphere for the velocity (a) magnitude and (b) direction at $Re = 178$.

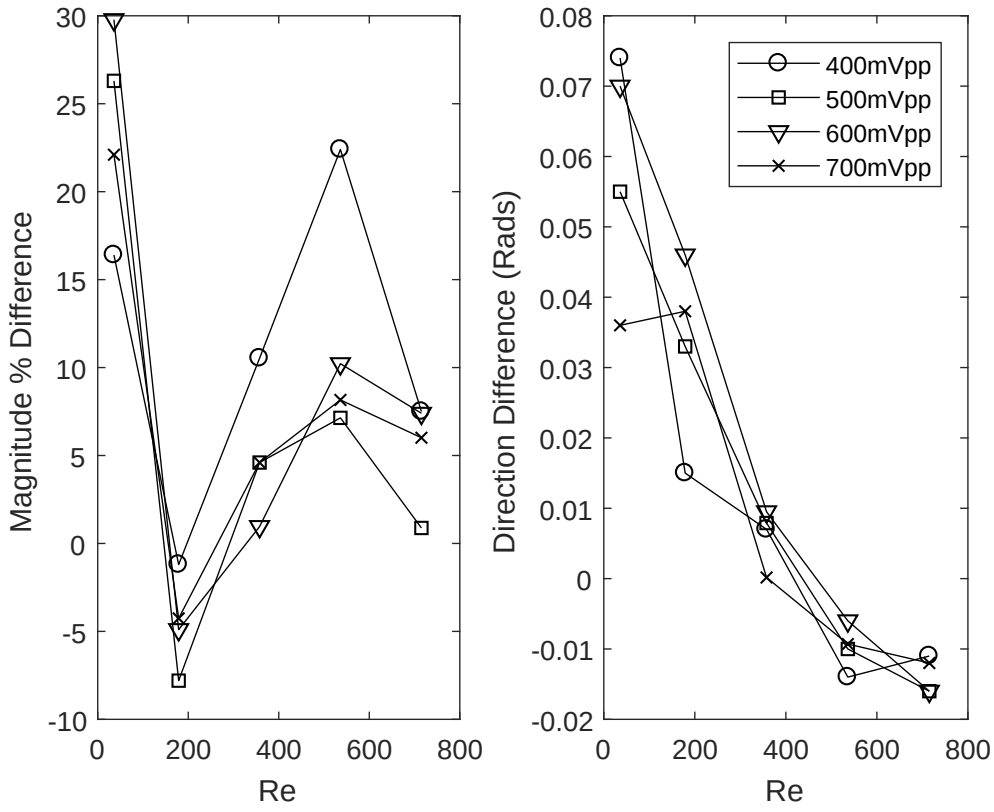

Figure C.5: Plots showing the average deviation from an undisturbed velocity field caused by the presence of the ultrasonic field showing deviations of (a) magnitude and (b) direction as a function of sphere Reynolds number for various acoustic field intensities quantified by the peak to peak voltage of the unsimplified signal driving the transducer.

Appendix D Fluorometry

Disodium fluorescein was chosen as the particle material because it is a well characterized fluorescent die, which will fluoresce when excited by ultraviolet light. It has a peak excitation wavelength of 480 nm and a peak emission wavelength of 525 nm. The intensity of the emitted light depends on the intensity of the absorbed light, the concentration of disodium fluorescein, and the solution pH.[67] Taking advantage of this response a fluorometer (Turner Designs PicoFlour 8000-003) was used to measure the concentration of a sample, which in turn can be used to determine the mass, or number of particles present, in a sample. The linearity of the fluorometer was measured by preparing a known concentration fluorescein solution and measuring the fluorescein concentration with the fluorometer. Then a serial dilution was performed, halving the concentration and measuring the resulting concentration. A plot of the known and measured fluorescing concentration is shown in Fig. D.1, showing that the fluorometer is very linear for concentrations above 10^{-8} molar, therefore this was used as the noise floor for the fluorometer measurements, and scavenging experiments were carried out until the measured concentration was above this threshold, any data below the linearity threshold was discarded.

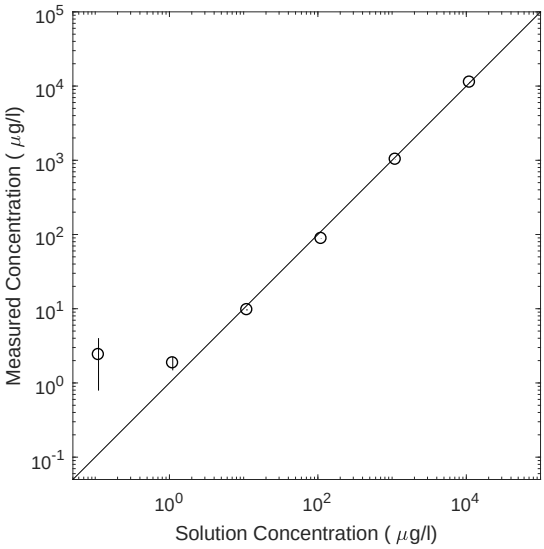

Figure D.1: Plot showing the linearity of the fluorometer used to measure particle concentrations.

As the solution components can change the measured concentration, a series of tests were performed to determine if the presence of propylene glycol in a sample would impact the measured

fluorescein concentration. First, a known concentration solution of fluorescein and water was prepared, then 3 ml of this solution was added to a measurement cuvette, and 1 ml of distilled water or propylene glycol was mixed in, this simulates the addition of the drop liquid, however is by far in excess of the volume of even the largest diameter drop tested, therefore any difference in the concentration measurement due to the presence of propylene glycol would be exaggerated. This test found that the measured fluorescein concentrations with and without propylene glycol were within the repeatability of the fluorometer, and therefore the presence of propylene glycol in the sample was determined to negligibly impact the measurement accuracy.

Appendix E Nozzle construction and validation

The nozzle used in this experiment consisted of 3 stages: a divergent region as flow entered the nozzle, a series of flow straighteners, and a convergent nozzle with a fifth order polynomial contraction based on the design of Bell and Mehta.[10] Each stage was separated by a ~ 0.5 mm mesh to promote mixing within the nozzle and evenly distribute the suspended particles. A schematic of the nozzle is shown in Fig. E.1, a detail drawing of the nozzle portion is shown in Fig. E.2. The velocity profile for this jet was measured, with hand held anemometer (TSI Velocicalc 9545) mounted on a transverse, at various locations along the jet. As Fig. E.3 shows, the resulting jet had a velocity profile that varied by only 2% from the average.

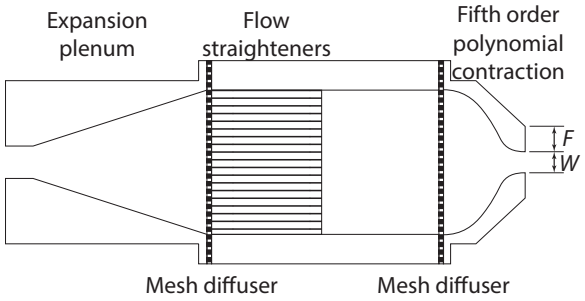

Figure E.1: Nozzle used to produce the laminar jet for the experiments herein. It consists of a divergent section, a mesh diffuser, a bank of flow straighteners, a second mesh diffuser, and a convergent nozzle.

The particle concentration within the jet was measured using flow visualization. A 0.5 W argon-ion laser was spread into a sheet using a series of cylindrical lenses. This sheet was aligned along the axis of the jet. A fog generator was installed upstream of the jet, seeding water droplets into the nozzle. A fog generator was used instead of the particle generator as it could produce a far larger concentration of particles, which allowed for the jet to be visualized. The configuration of the flow visualization is shown in Fig. E.4. A camera (Cannon EOS T3i) was mounted perpendicular to the jet allowing 1 ms exposure images to be taken showing the location of droplets transported within the jet. An example image of the fog laden jet is shown in Fig. E.5.

To get a time average of the particle concentration 1024 images were taken of the jet. These images were converted to binary images, with a pixel value of 1 if illuminated fog was present within the pixel, and 0 otherwise. These images were then summed to obtain a 10 bit image of the jet concentration. This test was performed for the isolated jet, for the jet through the transducer with

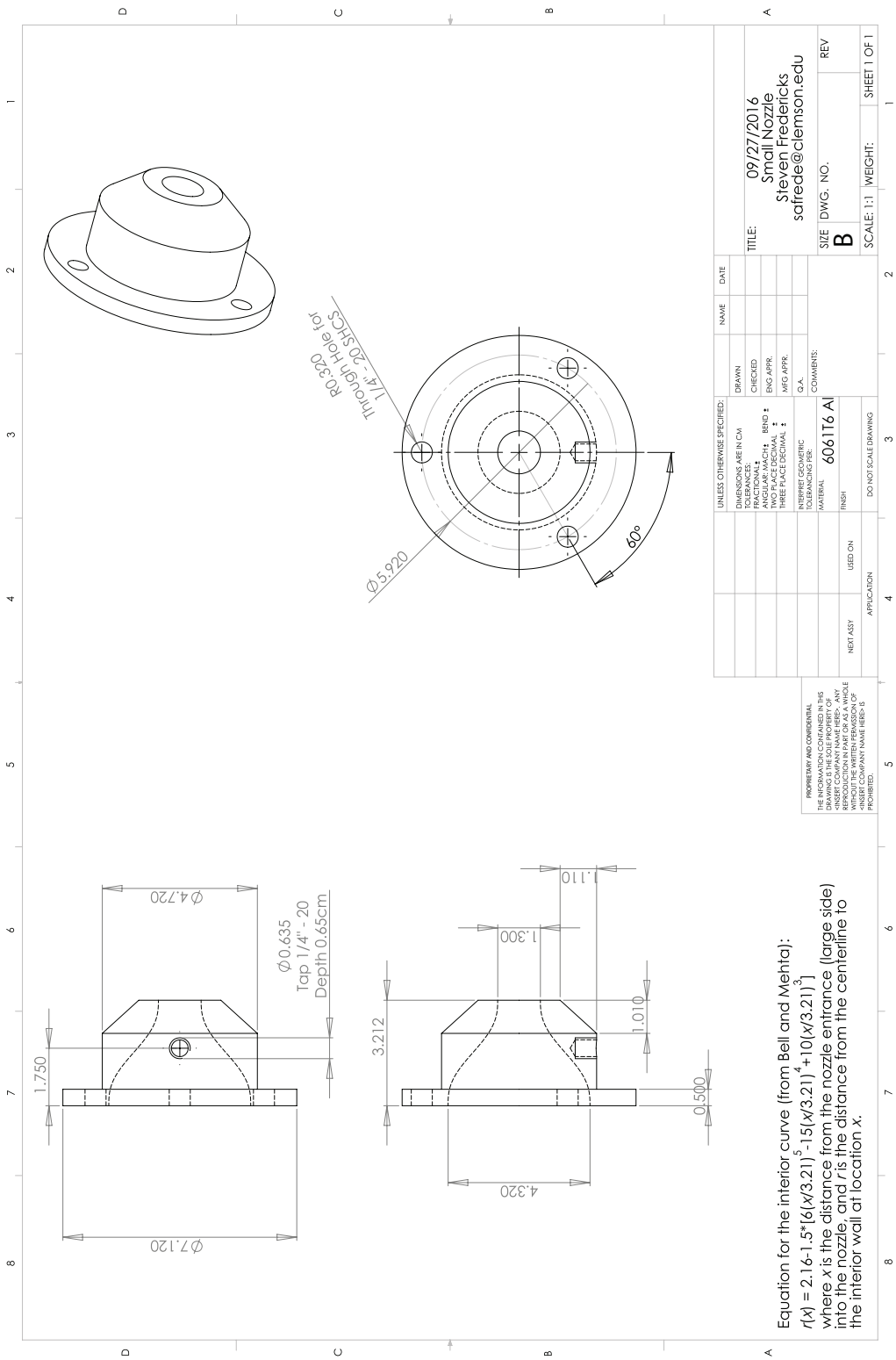

Figure E.2: A machine drawing of the fifth order polynomial contraction nozzle based on the design of Bell and Mehta[10]

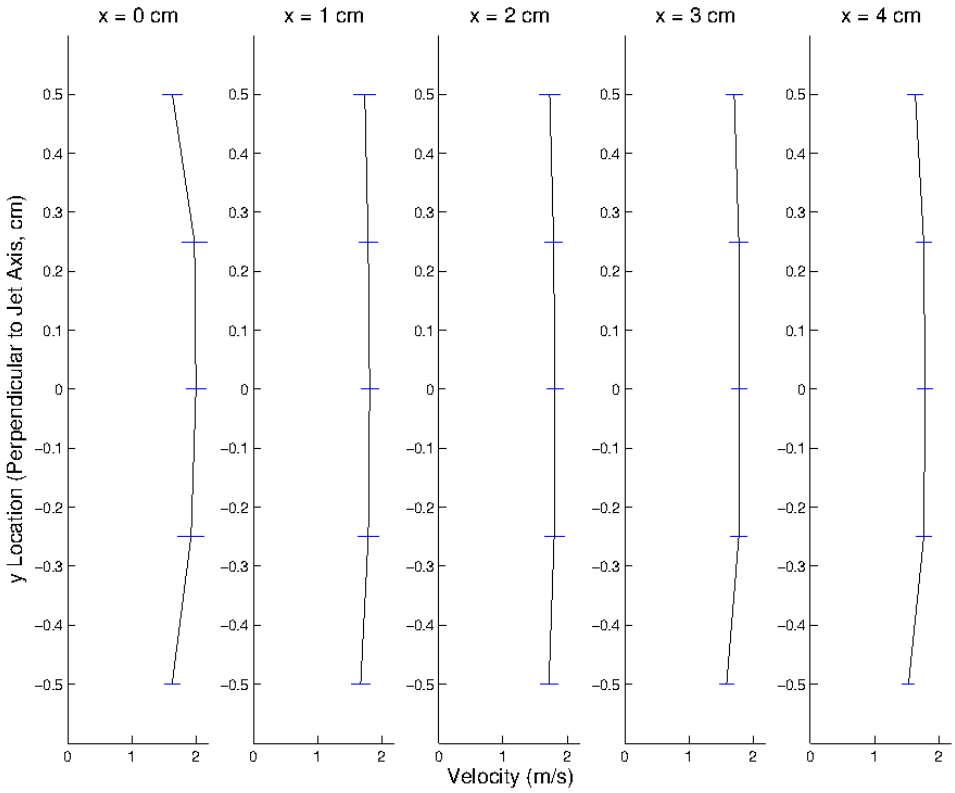

Figure E.3: Jet velocity profile at various downstream locations, the location of the levitating drop was approximately 2 cm downstream. The horizontal bars show 95% confidence intervals.

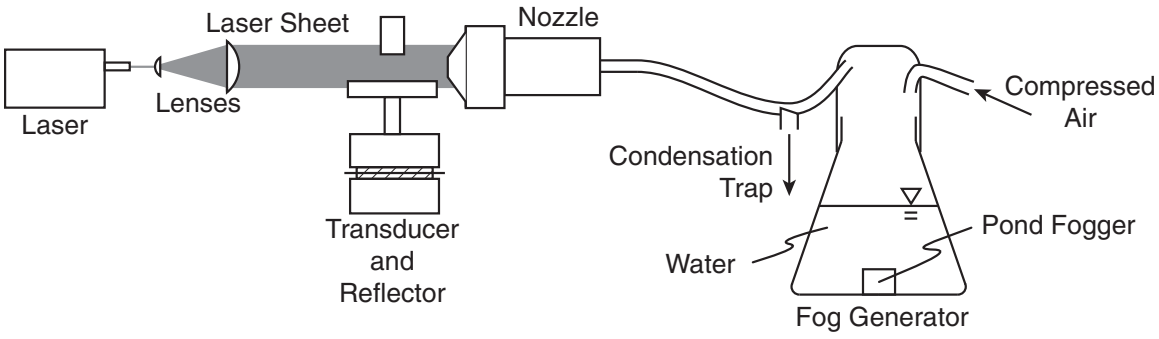

Figure E.4: Experimental configuration for imaging the boundaries of the jet in order to determine the mixing of quiescent fluid with the jet fluid. This will be used to determine the potential core of the jet.

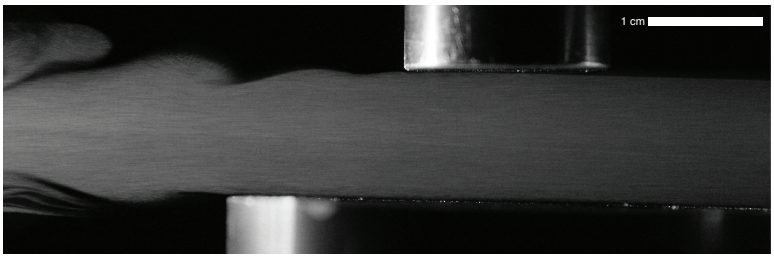

Figure E.5: Example 1 ms exposure of the fog laden jet through the laser sheet, dark area is the quiescent fluid and the light area is the illuminated fog. The transducer and reflector are visible below and above the jet.

no acoustic field, and through the transducer with an acoustic field. The results of these tests are shown in Figs. E.6, E.7, and E.8 respectively. In these figures, the quiescent fluid is black, and the illuminated jet is white, with the mixing layer a grayscale with grayscale intensity related to droplet concentration within the jet. The region of the flow where the concentration value has dropped to less than the exit concentration is outlined in gray. As these results show, the experimentation region of the jet, where the scavenging drop is levitated, has a uniform concentration equal to the concentration at the outlet of the nozzle.

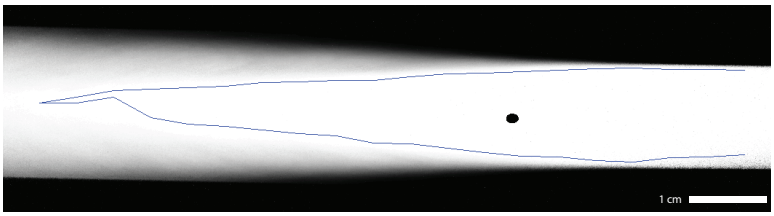

Figure E.6: Ten bit false grayscale image of the concentration gradients within the free jet. The region of uniform concentration is outlined with gray, and the location of the levitated drop is shown as a black circle.

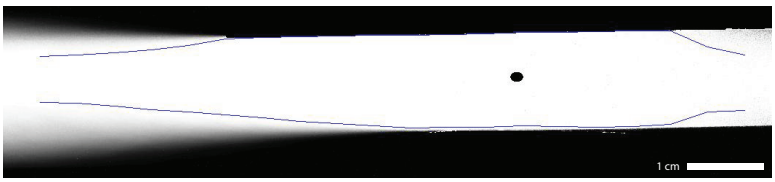

Figure E.7: Ten bit false grayscale image of the concentration gradients within the jet as it traverses the deactivated transducer. The region of uniform concentration is outlined with gray, and the location of the levitated drop is shown as a black circle. The transducer and reflector have been masked out.

This test shows that there is negligible mixing of the particle laden jet and the quiescent

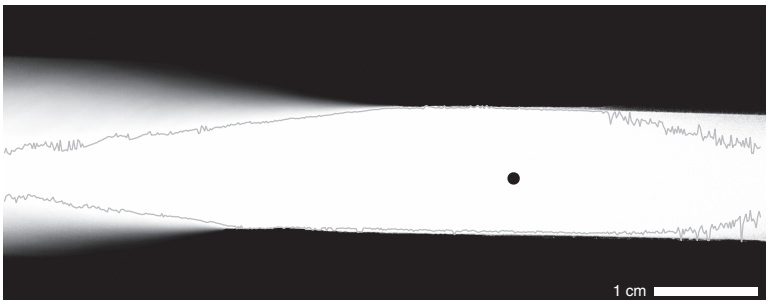

Figure E.8: Ten bit false grayscale image of the concentration gradients within the jet as it traverses the energized transducer which is producing an acoustic field. The region of uniform concentration is outlined with gray, and the location of the levitated drop is shown as a black circle. The transducer and reflector have been masked out.

fluid it is intruding into at the location of the levitating droplet, however it does not reveal insight into the radial concentration of particles within the jet, and it may still be possible for there to be some discrepancy between the concentration along the jet centerline and some location offset from the centerline. To test this the jet was loaded with fluorescein particles, as in a normal scavenging run. a 3 μm Teflon filter was clamped to the nozzle outlet, as in a normal scavenging run, and the fluorescein particles were allowed to deposit onto the filter. The filter was then removed from the nozzle, back lit, and imaged at 1x magnification using a Canon Rebel T3i camera, a sample filter deposition image is shown in Fig. E.9. There is a slight ring surrounding the main deposition, this ring is caused by particles which deposited in on the filter, but were blown off and redeposited to the location of the edge of the filter clamp. This should not interfere with the measurement of radial particle concentration, as this repositioning of particles should occur uniformly over the entire deposit. The filter deposit images were processed by subtracting the background, applying a small Gaussian blur, and radially averaging the intensity of the transmitted light through the deposit. From Beer's law, the transmitted light intensity is proportional to the amount of particles deposited. The overall average of the transmitted light intensity across the entire deposit is proportional to the measured mass deposited via fluorometry, so the relative concentration of particles in the jet was determined by dividing the radial average by the overall average and a plot of spatial variation in the jet particle concentration is shown in Figs. E.10 and E.11 for 5.9 μm and 12.6 μm particles respectively. The solid line in these figures shows the relative particle concentration, and the dashed line shows the nominal position of a levitated drop in the jet. As these figures show, the drop is exposed to approximately the average concentration, however there is some minor spatial variation

in the particle concentration. This variation is greater for the larger particles.

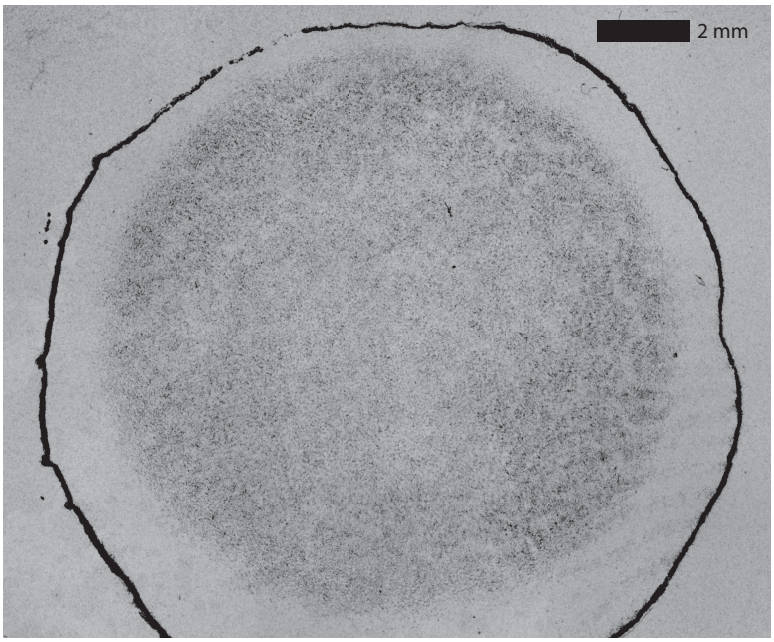

Figure E.9: Photograph of a filter loaded with 5.9 μm fluorescein particles, used to determine the upstream particle concentration, or the total number of particles available for the drop to scavenge.

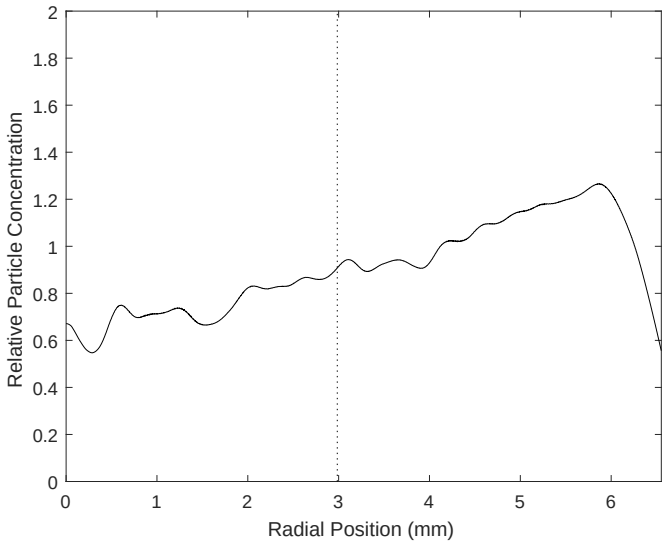

Figure E.10: Plot of the radial concentration of particles collected in the filter to determine the upstream particle concentration for 5.9 μm particles. The dashed line shows approximately the location of a levitated droplet.

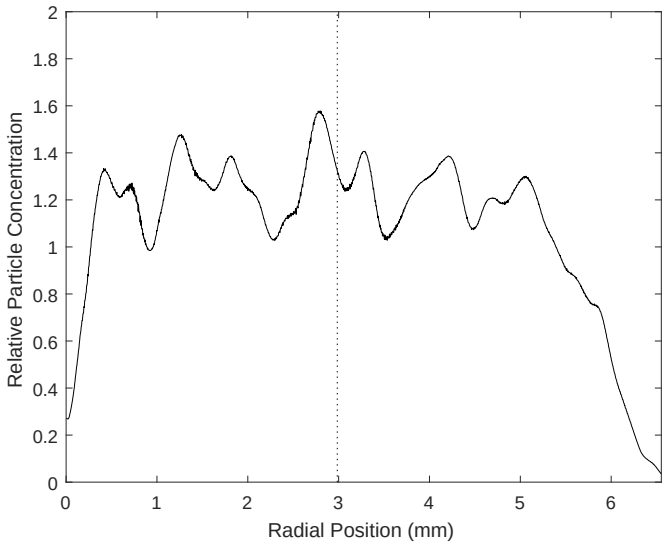

Figure E.11: Plot of the radial concentration of particles collected in the filter to determine the upstream particle concentration for 12.6 μm particles. The dashed line shows approximately the location of a levitated droplet.

Appendix F Scavenging correction details

These three contributors can be corrected for. To correct for the flowrate drop during the filter collection, a series of experiments were performed measuring the filter collection as described in section 4.1 to measure the mass the filter would collect, m_f, then repeating the measurement, but increasing the total flowrate through the system to match the unobstructed flowrate, and measuring the mass which would be present in the unobstructed jet, m_∞. By taking the ratio of the filter mass collection rates a correction factor was obtained. Figure F.1 shows the ratio of mass exiting the nozzle with and without the filter in place Stokes number based on the jet diameter, Stk_W. As this figure shows, there is an increase in scavenging for small jet Stokes numbers, and a decrease for large Stk_W.

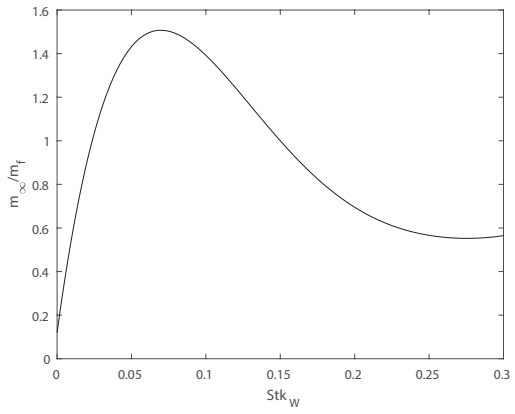

Figure F.1: Ratio of particle mass exiting the nozzle with and without the filter as a function of jet Stokes number, Stk_W, which can be used correct for the decrease in flowrate caused by the presence of the filter at the nozzle outlet.

The particle phase compression can be accounted for by simulating the particle trajectories as they travel from the nozzle to the drop. The acoustic radiation force, F_{ar}, exerted by the acoustic field on the particles was calculated with the formulation due to Settnes and Bruus:[100]

$$F_{ar} = F_{max} \sin(2kx) \tag{F.1}$$

where

$$F_{max} = \frac{1}{2}\pi\Phi\left(\frac{\kappa_p}{\kappa}, \frac{\rho_p}{\rho}, \frac{2\delta}{d}\right) kE_{ac}d^3, \tag{F.2}$$

$$\Phi\left(\frac{\kappa_p}{\kappa},\frac{\rho_p}{\rho},\frac{2\delta}{d}\right)=\frac{1}{3}f_1\left(\frac{\kappa_p}{\kappa}\right)+\frac{1}{2}f_2\left(\frac{\rho_p}{\rho},\frac{2\delta}{d}\right), \tag{F.3}$$

$$f_1\left(\frac{\kappa_p}{\kappa}\right)=1-\frac{\kappa_p}{\kappa}, \tag{F.4}$$

$$f_2\left(\frac{\rho_p}{\rho},\frac{2\delta}{d}\right)=\Re\left[\frac{2\left[1-\gamma\left(\frac{2\delta}{d}\right)\right]\left(\frac{\rho_p}{\rho}-1\right)}{2\frac{\rho_p}{\rho}+1-3\gamma\left(\frac{2\delta}{d}\right)}\right], \tag{F.5}$$

$$\gamma\left(\frac{2\delta}{d}\right)=-\frac{3}{2}\left[1+i\left(1+\frac{2\delta}{d}\right)\right]\frac{2\delta}{d}, \tag{F.6}$$

$$\delta=\sqrt{\frac{2\nu}{\omega}}, \tag{F.7}$$

$$k=\frac{2\pi}{\lambda} \tag{F.8}$$

where x is the object location within the field, E_{ac} is the acoustic energy density, d is the diameter of the object F_{ar} is acting upon, λ is the acoustic wavelength, ρ is the air density, ρ_p is the particle density, κ and κ_p are the compatibilities of air and the particle respectively, ν is the air kinematic viscosity, and ω is the angular frequency of the acoustic wave. The acoustic energy density was estimated by levitating a known volume water drop, then reducing the field strength until the gravity balanced F_{ar} and the drop fell. The drag experienced by the particles, F_d, resisting the action of F_{ar} was calculated as Stokes drag:

$$F_d=3\pi\rho\nu dU \tag{F.9}$$

where U is the particle velocity. A representative trajectory plot from this simulation is shown in Fig. F.2. A correction factor was created by taking the ratio of the particle concentration at the nozzle exit, m_∞ and the concentration at the drop location, m_D. Figure F.3 shows how this correction varies with particle diameter for various jet velocities and drop sizes.

Finally the increased deposition in the tubing during the filter collection due to different tube bend geometry upstream of the nozzle can be accounted for using the tube deposition model

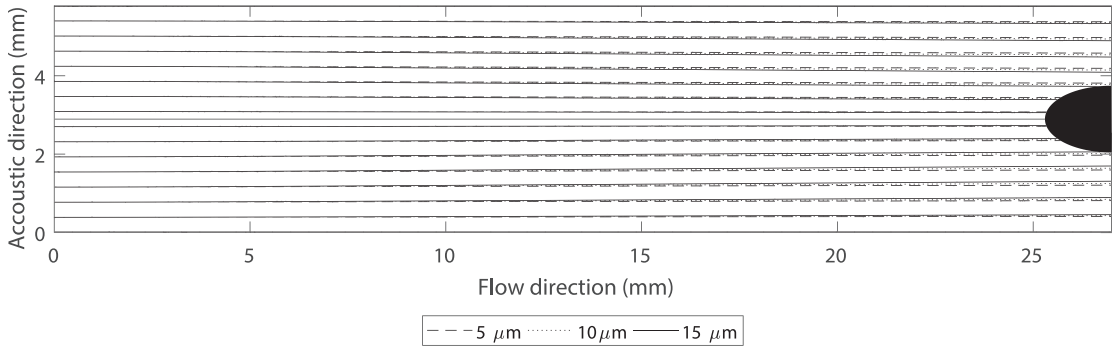

Figure F.2: Representative particle trajectories showing compression of particle phase during transit through the acoustic field to the drop surface. Simulation shown is for a 3 mm diameter drop with $\alpha = 0.5$ exposed to a 2.66 m/s jet, which is the average case for the experimental conditions presented herein.

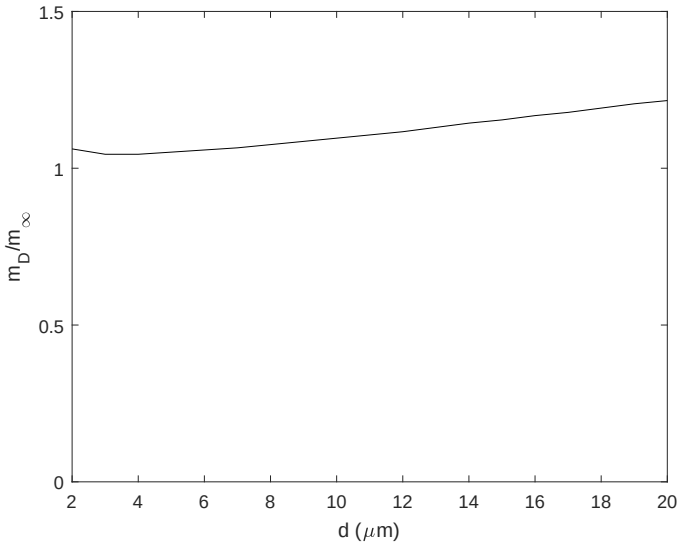

Figure F.3: Ratio of the particle concentrations at the nozzle inlet and drop location for a 3 mm drop with $\alpha = 0.5$ in a 2.66 m/s jet, which is representative of the experimental conditions herein. This ratio can be used to correct for the influence of the acoustic radiation force on measured scavenging.

due to McFarland *et al.*,[66] which determines the fraction of particles which penetrate a tube bend, P:

$$P = \exp\left[\frac{4.61 + G\theta Stk_T}{1 + H\theta Stk_T + I\theta Stk_T^2 + J\theta^2 Stk_T}\right] \tag{F.10}$$

where Stk_T is the stokes number calculated based on the tube diameter, T, θ is the bend angle in radians, and G, H, I, and J are functions of the curvature ratio, β:

$$\beta = \frac{T}{b} \tag{F.11}$$

where b is the tube bend diameter, and the functions G, H, I, and J are:

$$G = -0.9526 - 0.05686\beta \tag{F.12}$$

$$H = \frac{-0.297 - 0.0174\beta}{1 - 0.07\beta + 0.0171\beta^2} \tag{F.13}$$

$$I = -0.306 + \frac{1.895}{\beta^{0.5}} - \frac{2.0}{\beta} \tag{F.14}$$

$$J = \frac{0.131 - 0.132\beta + 0.000383\beta^2}{1 - 0.129\beta + 0.0136\beta^2} \tag{F.15}$$

Figure F.4 shows an example plot of the correction factor accounting for different deposition in the tube bends upstream of the nozzle in the configurations during a scavenging test and a filter test at a fixed volumetric flow rate of 12.25 liters per minute, which it in the range of experiments presented herein.

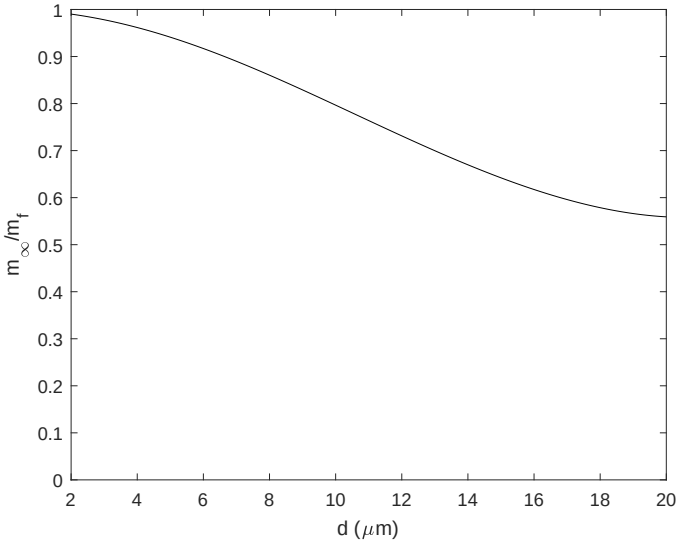

Figure F.4: Ratio of the particle concentration at the nozzle exit when the upstream tubing is in the configuration of a filter collection test to the nozzle exit concentration for the tubing configuration during a scavenging test. This change in particle concentration is due to deposition on the tube walls due to tube bends.

Appendix G Derivation of improved model accounting for drop shape

The model for scavenging presented in Eq. (3.10) from Chapter 3 is reproduced below for convenience:

$$E \sim \frac{\Gamma A_s}{n_\infty U A_d} \tag{G.1}$$

where Γ is the flux of particles to the drop surface, A_s is the drop surface area, n_∞ is the free stream drop concentration, and A_d is the drop projected area in the direction of the flow.

In the case of a spherical drop the equations for the surface area:

$$A_{s,\sigma} = \pi D^2 \tag{G.2}$$

and projected area of a sphere:

$$A_{d,\sigma} = \frac{\pi}{4} D^2 \tag{G.3}$$

are substituted into Eq. (G.1) resulting in the following model for sphere scavenging, E_σ:

$$E_\sigma \sim \frac{\Gamma}{n_\infty U} \frac{\pi D^2}{\frac{\pi}{4} D^2} \tag{G.4}$$

In the case of a drop deformed to be an oblate spheroid in the flow orientation of the experiments herein, the drop surface area is found from a geometric expression for the surface area of an oblate spheroid, based on the major and minor radii of the drop, h and v respectively, as defined in Fig 3.2:

$$A_{s,o} = 2\pi h^2 \left[1 + \frac{\alpha^2}{\sqrt{1-\alpha^2}} \tanh^{-1}\left(\sqrt{1-\alpha^2}\right) \right] \tag{G.5}$$

and the projected area of the drop will be the area of an ellipse:

$$A_{d,o} = \pi h^2 \alpha \tag{G.6}$$

Substituting these into Eq (G.1) results in the following model for scavenging of an oblate spheroid

in the flow orientation of the presented experiments, E_o:

$$E_o \, \frac{\Gamma}{n_\infty U} \left[\frac{2}{\alpha} \left(1 + \frac{\alpha^2}{\sqrt{1-\alpha^2}} \tanh^{-1} \left(\sqrt{1-\alpha^2} \right) \right) \right] \tag{G.7}$$

Taking the ratio of E_σ and E_o as defined in Eqs. (G.4) and (G.7) causes Γ, n_∞, and U to cancel and recovers the shape dependent correction factor in Eq. (3.11) from Chapter 3:

$$\frac{E_\sigma}{E_o} = \frac{2\alpha}{1 + \frac{\alpha^2}{\sqrt{1-\alpha^2}} \tanh^{-1} \left(\sqrt{1-\alpha^2} \right)} \tag{G.8}$$

The same method can be applied for a deformed drop in the flow orientation typical of rain or sprays. In this case the drop is still assumed to be an oblate spheroid, therefore the expression of the drop surface area, $A_{s,r}$, is the same as for the flow orientation of the experiment herein:

$$A_{s,r} = 2\pi h^2 \left[1 + \frac{\alpha^2}{\sqrt{1-\alpha^2}} \tanh^{-1} \left(\sqrt{1-\alpha^2} \right) \right] \tag{G.9}$$

and the projected area of a deformed drop in this flow orientation is the area of a circle with a radius of h:

$$A_{d,r} = \pi h^2 \tag{G.10}$$

Substituting these areas into Eq. (G.1) gives the following expression for scavenging of a deformed drop in the flow orientation of rain, E_r:

$$E_r \, \frac{\Gamma}{n_\infty U} \left[2 \left(1 + \frac{\alpha^2}{\sqrt{1-\alpha^2}} \tanh^{-1} \left(\sqrt{1-\alpha^2} \right) \right) \right] \tag{G.11}$$

By taking the ratio of E_σ and E_r as given by Eqs. (G.4) and (G.11), the Γ, n_∞, and U terms cancel and the shape dependent model presented in Eq. (3.17) is recovered:

$$\frac{E_\sigma}{E_r} = \frac{2}{1 + \frac{\alpha^2}{\sqrt{1-\alpha^2}} \tanh^{-1} \left(\sqrt{1-\alpha^2} \right)} \tag{G.12}$$

Appendix H Additional ring data

To investigate the influence of S/W on the observed ring deposition patterns, two additional sets of data are presented herein. The first is shown in Fig. H.1, and contains the data from 44 deposition rings collected for $S/W = 0.01$ and Stk_W between 0.011 and 0.031. The data is binned in Stk_W bin widths of 0.06. The error bars show 95% confidence intervals. This data is represented with triangles, and is presented along with the data from Fig. 4.4, represented by circles, for ease of comparison. This figure shows that, for the range of Stk_W and S/W investigated, the ring dimensions vary with Stk_W in the same qualitative fashion, regardless of S/W. Also, at a given Stk_W, the ring inner and outer diameters are larger for the larger value of S/W, while the ring thickness appears to be insensitive to S/W.

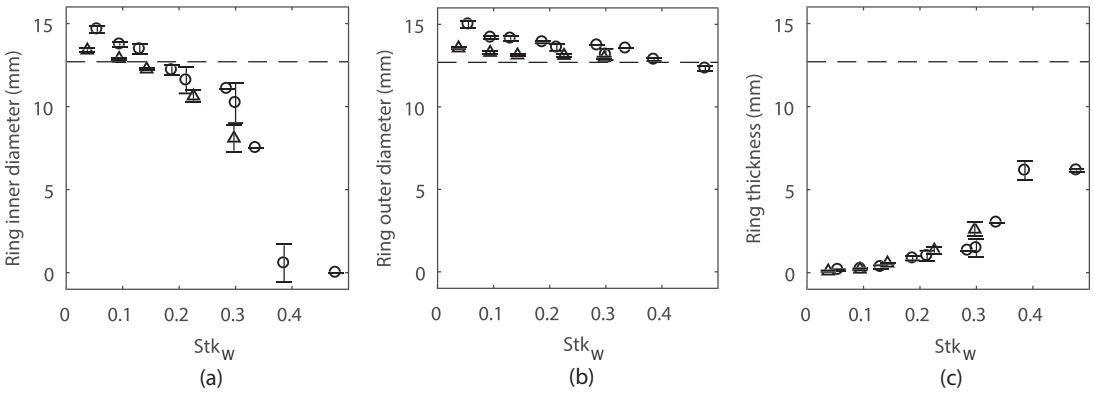

Figure H.1: Plots showing how variations in Stk_W influence small S/W impactor ring deposit geometries for (a) ring inner diameter, (b) ring outer diameter, and (c) ring thickness two values of S/W. Here $\circ$ is data from Fig. 4.4 with $S/W = 0.047$, and $\triangle$ is data taken at $S/W = 0.01$. The dashed lines in (a) - (c) are the nozzle diameter, W.

The second set of data is presented in Fig. H.2, and contains the unbinned data from 22 ring deposits at $Stk_W = 0.013$, for a range of S/W. Of note, $Stk_W = 0.013$ is the smallest Stk_W explored in either data set presented in Fig. H.1, and is where the largest influence of S/W should be observed. As Fig. H.2 shows, the inner and outer ring diameters both increase with S/W, and by approximately the same amount. Concomitantly, the ring thickness is relatively insensitive to S/W for the parameter space tested.

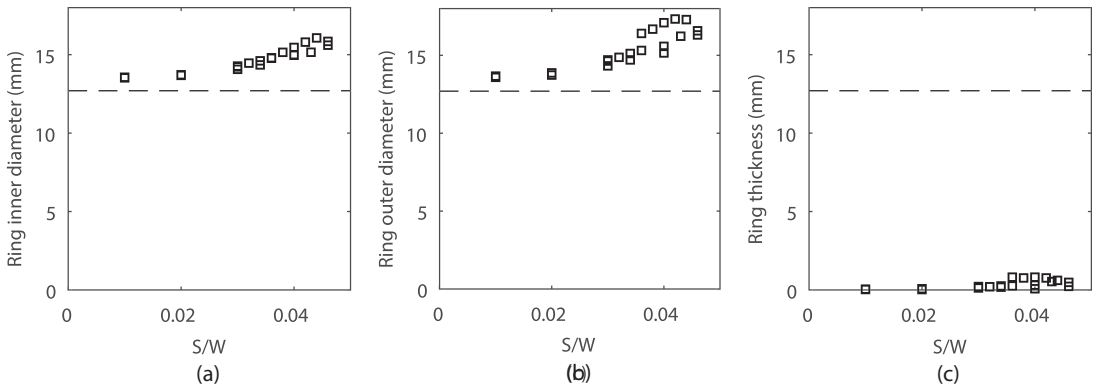

Figure H.2: Plots showing how small S/W impactor ring deposit geometry is related to S/W for fixed $Stk_W = 0.013$ for (a) ring inner diameter, (b) ring outer diameter, and (c) ring thickness with S/W for $Stk_W = 0.013$. The dashed lines in (a) - (c) are the nozzle diameter, W.

Appendix I Additional ring images

Below are presented additional photographs of the ring-shaped particle deposits on the microscope slide. Figure I.1 shows an additional set of impactor ring images which were captured for $S/W = 0.047$, and Fig. I.2 shows an set of photographs captured for $S/W = 0.01$.

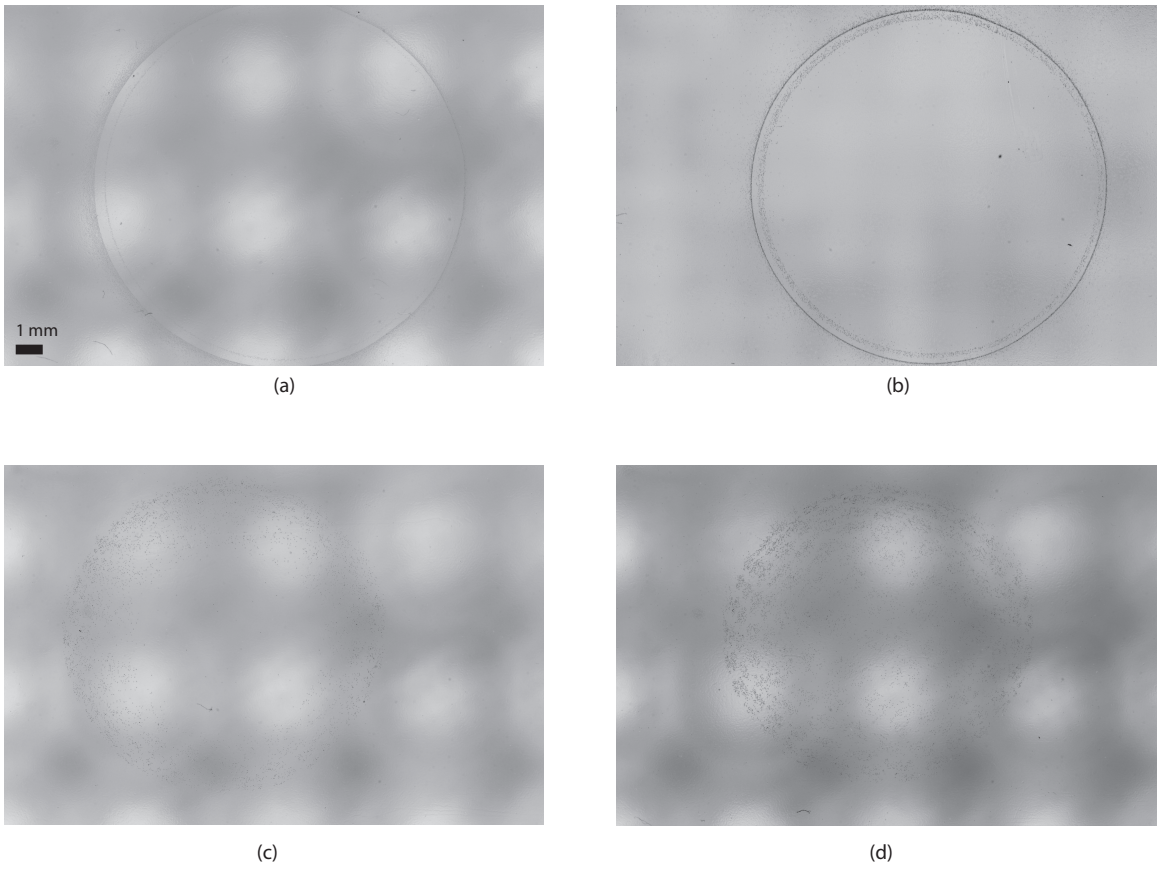

Figure I.1: These photographs shows additional photographs of ring-shaped deposits for the $S/W = 0.047$ condition. The particle diameter, d, and Stk_W for these images are: (a) d =4.71 μm and $Stk_W = 0.04$ for the outer ring, and d =5.93 μm and Stk_W =0.06 for the inner ring (b) d =8.72 μm and $Stk_W = 0.13$ for the outer ring and d =10.98 μm and $Stk_W = 0.20$ for the inner ring (c) d =13.09 μm and $Stk_W = 0.31$ and (d) d =14.65 μm and Stk_W =0.47.

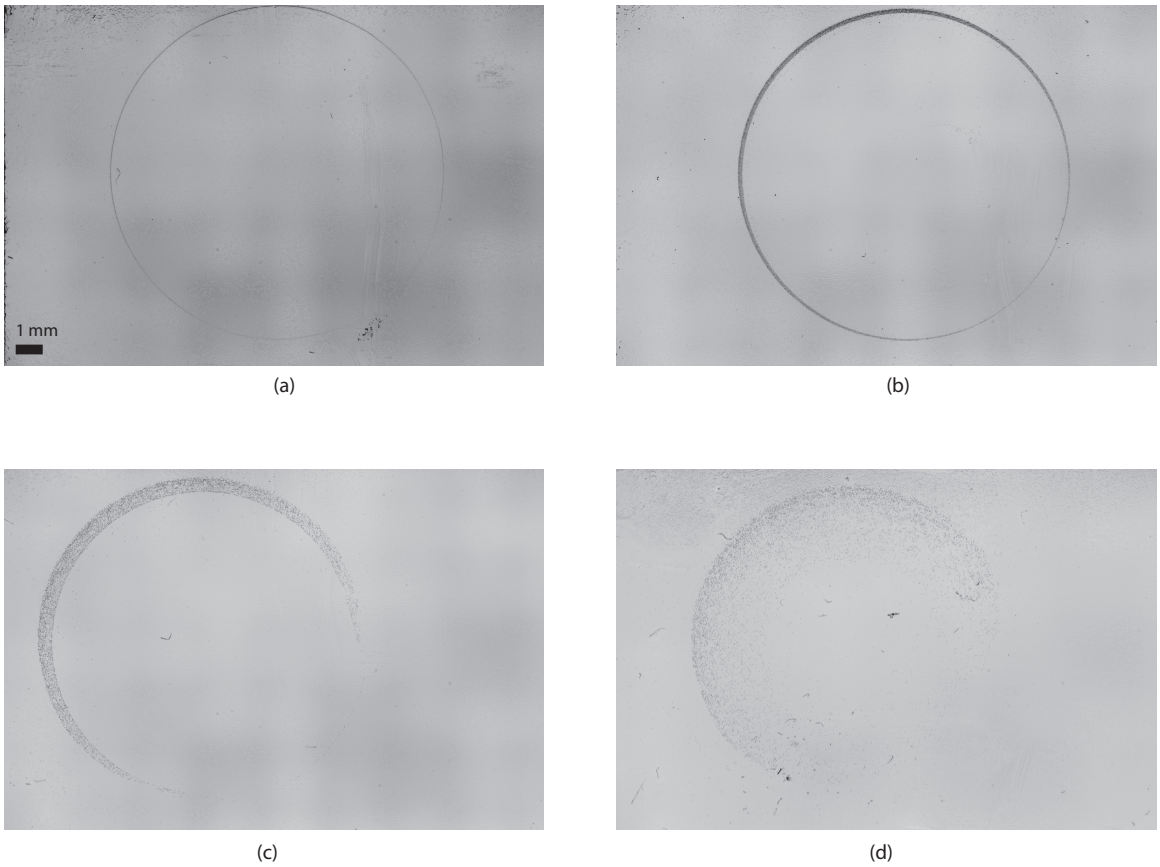

Figure I.2: These photographs shows additional photographs of ring-shaped deposits for the $S/W = 0.01$ condition. The particle diameter, d, and Stk_W for these images are: (a) d =2.56 μm and $Stk_W = 0.013$ (b) $d = 4.98$ μm and $Stk_W = 0.045$ (c) d =9.06 μm and $Stk_W = 0.14$ and (d) d =11.08 μm and $Stk_W = 0.31$.

Appendix J Inertial model for ring deposition

As the order of mangnitude analysis confirms that inertia is the dominant mechanism influencing the particle trajectories near the microscope slide, an inertial model is now developed to partially explain the observed results observed. A simplified model was developed using an approach similar to that by John,[45] but using a simplified, circular flow geometry for the flow as it travels from the nozzle through the slot created by the space between the plate and the flat outer portion of the nozzle. This assumed flow is shown shown in Fig. J.1, and is different from the flow discussed in the order of magnitude analysis in Chapter 4; it consists of uniform velocity within the nozzle, transitioning smoothly via quarter circle arcs to a uniform flow in the slot, with parallel streamlines beginning at the entrance to the slot. In this model it was assumed that particles deviated from their streamline only due to inertia, and that they continued traveling in the nozzle direction for a distance, δ, before following the curvature of their original streamline. Stated another way, the circular trajectories shown in Fig. J.1 (solid lines) were simply displaced downward (dashed lines) by a distance δ, and their impact location on the plate then determined. The particle stopping distance was used for δ, which is the distance a particle penetrates into a quiescent fluid when traveling at an initial velocity U and is decelerated only by Stokes drag.[43] It is defined as:

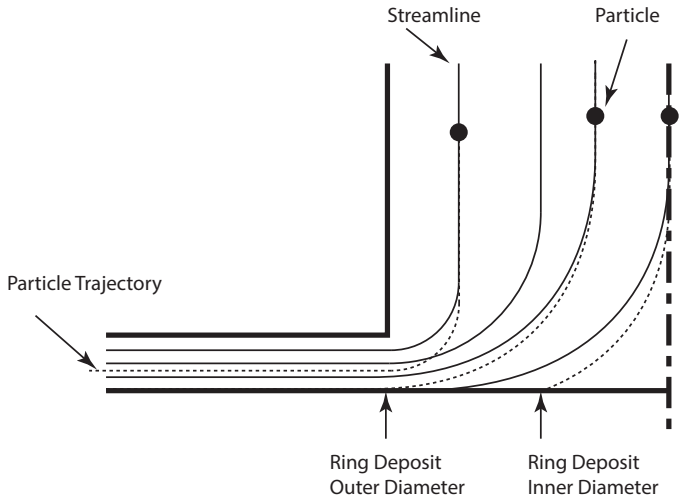

Figure J.1: Simplified particle trajectories for flow through half the impactor nozzle, showing the ring deposit geometry.

$$\delta = WStk_W \tag{J.1}$$

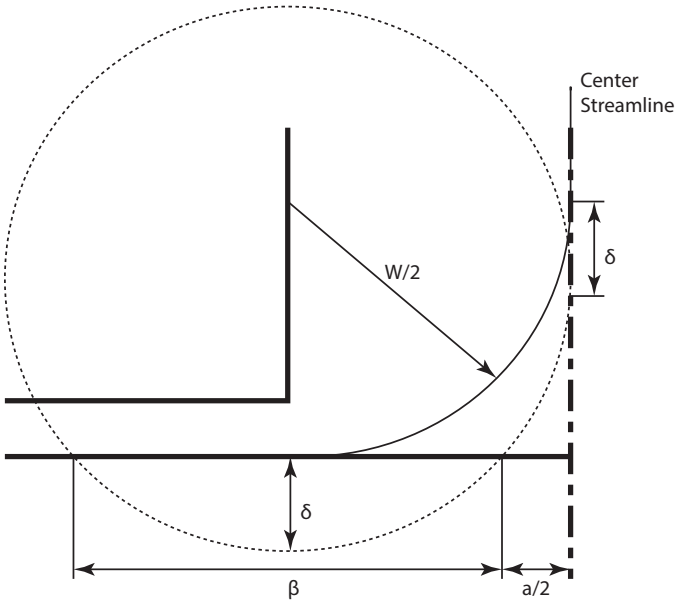

Figure J.2: Geometric reduction of the impaction process, reduced to an intersecting chords problem.

The ring inner diameter can then be estimated as the intersection point between the particle trajectory corresponding to the axial streamline and the plate surface. As the flow was assumed to be circular in this model, this can be reduced to a geometry problem, as shown in Fig. J.2, using the intersecting chords theorem:

$$a = W - \beta = W - 2\sqrt{\delta(W - \delta)} \tag{J.2}$$

where a is the inner diameter of the deposited particle ring, and β is the chord length of the circular streamline defined by its intersection with the slide. In this model the ring outer diameter will always be W due to the assumption that the flow in the slot between the slide and nozzle will be uniform with evenly spaced parallel streamlines beginning at the slot entrance.

A comparison of the results for inner diameter obtained from the above model and the experimental results is presented in Fig. J.3. Although the model is relatively crude, it predicts both the overall trend in the experimental observations, a monotonic decrease in ring inner diameter with Stk, and the value of Stk corresponding to the end of observed ring depositions. However, there are significant differences between the predicted and actual magnitude of the ring diameters shown in Fig. J.3, as large as a factor of three for some Stk. Improvements on this prediction would require a more accurate simulation of the flow and the particle paths in the flow.

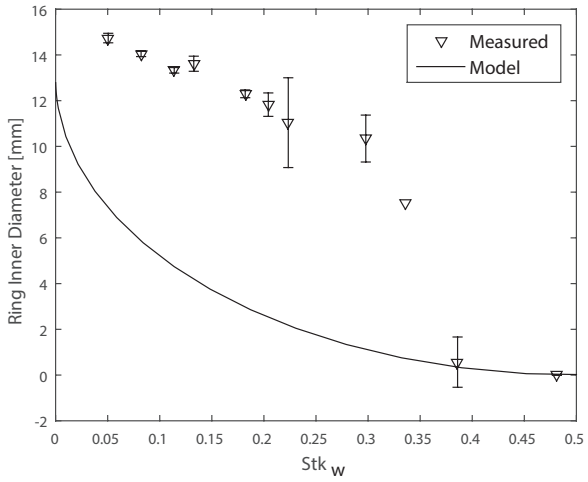

Figure J.3: Comparison between the experimentally observed ring inner diameter, and that predicted by the simplified model.

In order to use the results obtained herein as the basis of a particle spectrometer capable of measuring the particle size distribution, $N(d)$, of a polydisperse sample, the spatial concentration of deposited particles must be found. Though not explored in this work, it is possible that this could be achieved by back lighting and imaging a deposition pattern, and then determining the spatial distribution of the transmitted light intensity measured. By comparing this with the light intensity of the back light alone the deposited particle concentration as a function of radial location, $c(r)$, could be approximated with the Lambert-Beer law:

$$c(r) = \frac{4}{Q_e(d)d(r)^2\pi} \ln\left(\frac{I_0(r)}{I(r)}\right) \tag{J.3}$$

where $I(r)$ is the intensity of the light transmitted through the deposit at point r, and $I_0(r)$ is the light intensity without any deposition at point r, Q_e is the extinction efficiency of the particle, which is a function of the particle size and refractive index, and $d(r)$ is the expected particle size that will be deposited at location r. This estimate for $c(r)$ can also be modeled as a function of $N(d)$ via:

$$c(r) = \int_0^\infty \eta(d)N(d)P(r,d)UTdd \tag{J.4}$$

where $\eta(d)$ is the particle diameter resolved impactor collection efficiency; $P(r,d)$ is the probability that a collected particle having diameter d will deposit at r, as determined by a deposition model,

such as the one developed above; and T is the exposure duration. Therefore $N(d)$ could potentially be found by measuring the radial deposition concentration within an impactor plate deposition pattern. Clearly much work remains before $N(d)$ could be obtained from Eqs. (J.3) and (J.4) due to complexities in actually obtaining several quantities in these equations. A method for obtaining $Q_e(d)$ and $\eta(d)$ are needed as well as a more robust version of $P(r, d)$.

Bibliography

[1] P. J. Adams and J. H. Seinfeld. Predicting global aerosol size distributions in general circulation models. *J. Geophys. Res.*, 107:AAC–4, 2002.

[2] K. Andsager, K. V. Beard, and N. F. Laird. Laboratory measurements of axis ratios for large raindrops. *J. Atmos. Sci.*, 56:2673–2683, 1999.

[3] K. Ardon-Dryer, Y. W. Huang, and Cziczo D. J. Laboratory studies of collection efficiency of sub-micrometer aerosol particles by cloud droplets on a single droplet basis. *Atmos. Chem. Phys. Discuss.*, 15:6207–6236, 2015.

[4] A. Arffman, M. Marjamäki, and J. Keskinen. Simulation of low pressure impactor collection efficiency curves. *J. Aerosol Sci.*, 42(5):329–340, 2011.

[5] K. V. Beard. Experimental and numerical collision efficiencies for submicron particles scavenged by small raindrops. *J. Atmos. Sci.*, 31:1595–1603, 1974.

[6] K. V. Beard. Terminal velocity and shape of cloud and precipitation drops aloft. *J. Atmos. Sci.*, 33:851–864, 1976.

[7] K. V. Beard and C. Chuang. A new model for the equilibrium shape of raindrops. *J. Atmos. Sci.*, 44:1509–1524, 1987.

[8] K. V. Beard and S. N. Grover. Numerical collision efficiencies for small raindrops colliding with micron size particles. *J. Atmos. Sci.*, 31:543–550, 1974.

[9] K. V. Beard, H. T. Ochs, and R. J. Kubesh. Natural oscillations of small raindrops. *Nature*, 342:408–410, 1989.

[10] J. H. Bell and R. D Mehta. Contraction design for small low-speed wind tunnels. Technical report, NASA, 1988.

[11] F. Belosi and V. Prodi. Particle deposition within the inertial spectrometer. *J. Aerosol Sci.*, 18(1):37–42, 1987.

[12] R. N. Berglund and R. Y. H. Liu. Generation of monodisperse aerosol standards. *Environ. Sci. Tech.*, 7:147–153, 1973.

[13] A Berner. Zur ursache sekundärer partikelniederschläge bei impaktoren. *Staub Reinhalt. Luft*, 38(1):1, 1978.

[14] W. Burwash, W. Finlay, and E. Matida. Deposition of particles by a confined impinging jet onto a flat surface at Re=10^4. *Aerosol Sci. Technol.*, 40(3):147–156, 2006.

[15] M. A. Byrne and Jennings S. G. Scavenging of sub-micrometer aerosol particles by water drops. *Atmos. Environ.*, 27A:2099–2105, 1993.

[16] S. Calvert. Venturi and other atomizing scrubbers efficiency and pressure drop. *AIChE J.*, 16:392–396, 1970.

[17] S. Calvert and H. M. Englund. *Handbook of air pollution technology*. Wiley, New York, 1984.

[18] S. Calvert and J. Goldshmid. Wet scrubber system study: Scrubber handbook. Technical report, EPA, 1972.

[19] J. Canny. A computational approach to edge detection. *IEEE Transactions on Pattern Analysis and Machine Intelligence*, 8:679–698, 1986.

[20] D. M. Chate, K. A. Murugavel, S. Tiwari, and G. Beig. Below-cloud rain scavenging of atmospheric aerosols for aerosol deposition models. *Atmos. Res.*, 99:528–536, 2011.

[21] S. C. Chen, C. J. Tsai, H. D. Chen, C. Y. Huang, and G. D. Roam. The influence of relative humidity on nanoparticle concentration and particle mass distribution measurements by the MOUDI. *Aerosol Sci. Technol.*, 45(5):596–603, 2011.

[22] Y. S. Cheng and B. E. Dahneke. Properties of continuum source particle beams: II. beams generated in capillary expansions. *J. Aerosol Sci.*, 10(4):363–368, 1979.

[23] W. E. Clark and K. T. Whitby. Concentration and size distribution measurements of atmospheric aerosols and a test of the theory of self-preserving size distributions. *J. Atmospheric Sci.*, 24(6):677–687, 1967.

[24] A. J. Cohen. Outdoor air pollution and lung cancer. *Environ. Health Perspect.*, 108:743–750, 2000.

[25] B. Dahneke and H. Flachsbart. An aerosol beam spectrometer. *J. Aerosol Sci.*, 3(5):345–349, 1972.

[26] B. Dahneke, J. Hoover, and Y. S. Cheng. Similarity theory for aerosol beams. *J. Colloid Interface Sci.*, 87(1):167–179, 1982.

[27] S. D. Danilov and M. A. Mironov. Mean force on a small sphere in a sound field in a viscous fluid. *J. Acoust. Soc. Am.*, 107:143–153, 2000.

[28] H. M. Davenport and L. K. Peters. Field studies of atmospheric particulate concentration changes during precipitation. *Atmos. Environ.*, 12:997–1008, 1978.

[29] D. L. Davis, M. L. Bell, and T. A. Fletcher. A look back at the London smog of 1952 and the half century since. *Environ. Health Perspect.*, 110:A734–A735, 2002.

[30] J. F. de la Mora and D. E. Rosner. Effects of inertia on the diffusional deposition of small particles to spheres and cylinders at low Reynolds numbers. *J. Fluid Mech.*, 125:379–395, 1982.

[31] D. W. Docker and C. A. Pope. Acute respiratory effects of particulate air pollution. *Annu. Rev. Public Health*, 15:107–132, 1994.

[32] Hahner F., G. Dau, and F. Ebert. Inertial impaction of aerosol particles on single and multiple spherical targets. *Chem. Eng. Technol.*, 17:88–94, 1994.

[33] A. Fonda and H. Herne. Hydrodynamic capture of particles by spheres. *Mining Res. Establ. Rep*, 2086, 1957.

[34] S. Fredericks and J. R. Saylor. Parametric investigation of two aerosol scavenging models in the inertial regime. *J. Aerosol Sci.*, 101:34–42, 2016.

[35] S. Fredericks and J. R. Saylor. Corrigendum to parametric investigation of two aerosol scavenging models in the inertial regime. *J. Aerosol Sci.*, 114:342–343, 2017.

[36] S. K. Friedlander. *Smoke, Dust, and Haze*. Oxford University Press, New York, 1977.

[37] S. K. Friedlander. *Smoke, dust, and haze: fundamentals of aerosol dynamics*. Oxford University Press, New York, 2000.

[38] Y. Goldshmid and S. Calvert. Small particle collection by supported liquid drops. *AIChE J.*, 9:352–358, 1963.

[39] S. A. Grinshpun, G. Mainelis, M. Trunov, R. L. Górny, S. K. Sivasubramani, A. Adhikari, and T. Reponen. Collection of airborne spores by circular single-stage impactors with small jet-to-plate distance. *J. Aerosol Sci.*, 36(5):575–591, 2005.

[40] K. Gunn and W. Hitschfeld. A laboratory investigation of the coalescence between large and small water-drops. *J. of Meteor.*, 8:7–16, 1950.

[41] V. Hampl and M. Kerker. Scavenging of aerosol particles by a falling water droplet. effect of particle size. *J. Colloid Interface Sci.*, 40:305–308, 1972.

[42] V. Hampl, M. Kerker, D. D. Cooke, and E. Matijevic. Scavenging of aerosol particles by a falling water droplet. *J. Atmos. Sci.*, 28:21211–1221, 1971.

[43] W. C. Hinds. *Aerosol Technology: Properties, Behavior, and Measurement of Airborne Particles*. Wiley-Interscience, New York, NY, 1982.

[44] H. Horvath. Atmospheric light absorption - A review. *Atmos. Environ. A-Gen.*, 27:293–317, 1993.

[45] W. John. A simple derivation of the cutpoint of an impactor. *J. Aerosol Sci.*, 30(10):1317–1320, 1999.

[46] W. John, D. N. Fritter, and W. Winklmayr. Resuspension induced by impacting particles. *J. Aerosol Sci.*, 22(6):723–736, 1991.

[47] R. L. Johnson. Relative effects of air pollution on lungs and heart. *Circulation*, 109:5–7, 2004.

[48] M. Kanakidou, J. H. Seinfeld, S. N. Pandis, I. Barnes, F. J. Dentener, M. C. Facchini, R. Van Dingenen, B. Ervens, A. Nenes, C. J. Nielsen, E. Swietlicki, J. P. Putaud, Y. Balkanski, S. Fuzzi, J. Horth, G. K. Moortgat, R. Winterhalter, C. E. L. Myhre, K. Tsigaridis, E. Vignati, E. G. Stephanou, and J. Wilson. Organic aerosol and global climate modelling: a review. *Atmos. Chem. Phys*, 5:1053–1123, 2005.

[49] J. T. Karlsen and H. Bruus. Forces acting on a small particle in an acoustical field in a thermoviscous fluid. *Phys. Rev. E*, 92:043010–1 – 043010–22, 2015.

[50] L. V. King. On the acoustic radiation pressure on spheres. *Proceedings of the Royal Society of London. Series A-Mathematical and Physical Sciences*, 147(861):212–240, 1934.

[51] F. N. Kissell. *Handbook of Dust Control in Mining*. NIOSH Publication Number 2003-147. NIOSH Publications, Cincinnati, OH, 2003.

[52] L. Ladino, O. Stetzer, B. Hattendorf, D. Günther, B. Croft, and U. Lohmann. Experimental study of collection efficiencies between submicron aerosols and cloud droplets. *J. Atmos. Sci.*, 68:1853–1864, 2011.

[53] K. Y. Lai, N. Dayan, and M. Kerker. Scavenging of aerosol particles by a falling water droplet. *J. Atmos. Sci.*, 35:674–682, 1978.

[54] H. Lamb. *Hydrodynamics*. Cambridge University Press, 6th edition, 1932.

[55] I. Langmuir. The production of rain by a chain reaction in cumulus clouds at temperatures above freezing. *J. Meteor.*, 5:175–192, 1948.

[56] K. H. Leong, K. V. Beard, and H. T. Ochs III. Laboratory measurements of particle capture by evaporating cloud drops. *J. Atmos. Sci.*, 39:1130–1140, 1982.

[57] V. G. Levich. *Physicochemical hydrodynamics*. Prentice-Hall, New Jersey, 1962.

[58] B. Y. H. Liu. *Fine Particles: Aerosol Generation, Measurement, Sampling, and Analysis*. Academic Press Inc., New York, 1975.

[59] Chate D. M. and Kamra A. K. Collection efficiencies of large water drops collecting aerosol particles of various densities. *Atmos. Environ.*, 31:1631–1635, 1997.

[60] M. Marjamäki, J. Keskinen, D. R. Chen, and D. Y. H. Pui. Performance evaluation of the electrical low-pressure impactor (ELPI). *J. Aerosol Sci.*, 31(2):249–261, 2000.

[61] V. A. Marple. History of impactors - The first 110 years. *Aerosol Sci. Technol.*, 38(3):247–292, 2004.

[62] V. A. Marple, B. Y. H. Liu, and K. T. Whitby. Fluid mechanics of the laminar flow aerosol impactor. *J. Aerosol Sci.*, 5(1):1–16, 1974.

[63] V. A. Marple, K. L. Rubow, and S. M. Behm. A microorifice uniform deposit impactor (MOUDI): Description, calibration, and use. *Aerosol Sci. Technol.*, 14(4):434–446, 1991.

[64] V. A. Marple and K. Willeke. Impactor design. *Atmos. Environ.*, 10:891–896, 1976.

[65] J. S. Marshall and W. M. Palmer. The distributions of raindrops with size. *J. Meteor.*, 9:327–332, 1948.

[66] A. R. McFarland, H. Gong, A. Muyshondt, W. B. Wente, and N. K. Anand. Aerosol deposition in bends with turbulent flow. *Environ. Sci. Technol.*, 31(12):3371–3377, 1997.

[67] S. Ohkuma and B. Poole. Fluorescence probe measurement of the intralysosomal ph in living cells and the perturbation of pH by various agents. *Proc. Natl. Acad. Sci. USA*, 75:3327–3331, 1978.

[68] T. Oodo, Y. Takashima, and M. Hanzawa. An experimental study of adhesion of particles with a round nozzle impactor. *J. Chem. Eng. Jpn.*, 14(1):76–78, 1981.

[69] S. S. Pak, B. Y. H. Liu, and K. L. Rubow. Effect of coating thickness on particle bounce in inertial impactors. *Aerosol Sci. Technol.*, 16(3):141–150, 1992.

[70] S. H. Park, C. H. Jung, K. R. Jung, B. K. Lee, and Lee K. W. Wet scrubbing of polydisperse aerosols by freely falling droplets. *J. Aerosol Sci.*, 36:1444–1458, 2005.

[71] C. A. Pope, R. T. Burnett, M. J. Thun, E. E. Calle, D. Krewski, K. Ito, and G. D. Thurston. Lung cancer, cardiopulmonary mortality, and long-term exposure to fine particulate air pollution. *JAMA*, 287:1132–1141, 2002.

[72] C. A. Pope, R. T. Burnett, G. D. Thurston, M. J. Thun, E. E. Calle, D. Krewski, and J. J. Godleski. Cardiovascular mortality and long-term exposure to particulate air pollution. *Circulation*, 109:71–77, 2004.

[73] C. A. Pope, M. J. Thun, M. M. Namboodiri, D. W. Dockery, J. S. Evans, F. E. Speizer, and C. W. Heath. Particulate air pollution as a predictor of mortality in a prospective study of U.S. adults. *Am. J. Respir. Crit. Care Med.*, 151:669–674, 1995.

[74] T. S. Pranesha and A. K. Kamra. Scavenging of aerosol particles by large water drops 1. Neutral case. *J. Geophys. Res.*, 101:23,373–23,380, 1996.

[75] V. Prodi, C. Melandri, G. Tarroni, T. De Zaiacomo, M. Formignani, and D. Hochrainer. An inertial spectrometer for aerosol particles. *J. Aerosol Sci.*, 10(4):411–419, 1979.

[76] H. Pruppacher and J. Klett. *Microphysics of Clouds and Precipitation*. Reidel Publishing Company, Dordrecht, 1978.

[77] A. Quérel, M. Monier, A. I. Flossmann, P. Lemaitre, and E. Porcheron. The importance of new collection efficiency values including the effect of rear capture for the below-cloud scavenging of aerosol particles. *Atmos. Res.*, 2013.

[78] Starr J. R. and Mason B. J. The capture of airborne particles by water drops and simulated snow crystals. *Quat. J. Royal Meteor. Soc.*, 92:490–499, 1966.

[79] V. Ramanathan, P. J. Crutzen, J. T. Kiehl, and D. Rosenfeld. Aerosols, climate, and the hydrological cycle. *Science*, 294:2119–2124, 2001.

[80] W. E. Ranz and J. B. Wong. Impaction of dust and smoke particles. *Ind. Eng. Chem.*, 44:1371–1381, 1956.

[81] N. P. Rao, J. Navascues, and J. F. De La Mora. Aerodynamic focusing of particles in viscous jets. *J. Aerosol Sci.*, 24(7):879–892, 1993.

[82] S. Rennecke and A. P. Weber. A novel model for the determination of nanoparticle impact velocity in low pressure impactors. *J. Aerosol Sci.*, 55:89–103, 2013.

[83] J. M. Rocklage, V. A. Marple, and B. A. Olson. Study of secondary deposits in multiple round nozzle impactors. *Aerosol Sci. Technol.*, 47(10):1144–1151, 2013.

[84] R. Roeber. Untersuchungen zur konimetrischen staubmessung. *Staub*, 49:273–295, 1957.

[85] E. Roeckner, G. Bäuml, L. Bonaventura, R. Brokopf, M. Esch, M. Giorgetta, and et al. The atmospheric general circulation model ECHAM 5. PART I: Model description. Technical report, MPI für Meteorologie, 2003.

[86] S. I. Rubinow and J. B. Keller. The transverse force on a spinning sphere moving in a viscous fluid. *J. Fluid Mech.*, 11(3):447–459, 1961.

[87] P. G. T Saffman. The lift on a small sphere in a slow shear flow. *J. Fluid Mech.*, 22(02):385–400, 1965.

[88] P. G. T. Saffman. The lift on a small sphere in a slow shear flow - Corrigendum. *J. Fluid Mech.*, 31:624, 1968.

[89] H. Sakamoto and H. Haniu. A study on vortex shedding from spheres in a uniform flow. *J. Fluids Engng.*, 112:386–392, 1990.

[90] J. R. Saylor. Photobleaching of disodium fluorescein in water. *Exp. Fluids*, 18:445–447, 1995.

[91] J. R. Saylor and B. K. Jones. The existence of vortices in the wakes of simulated raindrops. *Phys. Fluids*, 17:31706–31706(4), 2005.

[92] C. A. Schneider, W. S. Rasband, and K. W. Eliceiri. NIH Image to ImageJ: 25 years of image analysis. *Nature Methods*, 9(7):671, 2012.

[93] K. B. Schnelle and C. A. Brown. *Air Pollution Control Technology Handbook*. The Mechanical Engineering Handbook Series. CRC Press, Boca Raton, FL, 2002.

[94] J. Schwartz. What are people dying of on high air pollution days? *Environ. Res.*, 64:26–35, 1994.

[95] J. Schwartz and D. W. Dockery. Increased mortality in Philadelphia associated with daily air pollution concentrations. *Am. Rev. Respir. Dis.*, 145:600–604, 1992.

[96] J. Schwartz, F. Laden, and A. Zanobetti. The concentration-response relation between PM2.5 and daily deaths. *Environ. Health Perspect.*, 110(10):1025–1029, 2002.

[97] A. Seaton, W. MacNee, K. Donaldson, and D. Godden. Particulate air pollution and acute health effects. *The Lancet*, 345:176–178, 1995.

[98] J. H. Seinfeld and S. N. Pandis. *Atmospheric chemistry and physics: from air pollution to climate change*. Wiley & Sons, New Jersey, 2006.

[99] V. Sethi and W. John. Particle impaction patterns from a circular jet. *Aerosol Sci. Technol.*, 18(1):1–10, 1993.

[100] M. Settnes and H. Bruus. Forces acting on a small particle in an acoustical field in a viscous fluid. *Phys. Rev. E*, 85(1):016327, 2012.

[101] C. L. Shen, W. J. Xie, and B. Wei. Parametric resonance in acoustically levitated water drops. *Phys. Lett. A*, 374(23):2301–2304, 2010.

[102] C. L. Shen, W. J. Xie, and B. Wei. Parametrically excited sectorial oscillation of liquid drops floating in ultrasound. *Phys. Rev. E*, 81(4):046305, 2010.

[103] W. G. N. Slinn. Precipitation scavenging: Some problems, approximate solutions, and suggestions for future research. In R. G. Semonin and R. W. Beadle, editors, *Precipitation scavenging (1974): Proceedings of a symposium held at Champaign, Illinois, October 14-18, 1974*, ERDA symposium series; 41, pages 1–60, Springield, Va., 1977.

[104] W. G. N. Slinn. Precipitation scavenging. *Atmospheric Science and Power Production*, pages 466–532, 1984.

[105] W. G. N. Slinn and J. M. Hales. A reevaluation of the role of thermophoresis as a mechanism of in-and below-cloud scavenging. *J. Atmos. Sci.*, 28(8):1465–1471, 1971.

[106] T. Suwa, J. C. Hogg, K. B. Quinlan, A. Ohgami, R. Vincent, and S. F. van Eeden. Particulate air pollution induces progression of atherosclerosis. *J. Am. Coll. Cardiol.*, 39:935–942, 2002.

[107] I. Tegen, P. Hollrig, M. Chin, I. Fung, D. Jacob, and J. Penner. Contribution of different aerosol species to the global aerosol extinction optical thickness: Estimates from model results. *J. Geophys. Res. Atmospheres*, 102(D20):23895–23915, 1997.

[108] A. Tokay and K. V. Beard. A field study of raindrop oscillations. Part 1: Observation of size spectra and evaluation of oscillation causes. *J. Appl. Meteor.*, 35:1671–1687, 1996.

[109] E. Trinh and T. G. Wang. Large-amplitude free and driven drop-shape oscillations: experimental observations. *J. Fluid Mech.*, 122:315–338, 1982.

[110] E. H. Trinh. Compact acoustic levitation device for studies in fluid dynamics and material science in the laboratory and microgravity. *Rev. Sci. Instrum.*, 56:2059–2065, 1985.

[111] C. J. Tsai, C. N. Liu, S. M. Hung, S. C. Chen, S. N. Uang, Y. S. Cheng, and Y. Zhou. Novel active personal nanoparticle sampler for the exposure assessment of nanoparticles in workplaces. *Environ. Sci. Technol.*, 46(8):4546–4552, 2012.

[112] J. R. Turner and S. V. Hering. Greased and oiled substrates as bounce-free impaction surfaces. *J. Aerosol Sci.*, 18(2):215–224, 1987.

[113] R. L. Verrier, M. A. Mittleman, and P. H. Stone. Air pollution: an insidious and pervasisve component of cardiac risk. *Circulation*, 106:890–892, 2002.

[114] G. Vidal-de Miguel and J. F. de la Mora. Continuously converging multistage focusing lenses to concentrate aerosols at high Reynolds numbers. *Aerosol Sci. Technol.*, 46(3):287–296, 2012.

[115] J. H. Vincent. *Aerosol Sampling: Science, Standards, Instrumentation and Applications*. John Wiley & Sons, England, 2007.

[116] O. Vohl, S. K. Mitra, K. Kiehl, and G. Huber. A wind tunnel study of turbulence effects on the scavenging of aerosol particles by water drops. *J. Atmos. Sci.*, 58:3064–3072, 2001.

[117] M. Waldenmaier. Measurements of inertial deposition of aerosol particles in regular arrays of spheres. *J. Aerosol Sci.*, 30:1281–1290, 1999.

[118] W. H. Walton and A. Woolcock. The suppression of airborne dust by water spray. *Intl. J. Air Poll.*, 3:129–153, 1960.

[119] P. K. Wang and H. R. Pruppacher. Acceleration to terminal velocity of cloud and raindrops. *J. Appl. Meteor.*, 16:276–280, 1977.

[120] P. K. Wang and H. R. Pruppacher. An experimental determination of the efficiency with which aerosol particles are collected by water drops in subsaturated air. *J. Atmos. Sci.*, 34:1664–1669, 1977.

[121] X. Wang, L. Zhang, and M. D. Moran. Uncertainty assessment of current size-resolved parameterizations for below-cloud particle scavenging by rain. *Atmos. Chem. Phys.*, 10:5685–5705, 2010.

[122] X. Wang, L. Zhang, and M. D. Moran. On the discrepancies between theoretical and measured below-cloud particle scavenging coefficients for rain–a numerical investigation using a detailed one-dimensional cloud microphysics model. *Atmos. Chem. Phys.*, 11(22):11859–11866, 2011.

[123] H. N. Webster and D. J. Thomson. The NAME wet deposition scheme. Technical report, Forecasting Res. Tech. Rep., 2014.

[124] A.A. Zamyshlyaev and G.R. Shrager. Fluid flows past spheroids at moderate Reynolds numbers. *Fluid Dynamics*, 39(3):376–383, 2004.